OPTIMISATION OF SHOT PEENING FOR 12Cr STEEL IN STEAM TURBINE BLADE APPLICATIONS

By

MARK NEWBY

A thesis submitted to the University of Plymouth

for the degree of

DOCTOR OF PHILOSOPHY

School of Marine Science and Engineering

October 2012

CANDIDATE: MARK NEWBY

TITLE: OPTIMISATION OF SHOT PEENING FOR 12Cr STEEL IN STEAM TURBINE BLADE APPLICATIONS

ABSTRACT

Power generation in thermal stations typically relies on large steam turbines. The corrosion resistant steel blades used in the last stage of a typical low pressure rotor set are approximately 1m long and experience high centrifugal loading during service. They operate in a wet steam environment, at approximately 60°C while rotating at 3000rpm, and failure modes include high and low cycle fatigue, stress corrosion cracking or corrosion fatigue. The blades are retained by a fir tree root which is normally shot-peened to generate compressive residual stresses that resist crack initiation. Finite element (FE) modelling has indicated that, in the absence of shot-peening, stresses above yield are induced at the fir tree root during operation. In a shot-peened blade these lead to relaxation of the shot peening residual stresses. To date, no systematic information has been obtained on the level of residual stresses induced in the fir tree by shot-peening and their subsequent relaxation during service loading, nor are there any guidelines as to the magnitude of residual stresses necessary to ensure integrity of the turbine over a life span of at least twenty years. At least one of these blades has suffered catastrophic failure in recent years causing severe damage, in excess of €100M, to the turbine-generator set on a South African power station [**1**].

This thesis reports results from a comprehensive program of residual stress measurements at the shot-peened fir tree roots of service blades, and in specimens that simulate the root conditions, using diffraction data from laboratory and synchrotron X-ray radiation (SXRD). Shot-peening coverage between 75% and 200% was used and stresses were measured over a depth of 5mm into the blades/specimens. Measurements were made in the as-peened condition and after applying cyclic stresses representative of overspeed proof testing and of service operation. The results were used to calibrate FE modelling of residual stresses and as input into fatigue life prediction.

LIST OF CONTENTS

LIST OF TABLES AND ILLUSTRATIONS

NOMENCLATURE

ESRF	European Synchrotron Radiation Facility located in Grenoble, France
ILL	Institut Laue-Langevin. A neutron diffraction research facility located in Grenoble, France
SALSA	Strain Analyser for Large and Small Articles
Eskom	Electrical utility in South Africa
NPL	National Physical Laboratory, UK
EPRI	Electric Power Research Institute
SAE	Society of Automotive Engineers
SXRD	Synchrotron X-ray radiation diffraction
Laboratory XRD	X-ray radiation diffraction, when the X-rays are produced in a tube
ID31	ESRF beam line number ID31
ID15A	ESRF beam line number ID15A
SCC	Stress corrosion cracking
LP	Low pressure
IP	Intermediate pressure
HP	High pressure
BC	Before Christ
Dryness fraction	Ratio of moisture in steam
0.2% yield stress	Yield point in a material that results in 0.2% permanent strain
UTS	Ultimate tensile strength
ANSYS	Finite element modelling package

LS-DYNA	General purpose multi-physics simulation software package
EDEM	Discrete element modelling package
LAMP	Large Array Manipulation Program used at ESRF
MATLAB	A numerical technical computing software package
Python	Open source programming language
Scipy	Python scientific analysis module
Kinfit	Python curve fitting module
Almen strip	A thin flat plate used to measure the intensity of shot peening
R ratio	Stress ratio
Cr	Chrome
Ni	Nickel
Mo	Molybdenum
V	Vanadium
NaCl	Sodium Chloride
H_2SO_4	Sulphuric acid
λ	wavelength
d_0	Unstrained lattice parameter
θ	Scattering angle of X-ray beam
σ	Stress
σ_l	Longitudinal stress from longitudinal strain
σ_{lt}	Longitudinal stress from through-thickness strain
σ_N^{re}	Surface residual stress after N cycles
ψ	Angle of inclination of a sample

ϕ	Angle measured stress to principal stress
$\boldsymbol{\varepsilon}$	Strain
ε_l	Longitudinal strain
ε_t	Through-thickness strain
δz	partial derivative of function z
$\delta\sigma_l$	Fractional stress error from longitudinal strain measurement
$\delta\sigma_{lt}$	Fractional stress error from through-thickness strain measurement
ν	Poisson's ratio
E	Elastic modulus
rpm	revolutions per minute
µm	micron
MW	mega watt
Pa	Pascal
°C	degrees Celcius
K	degrees Kelvin
kgf	kilogram force
keV	kilo electron Volt
GeV	Giga electron Volt
nm	nanometer
Å	Angstrom
LCF	Low cycle fatigue
HCF	High cycle fatigue

ACKNOWLEDGEMENTS

The author gratefully acknowledges: the ESRF for the award of beam time for experiments MA326 and ME1165; the Eskom research program for funding allocations; Dr Sabine Verryn from the University of Pretoria, South African Airways Technical Services for use of their shot peening facility.

I am indebted to my supervisors Prof MN James and Prof DG Hattingh for all their support and encouragement.

I would like to thank Dr A Steuwer for his guidance and assistance with the ESRF experimental work and Mr R Scheepers for his assistance with finite element modelling

To my wife Pia and sons Eric and Luke, thank you for all the support and understanding during this stressful period.

AUTHORS DECLARATION

AUTHOR'S DECLARATION

At no time during the registration for the degree of Doctor of Philosophy has the author been registered for any other University award.

This study was supported by the Eskom research program (South Africa), internal funding from the University of Plymouth and the allocation of beam time at the ESRF, Grenoble in experiments MA326 and ME1165.

Relevant scientific seminars and conferences were regularly attended at which work was presented; external institutions were visited for consultation purposes and a paper was accepted as a plenary presentation at the Fatigue 2010 conference and published by Elsevier in Procedia Engineering.

Presentation and Conferences Attended:

FATIGUE 2010 Conference, Prague, Czech Republic

“Shot Peening of Steam Turbine Blades: Residual Stresses and their Modification by Fatigue Cycling”. MN James, M Newby, DG Hattingh and A Steuwer, FATIGUE 2010, Procedia Engineering 2 (2010) 441–451

External Contacts:

Word count of main body of thesis: 23968

Signed 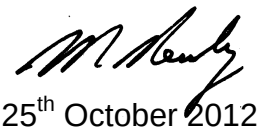

Date 25th October 2012

CHAPTER 1 INTRODUCTION

1.1 Background

Power generation in thermal stations relies on large steam turbines that drive the electrical generator. Steam is produced in the boiler and then transferred to the turbines via main steam piping. In a typical 600MW unit at the South African power utility Eskom, the main steam pressure and temperature at the entrance to the turbine, are approximately 16.4MPa and 535°C. This steam passes through a turbine train comprised of a high pressure (HP) stage, an intermediate pressure (IP) stage and then two low pressure (LP) stages. The energy extracted from the steam causes the turbine train to rotate and drive the two pole electrical generator. The South African electrical grid operates at 50Hz, so the shaft speed of the turbo-generator is 3000rpm. A typical steam flow path schematic is shown in Figure 1. The percentage power contribution to the 600MW output from each stage in the turbine is; HP casing 28%, IP casing 39% and LP casings 17% each.

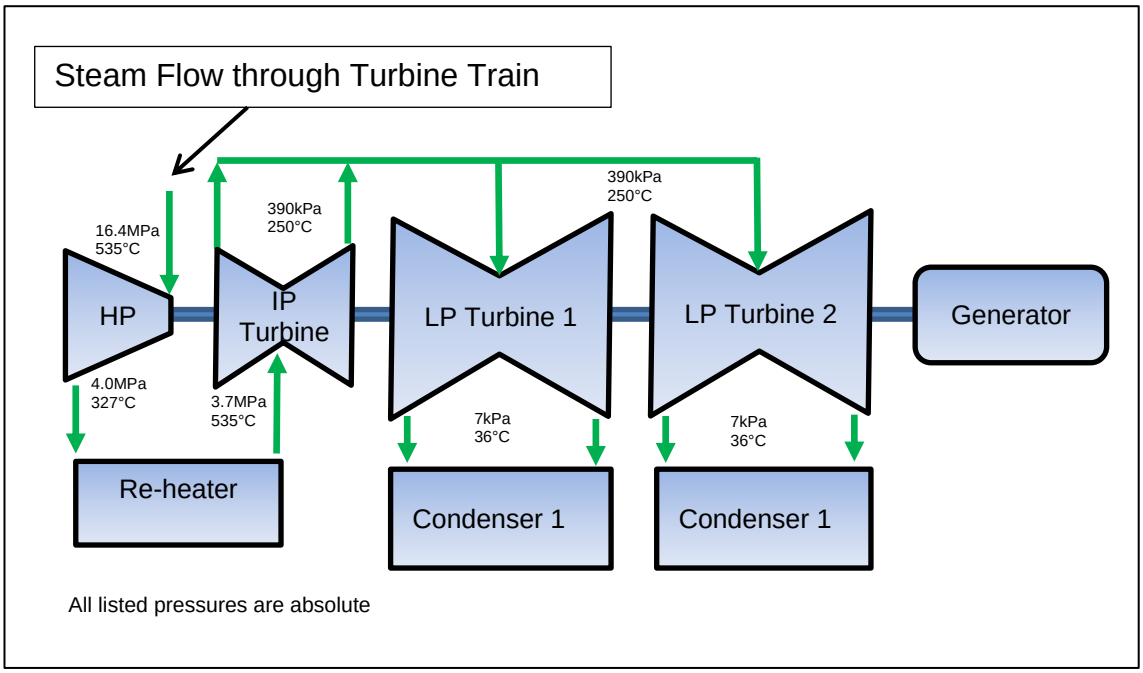

Figure 1: Steam path schematic (indicated by the green arrows)

The LP turbines have dual flows, meaning that the steam enters at the centre of the casing and then flows along two expansion paths to exit into the condenser. A typical LP rotor set, with covers removed, is shown in Figure 2.

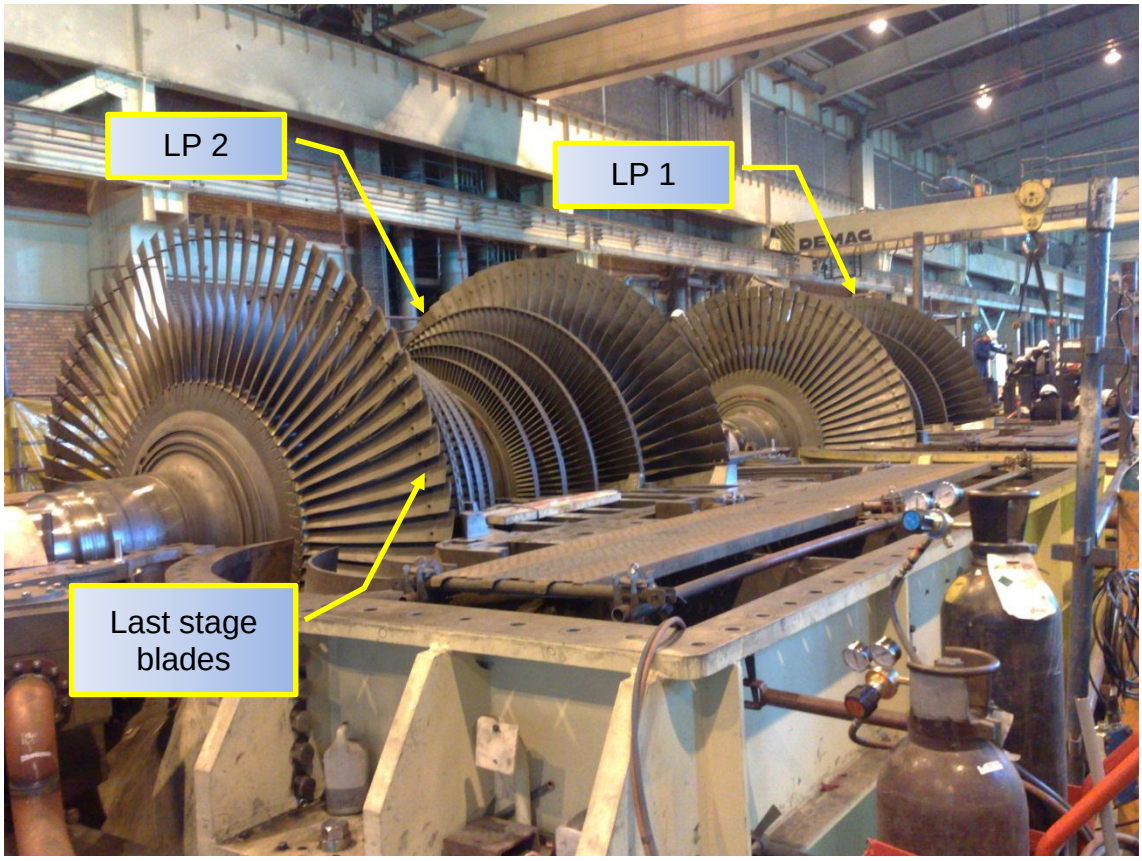

Figure 2: Low Pressure rotors from a 600MW turbo-generator

The last-row blades of the LP turbine analysed in this thesis, are approximately 1m long, are made from 12Cr corrosion resisting steel according to DIN1.4939 [**2**], with a 0.2% yield stress of 868MPa. The blades experience high centrifugal loading at 3000 rpm during service, up to 700MPa in the attachment areas, and operate in a wet steam environment. The steam conditions in the LP turbine vary from 250°C and 4MPa at the inlet to 38°C and 7kPa at the outlet. The last-row blades typically experience saturated steam at 60°C with a dryness fraction of 0.91. The dryness fraction of saturated steam ranges from 0 to 1, with 1

being completely dry. The failure modes of the blades can involve high or low cycle fatigue, stress corrosion cracking or corrosion fatigue. Figure 3 shows an axial view of the last stage blades from a 600MW turbo-generator set. The blades are retained by a fir tree root, which is highlighted by the inset photograph and shown more clearly in Figure 4. The fir tree attachment area is typically shot peened so that the induced compressive residual stresses resist crack initiation.

Operating cycles that affect the fatigue life are the start/stop cycles that result in large centrifugal stress changes, steam flow stresses induced during normal steady state operation, dynamic stresses due to shaft critical speeds near resonant frequencies and dynamic stresses due to flow induced excitation.

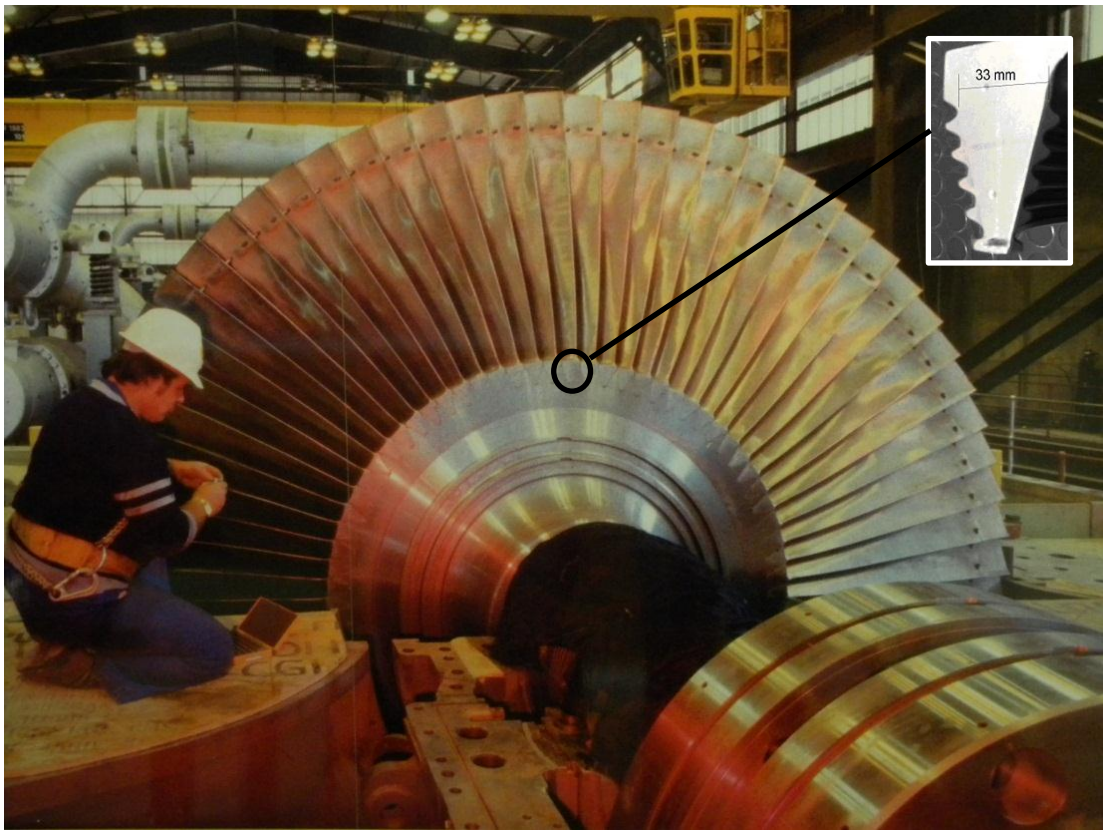

Figure 3: Axial View of a Low Pressure rotor from a 600MW turbo-generator showing the last stage blades of the turbine, with an inset image of the fir tree root

There are some concerns over whether the shot peening of the fir tree root region is effective in this application. Overspeed tests, up to 3300rpm, are conducted periodically, normally after maintenance operations that may have affected the balance of the rotor. The overspeed tests are significant due to the centrifugal stress varying with the square of the rotational speed. Thus a 10% overspeed of 3300rpm leads to a 21% increase in centrifugal stress.

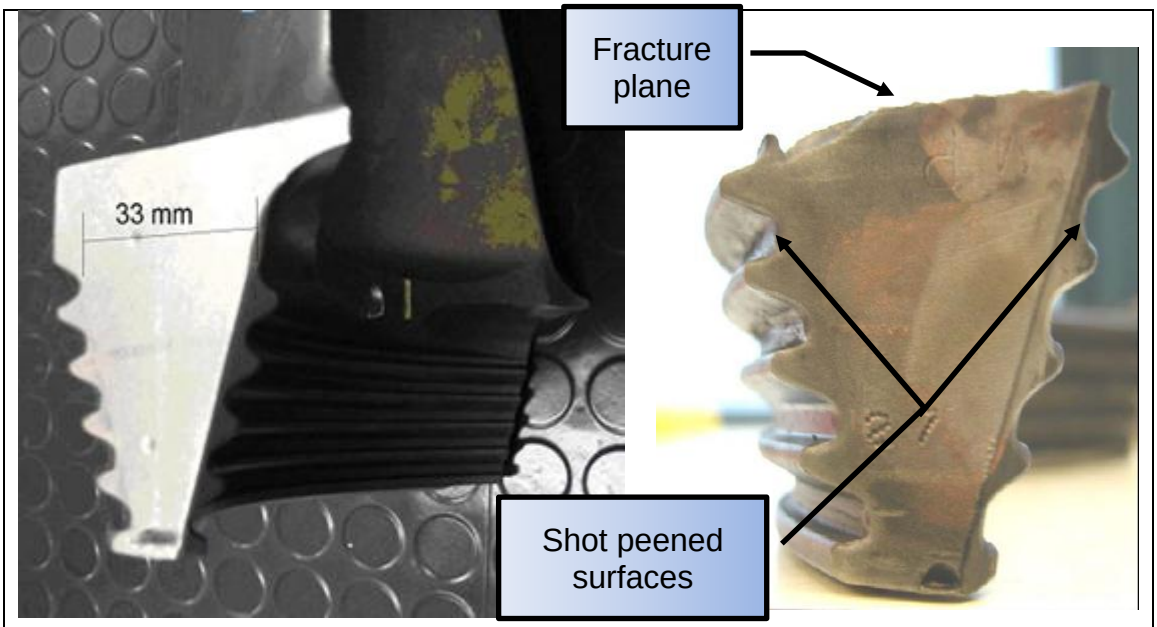

Turbine blade fir tree root

Failure in top serration of fir tree root

Figure 4: Fir tree shape of turbine blade root

Statutory overspeed tests have to be performed periodically on the installed rotor system, to check overspeed protection systems, and there have been instances where the rotor speed has reached 3600rpm. This would cause a 44% increase in centrifugal stress. These overspeed cycles result in localised stresses causing yielding of the material, which may reduce the level of residual compressive stress in the shot peened root region. A complete last stage LP turbine blade from a 600MW is shown in Figure 5.

Figure 5: Complete last stage LP turbine blade

The effect of the overspeed loading is illustrated in Figure 6, where the localised stress predicted by a finite element model in the top serration at 3600rpm is 998MPa which is above the 0.2% yield stress. In addition the varying profiles of the fir tree configuration make the application of uniform shot peening difficult, which may result in some areas not receiving the correct coverage, potentially leading to a smaller depth of shot peened layer and lower residual stresses.

A failure of one of these blades at a South African power station in January 2003 [**1**] caused a catastrophic turbine failure which resulted in a fire, severe damage to the turbine-generator set and loss of production of a 600MW unit for a period of six months with total damages amounting to nearly €100M. A photograph of the failed blade root is shown in Figure 4, and it can be seen that the failure occurred in the top serration of the fir tree. The cause of this failure was confirmed to be stress corrosion cracking, and this finding stimulated further investigation into the effectiveness of shot peening as a mitigation

measure. The shape of the fir tree root makes it particularly difficult to get consistent and complete coverage during shot peening, requiring a complex procedure with six different shot peening nozzles set up at various angles.

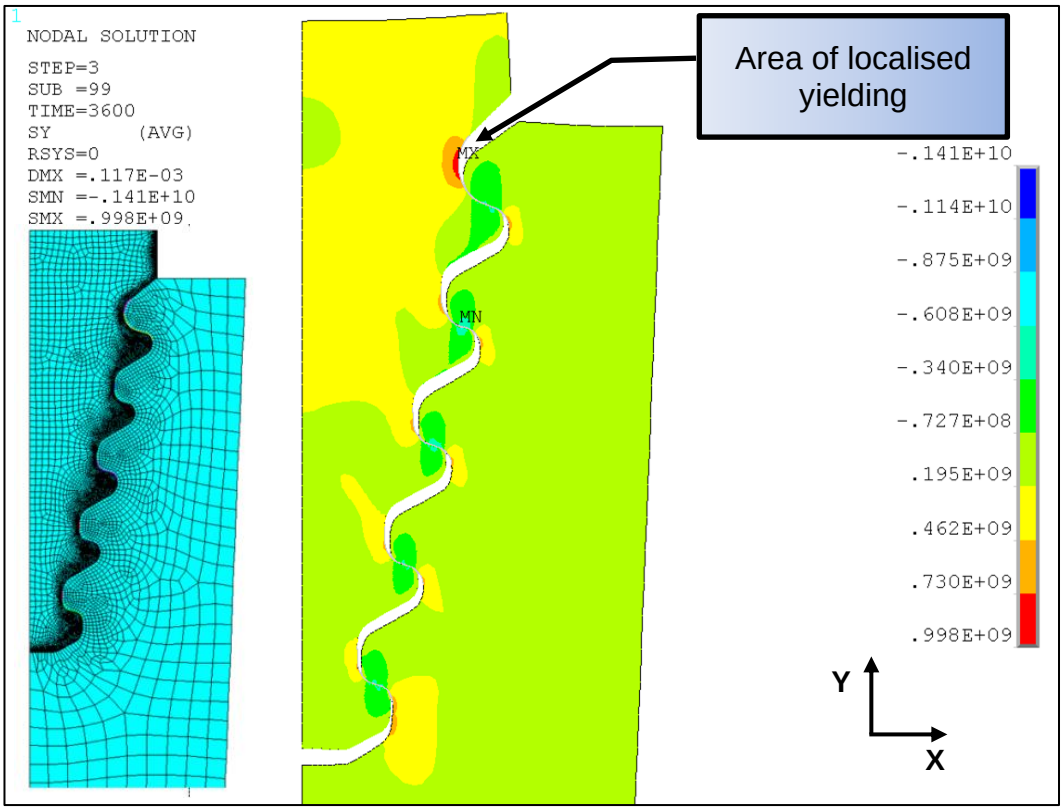

Figure 6: Finite element analysis (plane strain) of fir tree root for centrifugal loading at 3600rpm, resulting in localised stress in the top serration of 998MPa.

Until recently it has not been possible to effectively measure the residual stresses profiles with depth below the surface in a typical blade attachment region. Measuring the depth profile of residual stress without physically removing any material is only possible with either neutron or synchrotron diffraction techniques. Development work done with high intensity X-rays generated by a synchrotron radiation device has shown that through-thickness residual stress measurements with a high spatial resolution are possible in steel components up to some 15 mm thick.

A research facility in Grenoble, France, houses both a neutron source and a synchrotron accelerator;

- The Institut Laue-Langevin (ILL) provides an intense neutron source with several beam lines for different fields of research, the SALSA (Strain Analyser for Large and Small Articles) beam line is designed for materials research. SALSA is the world-leading neutron instrument for the assessment of residual stress in engineering components, the SALSA field of application is wide but it is particularly well suited to bulk strain measurements where the high flux of the ILL reactor is exploited. Spatial resolution is limited to approximately 200μm.
- The European Synchrotron Radiation Facility (ESRF) generates high intensity X-rays and two of the beam lines, ID15A and ID31 are designed for materials research. The advantage of synchrotron X-ray diffraction (SXRD) is that it allows for much finer spatial resolution, approximately 50μm, than can be obtained with neutron diffraction, and was thus better suited to the planned experimental work for this thesis.

Preliminary work at the ESRF through FaME38, a UK funded facility to support materials engineering at the ESRF site, on beam line ID15A demonstrated the ability of synchrotron diffraction to yield high quality data, both in terms of strain and displacement resolution, on stresses in the blade root region. Two detectors were used to simultaneously measure strains in two orthogonal directions, and the blade mounted on the ID15A instrument is shown in Figure 7.

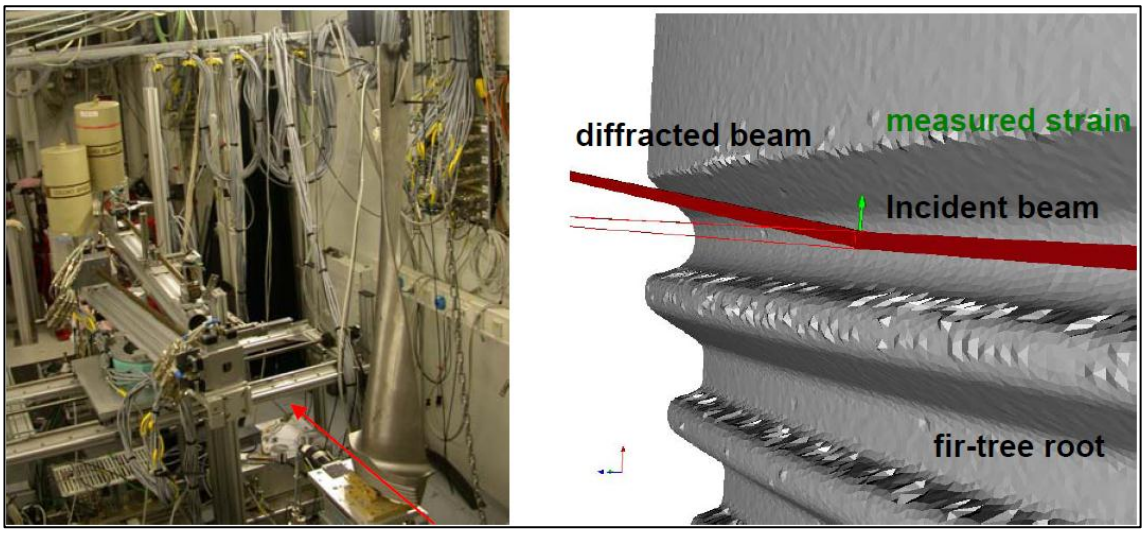

Figure 7: Turbine blade set up on beam line ID15A at the ESRF

This was the first time that such a technique has been used on steam turbine blades and opened up opportunities for rigorous analysis of the blade root condition. Based on the success of this initial work a PhD project was commenced through Plymouth University to analyse in detail the residual stresses induced by shot peening in a series of samples manufactured from 12Cr steels used in turbine blade applications for the power industry.

1.2 Objectives

The aims of the synchrotron work were:

- To quantify the shot peened residual stress depth profiles on three fir tree samples after exposure to the standard 200% coverage condition as specified in the Eskom guideline for shot peening of turbine blades [**3**].
- To quantify the shot peened residual stress depth profiles due to four different coverage conditions on flat plate specimens. The different coverage conditions were chosen to determine whether there would be an adverse effect of blade performance in service arising from under-peening on the fir tree root. Coverage conditions of 75%, 100%, 150%

and 200% were chosen as representing realistic possible variations in coverage around the fir tree root profile from the specified 200%. The flat sample configuration was chosen so that tensile loading could be applied after the as-peened residual stress profile had been measured.

- To apply overspeed fatigue stress cycles to the flat plate samples in-situ on a beam-line to simulate the service fatigue effects of the residual stresses. This test condition was chosen due to the concern that overspeed conditions would result in a reduction in magnitude of residual stress after localised yielding had taken place at the fir tree notch root as illustrated by the finite element plot in Figure 6.
- To combine the experimental results with data from a Finite Element model in order to develop predictive capability of the effects of the overspeed cycles on the residual stress profiles and hence on the fatigue and stress corrosion performance of the turbine blade.

The outcomes of this programme of experimental and numerical work will thus allow optimum shot peening conditions to be identified, through integration with finite element modelling results, to real blades in service. This work is hence extremely important for the steam turbine industry to improve the safety and reliability of the rotating generation components. Failure of these components has previously resulted in catastrophic and expensive damage to the turbine as well as long term loss of production. The results from this work will be integrated into a research project that is supported by industry, allowing its findings to have a real impact on industrial practice. Prevention of an incident such as the 2003 failure obviously has significant financial and safety benefits.

In summary this research will focus on the generation of representative data for the residual stress profiles induced in the fir tree attachment region of a last stage LP turbine blade, over a range of shot peening and blade operating conditions; interpretation of the new data and its synthesis into a predictive finite element model, and the development of this model into a tool to relate fatigue performance of turbine blades to material condition and shot peening parameters [**4**] [**5**]. This would represent a fundamental advance in knowledge in an area critical to efficient and safe power generation.

1.3 Research Methodology

The research methodology was designed to eliminate as many system variables as possible, while ensuring that the sample preparation was representative of industry standard conditions. The key aspects of the methodology are summarised below and explained in more detail in Chapter 4.

- Two types of sample for shot peening were prepared; twelve flat hour glass samples that could be loaded in a tensile testing machine after residual stress measurements and three fir tree samples that could be shot peened in the same way as the “in service” blades were treated. Details of the specimens are shown in Figure 8, Figure 10 and Figure 12.
- The samples were all extracted from a single used turbine blade so that the material properties would be consistent, see Figure 9.

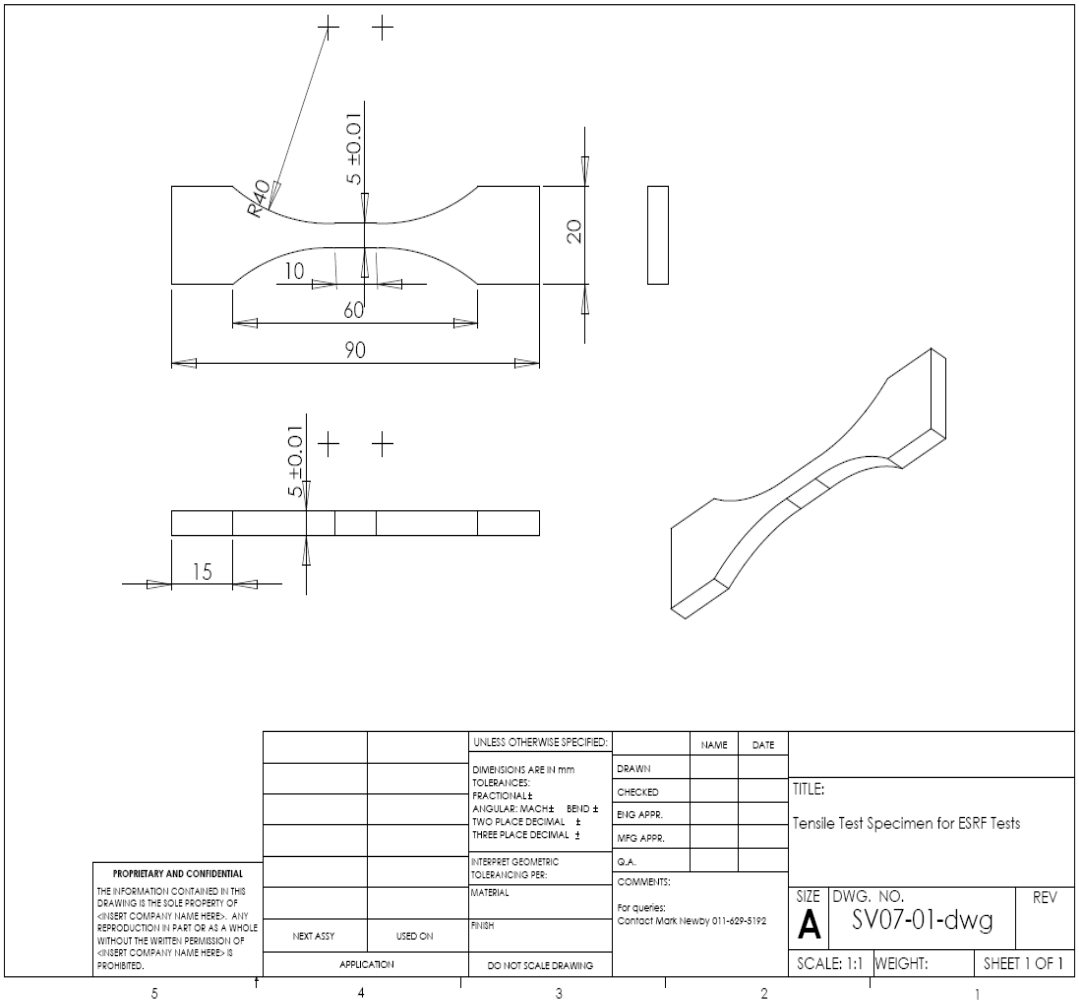

Figure 8: Geometry of flat sample

Front view of turbine blade attachment fingers

Side view showing flat sample location

Figure 9: Photograph of used turbine blade attachment fingers showing flat sample location in blade before machining

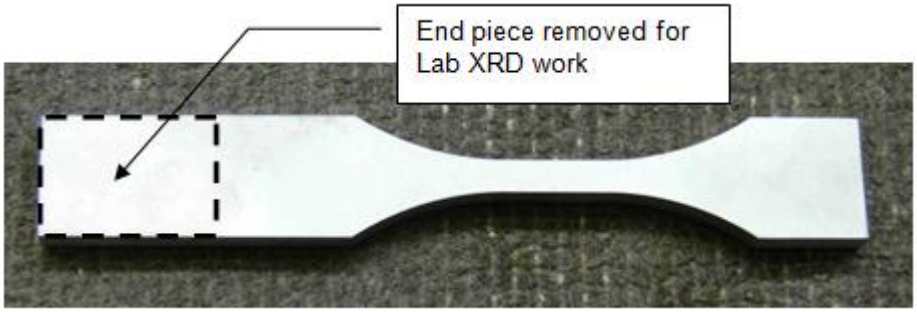

Figure 10: Flat sample after shot peening showing where end piece was removed

- Three tensile test samples were prepared for determining material properties; Elastic modulus, 0.2% yield stress, ultimate tensile strength.
- The shot peening was conducted according to the guideline used by Eskom [**3**]. The guideline conforms to the shot peening standard SAE AMS-S-13165 and calls for six nozzles to be used during the shot peening process. The nozzles were mounted with specific angles at standoff distances of 228.6mm from the blade surface. The blade was mounted on a turntable and as this rotated, the blade root area travelled through the nozzle matrix. The nozzles also moved up and down vertically during this process. When the system was being set up, a test blade with place for seven Almen strips, see Figure 11, was mounted on the turntable and the time required to achieve 100% coverage was measured. This time was then doubled to obtain 200% coverage. The three fir tree samples were inserted into a cut-out on a used blade, Figure 12, so that the samples were subjected to the correct shot peening conditions according to the guideline.

- The flat samples were treated to four different coverage conditions from 75% to 200% and were shot peened on both sides simultaneously to ensure that no additional bending load was induced.

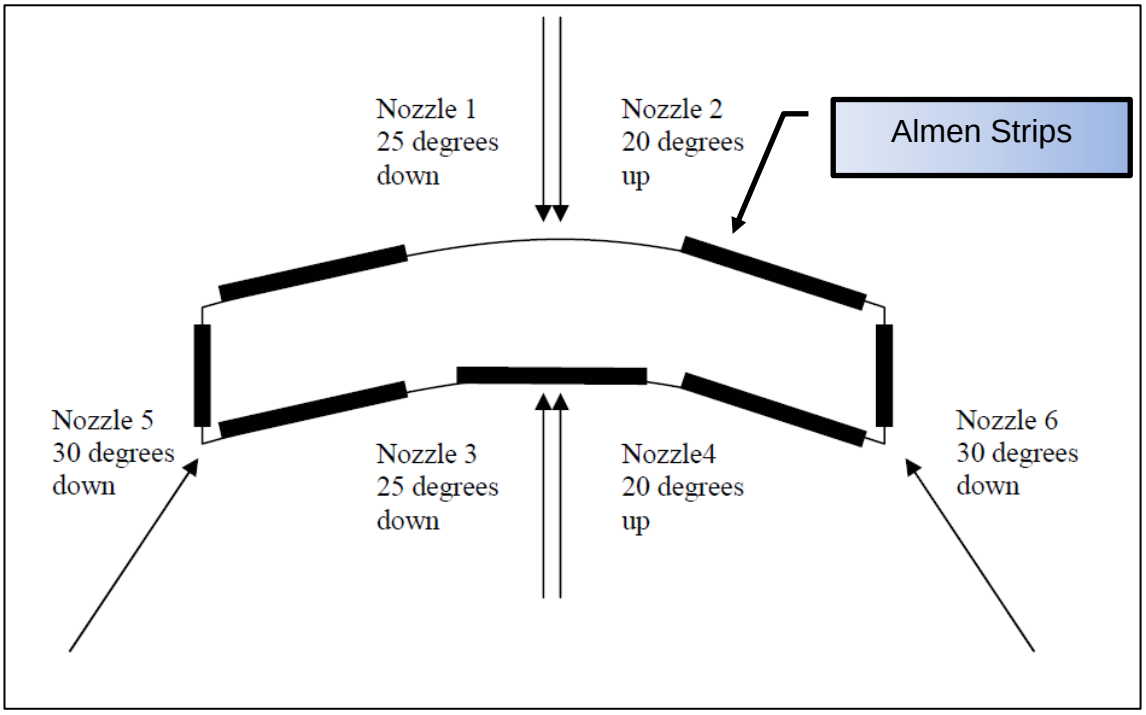

Figure 11: Extract from Eskom guideline [3] showing Almen strip and nozzle locations (plan view of turbine blade fir tree region)

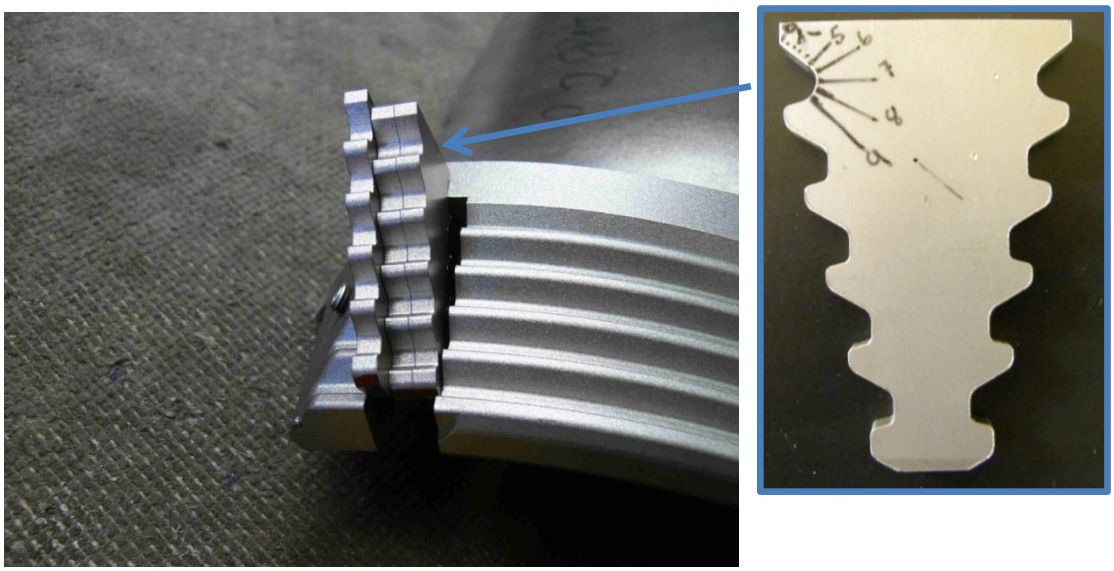

Figure 12: Three fir tree samples after shot peening. The samples were clamped in a cut-out made in an old blade so that the specified shot peening conditions could be achieved

- End pieces from the flat samples, see Figure 10, were analysed using a Panalytical X'pert Pro X-ray laboratory diffraction instrument to determine surface residual stress conditions before starting the synchrotron experiment. This was done in order to ensure that the consistency of treatment for the samples was acceptable, and that the time at the ESRF facility would be used effectively. This was necessary due to the high beam time cost of the ESRF, and limited time granted for experiments. Access to the ESRF facility was obtained through an academic application for beam time and five days were granted for experiment number MA326. The value of this time was approximately 24,000 euros for a 24 hour shift.
- Two samples of each shot peened condition (75%, 100%, 150% and 200%) were measured in the as-peened condition in experiment MA326.
- One sample from each condition, four samples, was then loaded in a single cycle to an applied 868MPa (0.2% proof stress) and the residual stress profiles were then re-measured. These samples were then loaded in a single cycle to 910MPa (0.5% proof stress) and the residual stress profiles re-measured.
- The other four samples, one from each condition, were loaded in a single cycle to 600MPa (limit of proportionality) and the residual stress profiles were then re-measured. These samples were then loaded to a mean stress of 868MPa and a dynamic stress range of 20MPa was applied for 10,000 cycles. The residual stress profiles were then re-measured.
- The fatigue tests in experiment MA326 were performed at a mean stress that was too high; as a result the data had limited application. Another set of data was recorded on a spare sample, Sample 6, during

experiment ME1165 on beam line ID15A. The as-peened condition was measured first and then fatigue loading up to 100,000 cycles with a stress range of 40MPa and a mean stress of 600MPa applied. Residual stress profiles were recorded after 10, 100, 1,000, 10,000 and 100,000 fatigue cycles. The mean load was then increased so that the mean stress reached 848MPa and further fatigue cycles were applied. The complete test matrix is shown in Table 14 on page 103.

- Further laboratory XRD residual stress measurements, combined with surface layer removal, were conducted on the flat samples previously tested at the ESRF, to cross-correlate with the through-thickness (full depth) synchrotron measurements. These tests were done after a Proto iXRD instrument had been purchased by Eskom for general purpose work and the electro-polishing unit supplied by Proto was better suited to localised electro-polishing than the technique used on the flat sample end pieces previously.
- Finally a finite element modelling technique was developed to determine the residual stress profiles on the fir tree after shot peening, and to correlate these results with experimental values. The model was then further used to determine the effect of centrifugal loading on residual stress profiles. Models for both the flat samples and the fir tree were constructed and analysed. The modelling process was initially applied to the flat sample so that the results could be linked with the synchrotron data. The loading simulation was then applied to the fir tree geometry. The models were constructed in ANSYS ver12 as 2D plane-strain models, the fir tree mesh is shown in Figure 6 and Figure 59. Elastic-perfectly plastic constitutive response of the material was assumed and

the residual stress profile was induced using a thermal quench loading technique.

1.4 Research project plan

ACTIVITY	TIMELINE
Literature survey and ESRF proposal	June 2006 to Jan 2007
Manufacture of flat specimens from 12Cr steel	Jan to Feb 2007
Shot peening of flat samples at different intensities	May 2007
Test samples with Laboratory X-ray diffraction	May 2007
ESRF experimental setup for synchrotron measurements	Jan to June 2007
ESRF experiment MA326. Full profile for eight samples, included some tensile test effects	June 2007
Analysis of data	May 2007 to May 2011
Transfer report MPhil to PhD	April 2008
Layer removal tests with Lab X-ray	May 2008
ESRF experiment ME1158. Check in-situ incremental amplitude effects of fatigue loading	Dec 2008
Fatigue 2010 conference.	June 2010
Finite element modelling of shot peening effect in fir tree root	July 2010 to March 2011
Compile thesis	July 2011 to July 2012
Submit thesis	September 2012

CHAPTER 2 LITERATURE REVIEW

2.1 Life Assessment of steam turbine blades

Turbine blade design has to consider and find a suitable compromise between various material and operational variables. These include efficiency of turbine output, mechanical strength, dynamic blade response to vibration excitation, resistance to environmental effects such as corrosion, fatigue characteristics and thermal suitability of the material. Maximum steam turbine temperatures vary from 540°C in the HP and IP casings to 250°C in the LP casings, as shown previously in Figure 1.

The typical design life of a low pressure steam turbine rotor installed in the 1980's was 100,000 hours, with current designs being rated at 200,000 hours [**6**], [**7**]. According to McCloskey et al, [**8**] [**9**] "fatigue in LP turbine blades is one of the most common underlying causes of steam turbine failures". These fatigue failures are exacerbated by unfavourable environmental effects

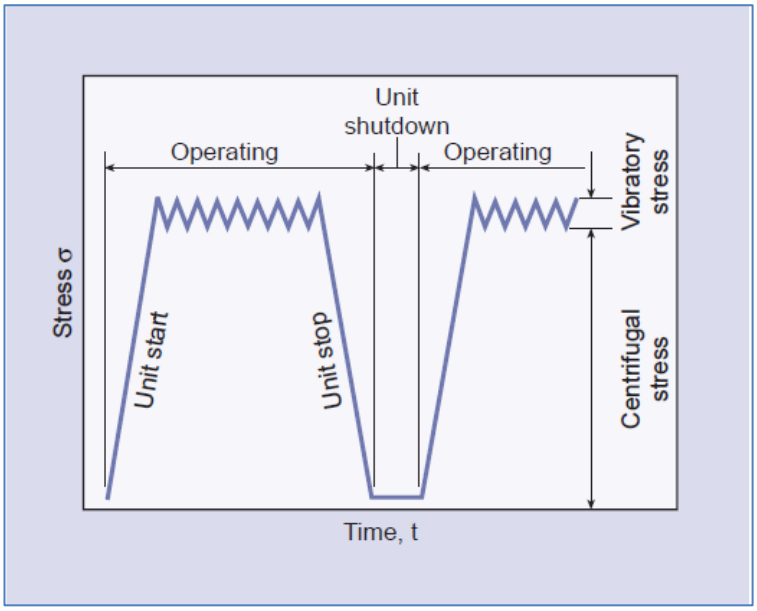

Figure 13: Typical turbine blade stresses during start-stop and operation [8] (fig 5-9). ***Permission to reproduce figure granted from EPRI***

Operational stresses that occur during normal operation are listed below;

- centrifugal stresses resulting in tensile, bending and torsion effects
- steady state steam bending stress
- stresses caused by stiffening attachments such as blade shrouds, lashing wire or wing bands.
- dynamic stresses due to vibrational effects, particularly if natural frequencies are excited and resonance occurs, as explained further below
- thermally-induced stresses during transients such as start-up and shut-down conditions
- effects of stress concentrations such as blade root attachments, which could be fir tree dovetails or pinned forks, as well as any other sharp radii

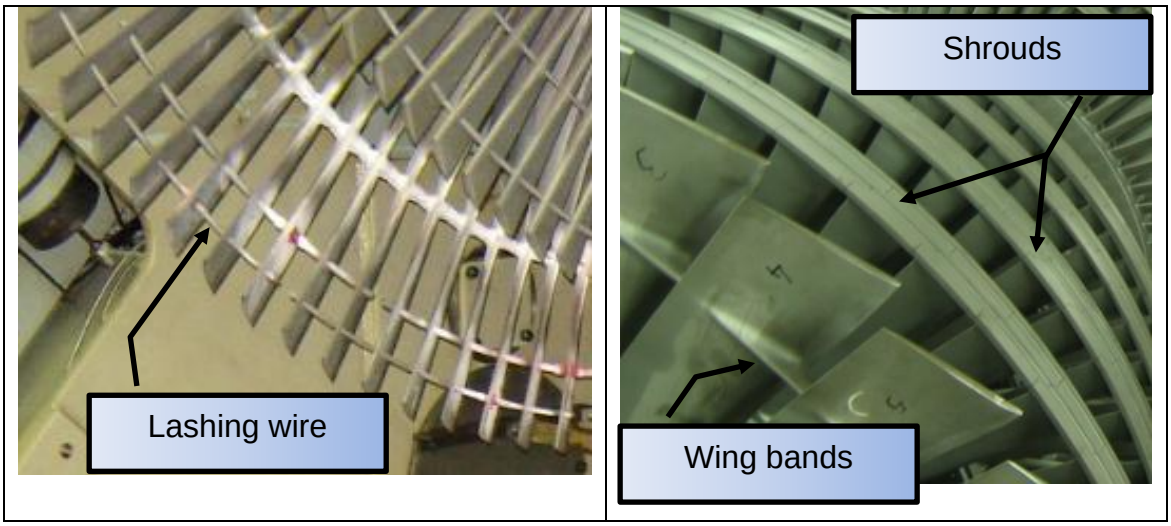

Figure 14: Examples of shrouding, lashing wire and wing bands on LP turbine blades

Of these, probably the most difficult to quantify, are those stresses caused by vibration. Vibration-induced stresses in turbine blades have numerous sources, which include:

- non-uniform pressures around the flow path due to velocity or angle changes in the steam flow path from various factors e.g. partial steam

admission, bending of steam flow at inlet/outlet, leakage at diaphragm half joints, damaged diaphragm blades, stay-bars, and aerodynamic effects such as nozzle wakes.

- unsteady flow in stationary flow passages due to choked flow and flow separation amongst others
- stall and flutter causing cavitation
- disk-induced vibration resulting in disk nodal modes resonating
- moisture-induced vibration, particularly on the last stage blades when the steam has the highest moisture content

Non-uniform pressures and choked flows generally result in a flow discontinuity which causes a once per revolution pressure pulse to be applied to the blades. This forced excitation can result in natural frequencies being excited. The EPRI guideline on steam path turbine damage [**9**] summarises an overview of blade stresses and their contribution to fatigue.

Table 20-3
Overview of Blade Stresses and Their Contribution to Fatigue in LP Turbines

Stress Type	Nature of loading	Source/root cause	Contribution to fatigue
Centrifugal tensile stresses	Steady state	Rotation of blade.	Increased mean stress level.
Geometric untwisting	Steady state	Induced by untwisting of blade.	Mean stresses.
Centrifugal bending stresses	Steady state	A result of blade response to centrifugal forces because section centroids at different heights do not fall on the same radial line.	Mean stresses.
Steam bending loads	Steady state and dynamic	Induced by steam moving within the blade path.	Mean stresses; HCF.
Synchronous resonance of blades with a harmonic of the unit running speed.	Dynamic	Variety of sources. See discussion in Chapter 5.	HCF.
Non-uniform flows	Dynamic	Can be produced by a variety of phenomena (see Chapter 5) such as nozzle-wake interactions, non-uniform pressures, flow bending, geometrically-induced flow unsteadiness.	HCF.
Blade vibration induced from rotor or disc.	Dynamic	A variety of causes including rotor torsional loading and various blade-disc interactions. See Chapter 5.	HCF.
Self-excitation.	Dynamic	Includes stall flutter, unstalled flutter and condensation shocks. See Chapter 5.	HCF.
Start-stop transients and overspeeds.	Dynamic	Loading induced by various modes of turbine operation.	LCF.
Manufacture and assembly stresses.	Steady state	Includes a variety of effects and sources such as (i) bending induced by shroud and lashing wire loads, (ii) stress concentrations caused by assembly and attachment tolerances, (iii) increased loads caused by attachment constraints, and (iv) residual stresses from assembly such as tenon cold working or weld repair.	Mean stresses.

Figure 15: Extract from Table 20-3, page 20-9, Turbine Steam Path Damage: Theory and Practice, Volume 2: Damage Mechanisms [9]. ***Permission to reproduce figure granted from EPRI***

Resonance, caused by any of these excitation forces coinciding with a natural frequency of a blade or a disk model, is a phenomenon that turbine blade designers try to avoid. Resonance can result in high cycle fatigue and in the worst cases result in catastrophic failure as shown in Figure 16. The stress resulting from the resonant condition is directly affected by the damping of the system. Rieger [**10**], refers to the catastrophic failure of a LP turbine due to resonance from whirling, which occurs as a sub-synchronous excitation of the turbine shaft from the rotation of the oil film in the journal bearings that support the turbine shaft.

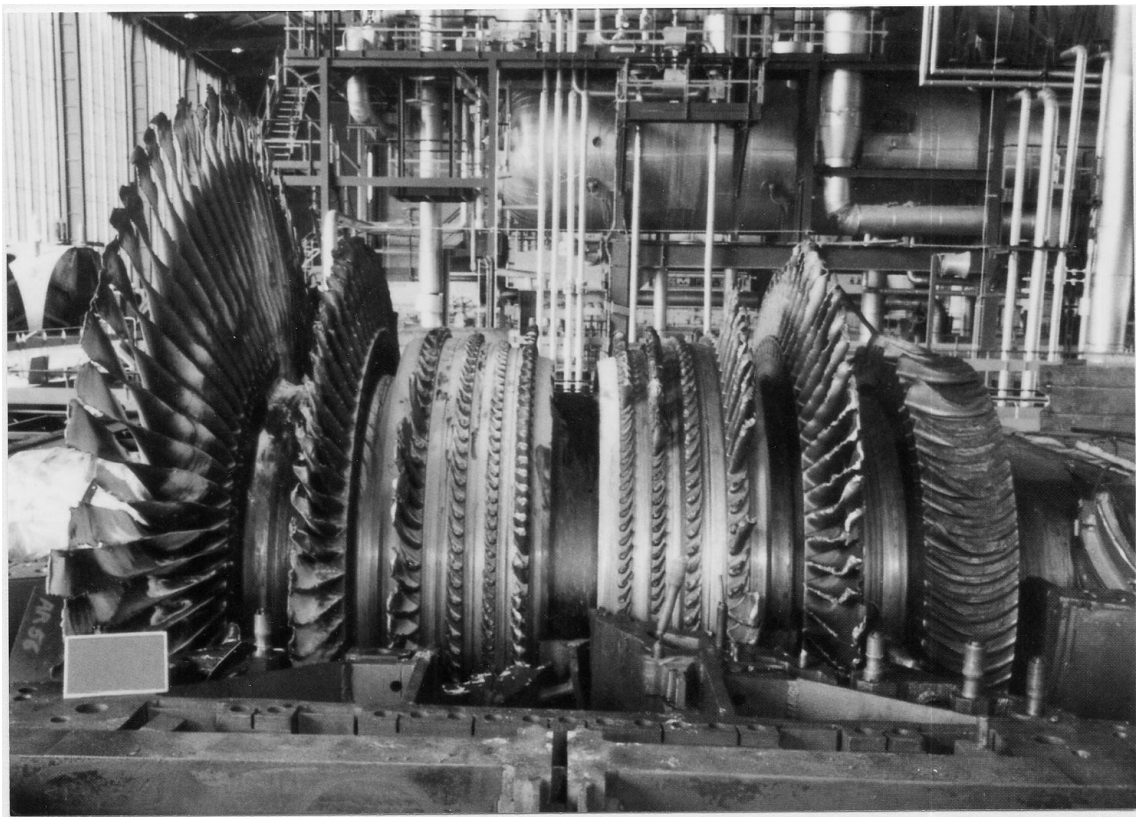

Figure 16: LP Rotor failure due to excessive whirling [10**].** ***Permission to reproduce figure granted from the Vibration Institute © 2013***

Evaluation of the potential for resonance can be conducted in a number of ways, but the most commonly used method is a Campbell diagram as shown in simplified form in Figure 17. The order lines, which are determined from the frequency of shaft speed multiplied by the order number, are plotted against the shaft speed. The turbine blade/disk natural frequencies, at different shaft speeds, are superimposed on the plot and intersections with the order lines indicate potential resonance points or shaft critical speeds. The most important region to focus on is the rated steady-state speed for the shaft, in this case 3000rpm. The vertical line on the plot shows the operating point for the turbine and the potential for resonance of the first disk mode natural frequency where it intersects with the fourth order line.

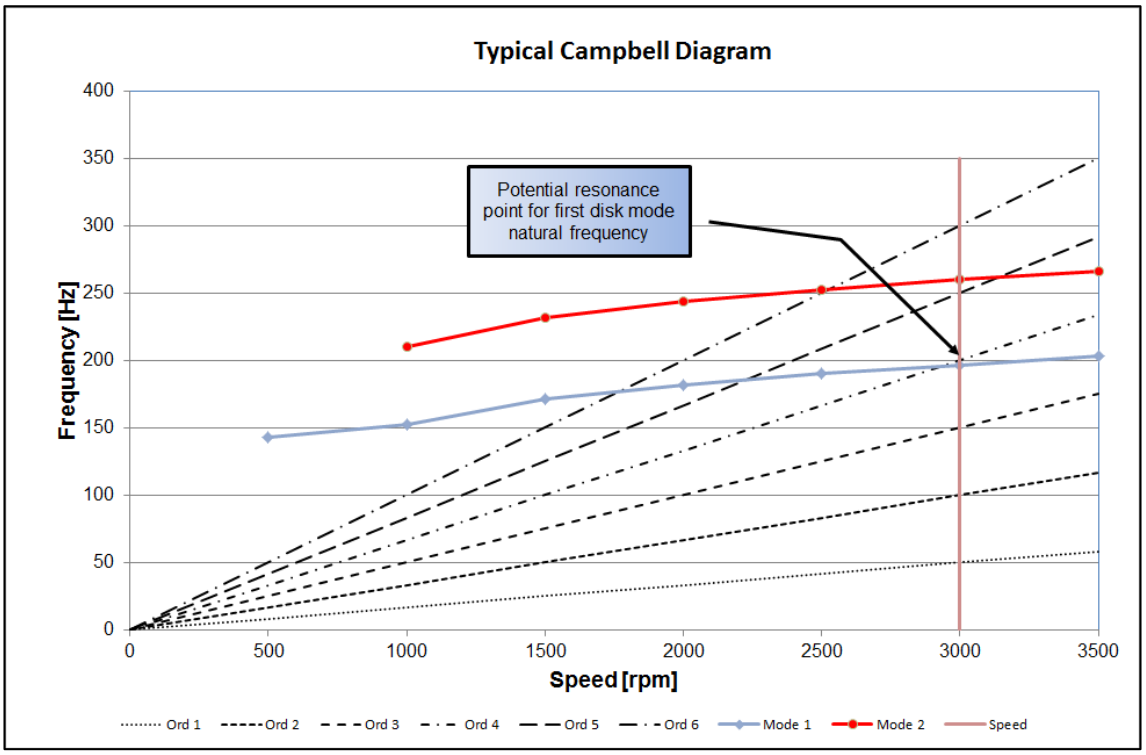

Figure 17: Campbell diagram of a LP rotor stage showing the first two disk mode natural frequencies and a potential resonance point at a shaft speed of 3000rpm. The first six order lines are shown.

Material selection has to take into account a number of parameters such as; mechanical strength, corrosion resistance, toughness, fatigue strength, notch sensitivity and erosion resistance. In the case of LP turbine rotors, the steam exits the casing in a wet condition, and the steels generally have a high Chrome content to minimise corrosion.

Failure mechanisms include; high and low cycle fatigue, stress corrosion cracking (SCC), fretting, erosion, local yielding and manufacturing defects. The most serious failures, should they occur, are on the last stage blades in the root attachment area. The focus of this study is the fir tree root attachment. Surface treatment measures that induce compressive residual stresses, such as shot peening, are used on the highly stressed areas to improve fatigue life.

Prabhugaunkar et al [**11**] conducted a study into the effects of shot peening on high cycle and corrosion fatigue, specifically on 12% Cr steel used in turbine blades. The samples used were round and were subjected to rotary bending loads. In addition SCC tests were conducted on U-bend samples subjected to a 3.5%NaCl corrosive environment. The benefits of shot peening were clearly demonstrated leading to their conclusions that;

- Fatigue properties in air improved by approximately 25%
- Resistance to stress corrosion cracking improved by a factor of three
- Resistance to corrosion fatigue improved by approximately 40%

2.2 Shot peening

Shot peening is a surface treatment process aimed at inducing compressive residual stress into a component. The component is subjected to a stream of particles composed of conditioned cut wire, cast steel or ceramic beads, driven by pressurised air and accelerated through a nozzle to speeds which typically range from 20 to 70m/s [**12**], [**13**], [**14**] depending on parameter settings. The cut wire particles are manufactured from a length of wire, cylindrical in cross section, and the cut faces are too sharp to give a good surface finish on the work piece. The cut wire particles must first be conditioned, with the sharp corners removed, so that they are close to spherical in shape. The particles are cut with a length equal to the diameter, so it is easy to vary the size of the shot by using different diameter wire. The hardness of the shot should be at least as hard as the Almen strip material and the work piece. This is easier to control in cut wire than in cast steel.

The particles plastically deform the surface of the component to a depth of tens of microns [**15**], the constraint of the elastically deformed material below this layer results in a compressive surface stress that has to be balanced by a sub-surface tensile stress. The sub-surface tensile balancing stress requires careful consideration on thin samples as the tensile peak can cause a metallurgical notch in the sample.

Figure 18 shows a schematic illustrating the process of a single shot impacting on the surface of a work piece. The particle indents the surface and produces a small amount of plastic deformation on the surface. After the impact the constraint of the material under the surface tries to force the plastic layer back into position generating the compressive residual stress on the surface.

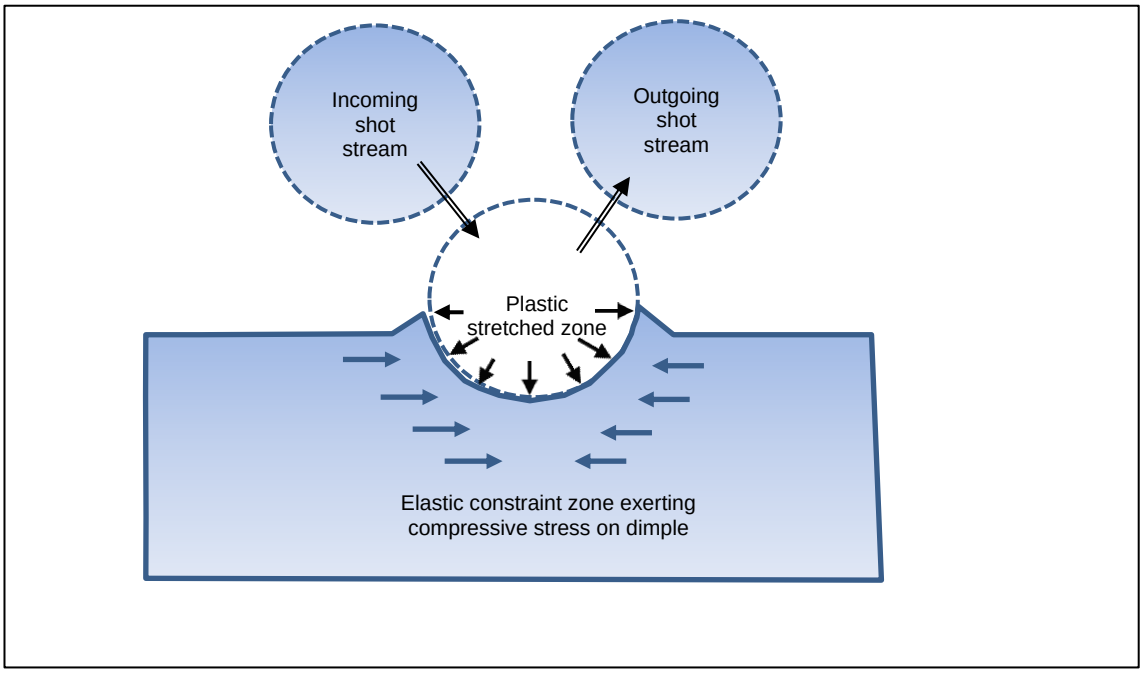

Figure 18: Illustration of shot peened effect

The depth of compressive stress depends on the material properties and the shot peening parameters, but is in the order of 150µm to 400µm. The surface stress on a component will be made up of the residual stress and the

superimposed operational stress. The surface residual compressive stress after shot peening is normally between 0.4 and 0.8 of the yield stress. It can be seen in Figure 19, that when the applied operational load results in a high tensile surface stress, which is very detrimental for both fatigue and SCC degradation, the superimposed compressive residual stress has a very significant beneficial effect by reducing the surface stress by approximately 800 MPa.

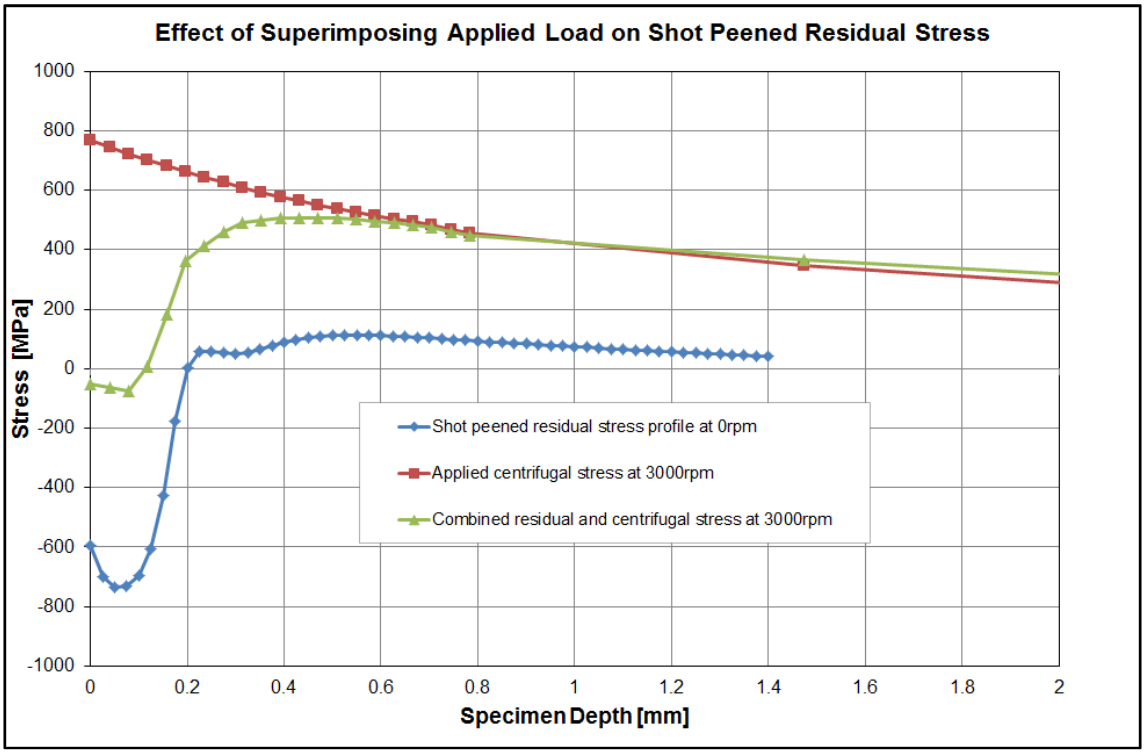

Figure 19: Illustration of a shot peened residual stress profile on a turbine blade combined with centrifugal loading and the stress raiser of the top fir tree serration

Mechanical pre-stressing and peening are cold work forming processes and have been used in various forms since 2700BC [**16**] for manufacture of weapons such as swords and helmets. In the nineteenth century concepts such as roll burnishing and cold rolling of shafts were used in the railroad industry.

The growth in manufacturing and the weapons industry that occurred during two world wars in the first half of the twentieth century, resulted in significant research into metal fatigue. Shot peening was developed as an industrial process in the early part of the twentieth century [**17**], when it was found that components that had been cleaned by sand blasting had improved fatigue performance. One of the pioneers in the industry John O Almen, who worked for General Motors USA, developed a method of standardising the process through the use of thin flat plates that are shot peened on one side, resulting in a known curvature of the plate. The Almen test became the industry standard and is incorporated into shot peening guidelines such as SAE AMS-S-13165 [**18**].

The shot peening process is characterised and evaluated through three parameters [**19**];

- Intensity; the amount of energy being transferred from the stream of particles to the work piece.
- Saturation; a measure of the amount of residual stress accumulated in the strip, obtained by plotting Almen strip displacement against exposure time
- Coverage; the percentage of the target surface that has been deformed by the shot peening stream in a given time, when viewed through a 10X magnifying glass

SAE AMS-S-13165 list the standard sizes for three different thickness Almen plates A, C and N, the selection of which depends upon the target component

thickness and the level of residual stress desired. All three types of plate are made from SAE 1070 steel with a hardness of 45HRC. The plates are 3inches (76mm) long and 0.75inches (19mm) wide.

The thicknesses are;

A 0.051inches (1.30mm)

C 0.0938inches (2.38mm)

N 0.031inches (0.79mm)

The plates are mounted in a fixture such as that shown in Figure 20 or on a dummy sample as shown in Figure 21. The sample holder surface must be flat and the strip is held in place with four clamping screws. After the strip has been shot peened, the strip is removed and the deflection at the centre of the length (arc deflection) is measured. The deflection is a measure of the intensity of the residual stress and the energy in the shot peen stream. The intensity is quoted in terms of the deflection and the strip used, for instance 12A would be for an A strip with a deflection of 0.012".

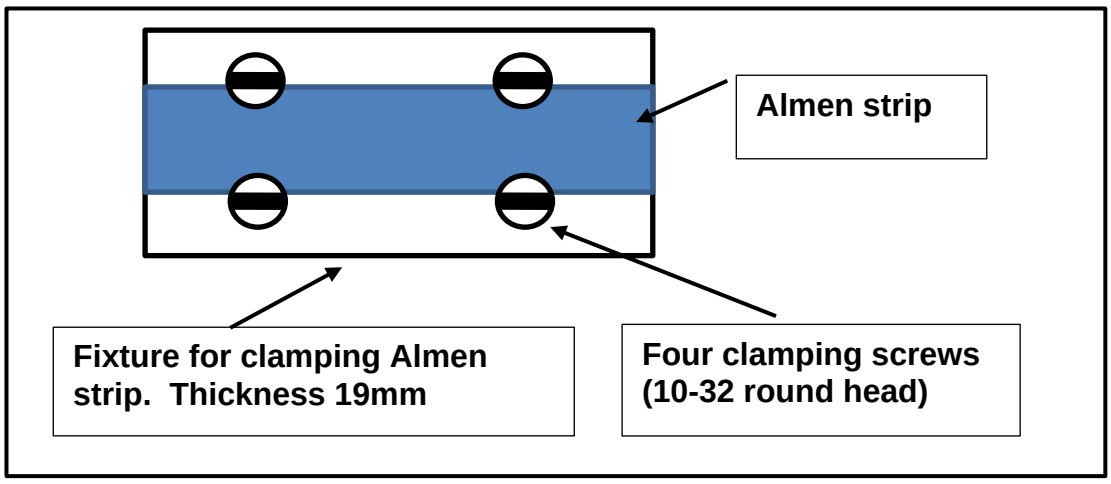

Figure 20: Recommended Almen test holding fixture arrangement according to AMS-S-13165 [18**]**

Figure 21: Almen strip location on old turbine blade with a fir tree root

In any new shot peening process a saturation curve has to be developed by using several Almen strips, exposed to the shot peening conditions for increasing times. Saturation is achieved when, as the exposure time for the tests strips is doubled, the arc height does not increase by more than 10%, as shown in Figure 22. Coverage of 100%, as determined with a 10X magnifier, is normally achieved close to the saturation point.

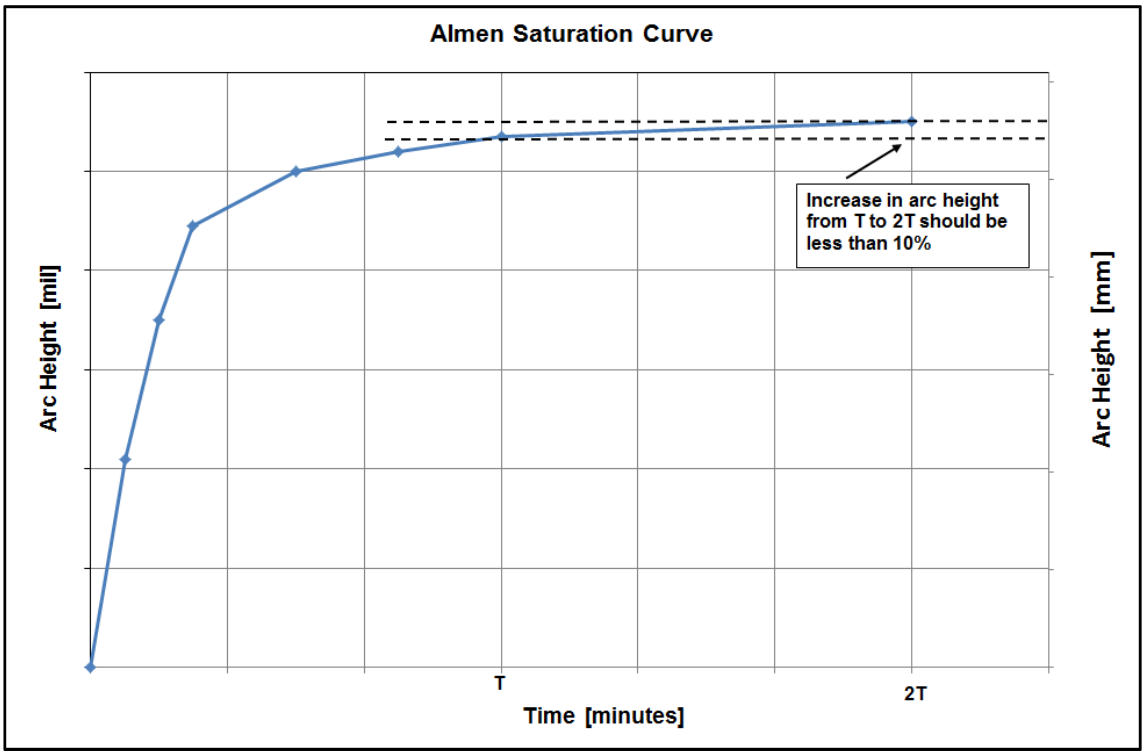

Figure 22: Almen saturation curve according to AMS-S-13165 [18**]**

2.2.1 Coverage

As stated previously 100% coverage is achieved when the complete surface of the target has been deformed by the shot peening stream in a given time, when viewed through a 10X magnifying glass. This is illustrated in Figure 23.

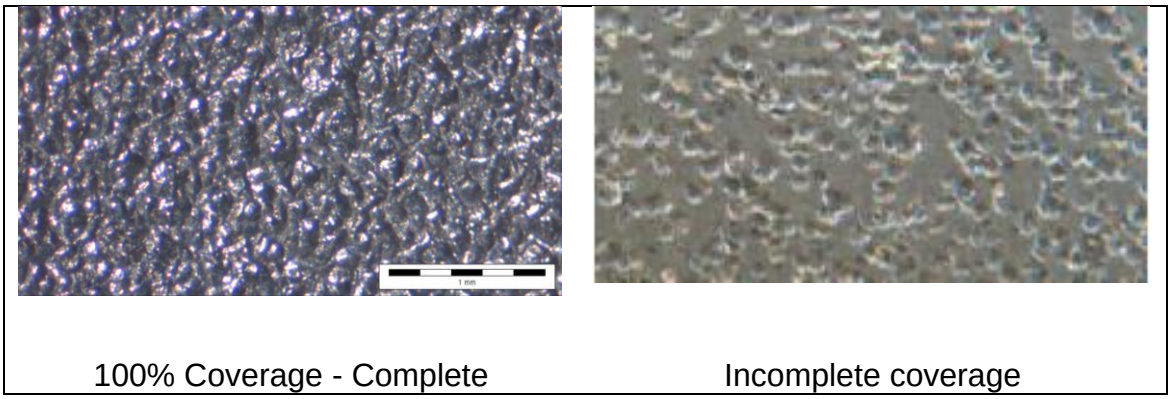

100% Coverage - Complete Incomplete coverage

Figure 23: Comparison of Complete and Incomplete shot peening coverage

In the case of the Eskom turbine blade failure referred to on page 5, the shot peening coverage was specified to be 200%. A key question was raised about the effectiveness of the Eskom guideline [**3**], and what the result of incomplete coverage would be. This influenced the experimental methodology choices, so that samples with coverage conditions of 75%, 100%, 150% and 200% were manufactured.

One of the disadvantages of over-peening to 200% is that there is an increase in surface roughness. In the case of the fir tree blade root configuration this can lead to interference problems during assembly of the blades on the shaft. It would be beneficial if the coverage could be reduced to 100%.

Work done by Prevéy and Cammett, [**20**], [**21**] showed that coverage below 100% was still very effective against fatigue. Their initial work was conducted

on aircraft quality 4340 (NiCrMo steel plate). Samples were prepared with coverage conditions ranging from 0.03T to 4T, where T represented the time to achieve 100% coverage. Their results, illustrated in Figure 24, showed that at 20% coverage the residual stress profile was well developed. Residual stresses were measured using laboratory XRD equipment and layer removal techniques.

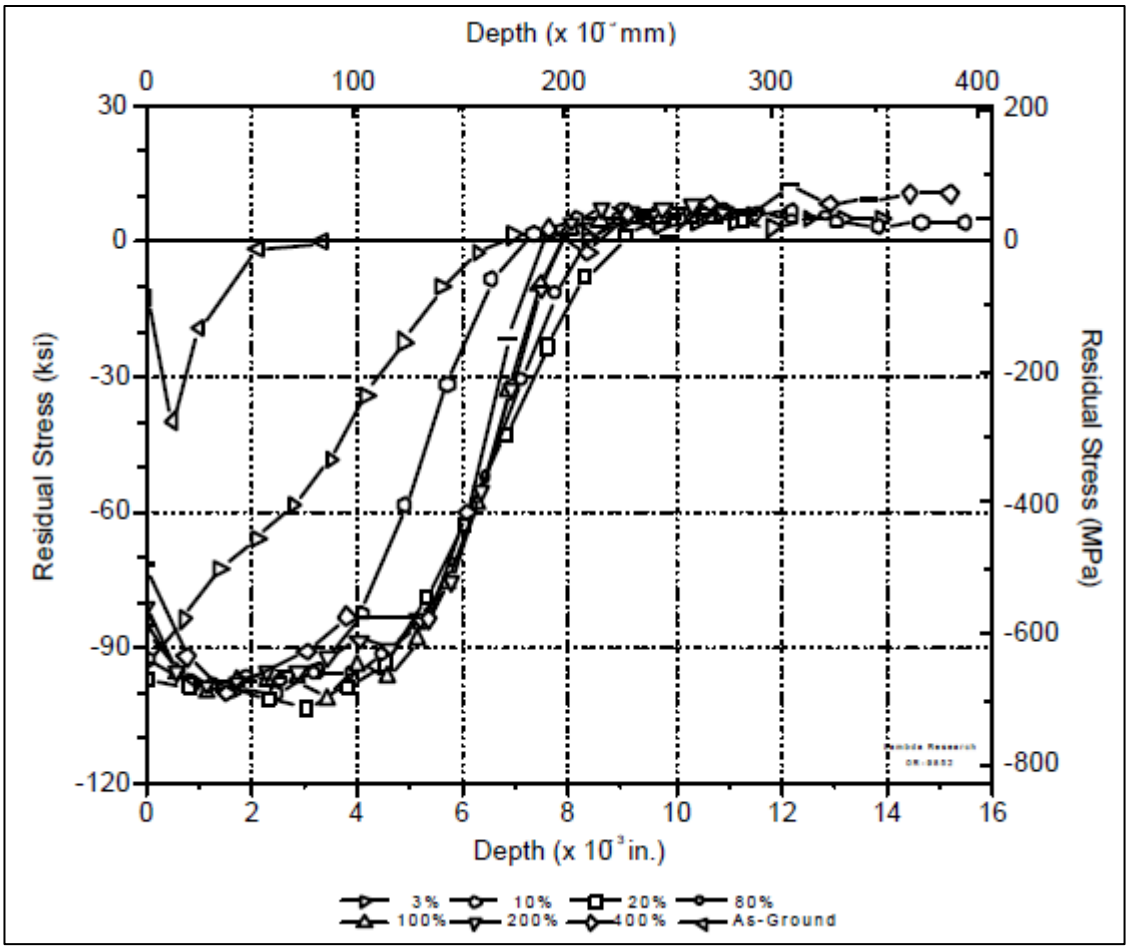

Figure 24: Extract from Prevéy and Cammett (fig 2) [20], showing residual stress profiles at different shot peening coverage conditions for 4340 steel plate. ***Permission to reproduce figure granted from of the International Scientific Committee on Shot Peening***

These results were unexpected and led to limited fatigue testing of the samples. Fatigue testing of samples with 20%, 100% and 300% coverage, in reversed bending with an R ratio of 0.1, showed that there was very little difference between the 20% and 100% conditions, with some loss of fatigue life at 300%

coverage, see Figure 25. This may be due to increased surface roughness and work hardening of the material.

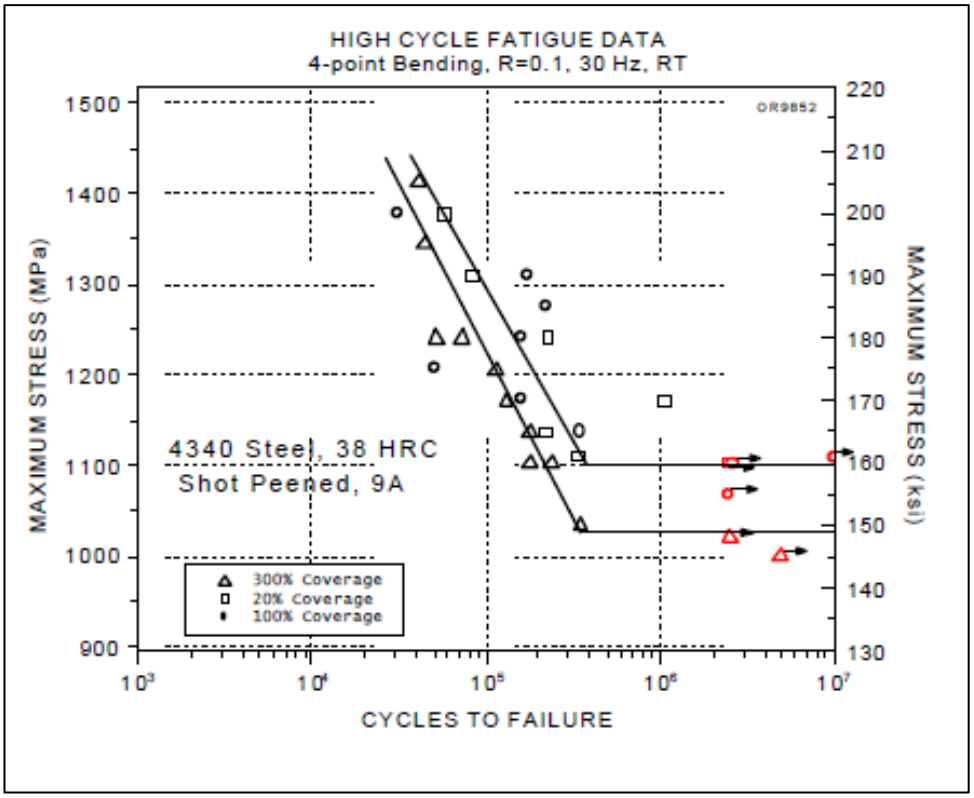

Figure 25: Extract from Prevéy and Cammett (fig 7) [20], showing high-cycle fatigue results for shot peened 4340 steel, 38 HRC, at 20%, 100% and 300% coverage. ***Permission to reproduce figure granted from the International Scientific Committee on Shot Peening***

Further work by Cammett and Prevéy on a Ni-base super alloy revealed similar results, with the stress profile at 0.1T (10%) already well developed, see Figure 26. The results published by Prevéy and Cammett [**20**], [**21**] contradict the work by Meguid [**22**] where his results showed that fatigue life on EN8 (SAE 1040) steel samples improved significantly with increased coverage as shown in Figure 27.

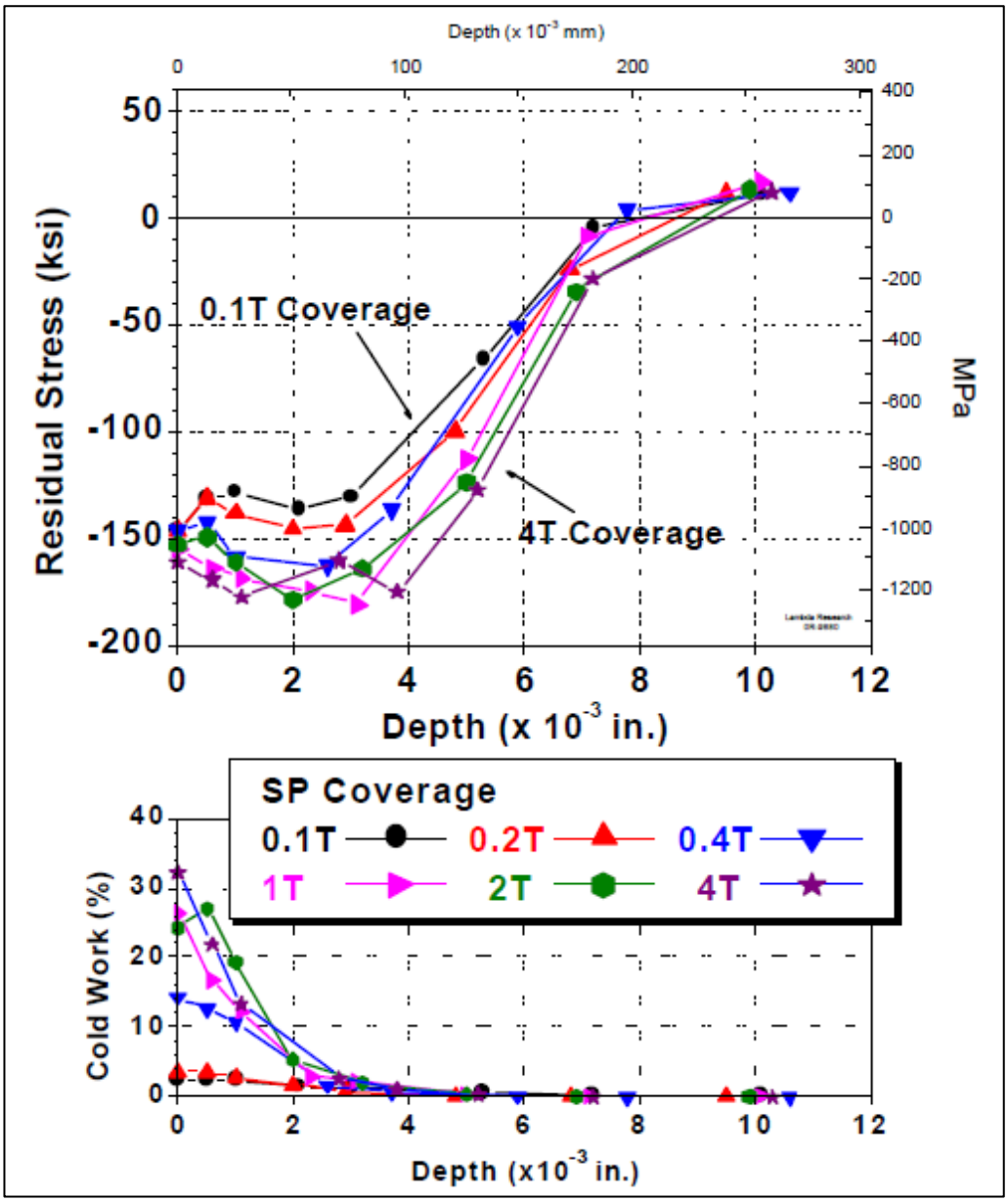

Figure 26: **Extract from Cammett and Prevéy (fig 1) [21], showing residual stress profiles at different shot peening coverage conditions for a Ni based super alloy IN718.** ***Permission to reproduce figure granted from the International Scientific Committee on Shot Peening***

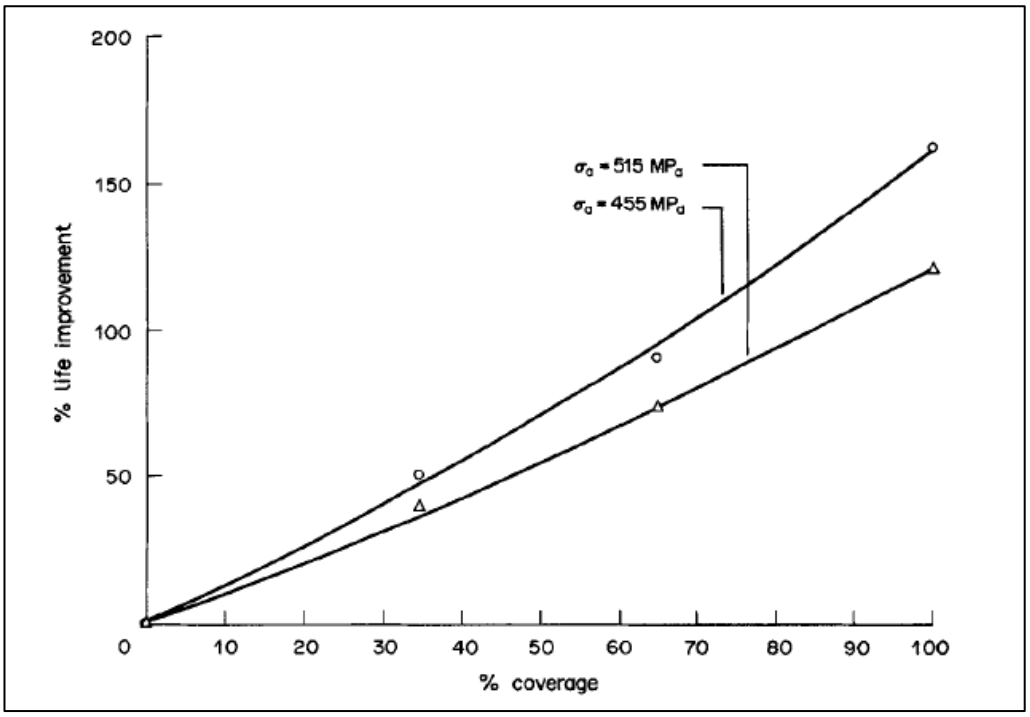

Figure 27: Extract from Meguid [22] showing the relationship between %coverage and %fatigue life improvement, R = -1 ***Permission to reproduce figure granted from John Wiley and Sons***

Kirk and Hollyoak [**23**] conducted an experiment to investigate the results obtained by Prevéy and Cammett using samples that had been peened in a very controlled manner. Samples were manufactured from hot rolled mild steel in a rectangular section, 40mm by 3mm. A 2mm indenter was used to apply precise loading of 70kgf (686.7N) on the samples, resulting in a dimple of 0.67mm diameter. Two sets of samples were manufactured; the first set had arrays of indentations with different separations to simulate different coverage conditions, while the second set had a single line of indentations with two different separations.

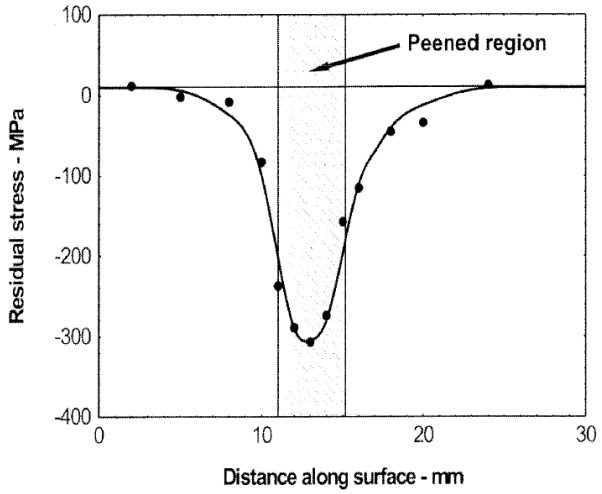

Surface residual stress profile across array of indentations

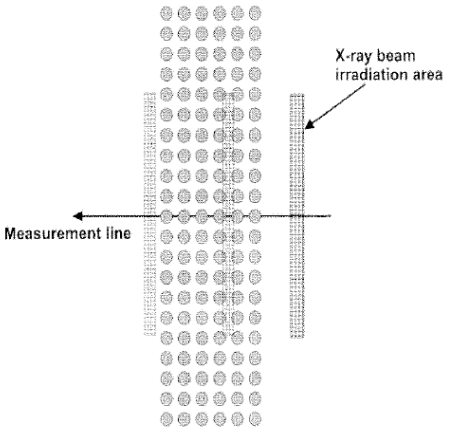

Array of indentations representation 100% coverage

Figure 28: Extract from Kirk and Hollyoak [23], showing the residual stress profile across an array of indentations on a 3mm thick sample. ***Permission to reproduce figure granted from the International Scientific Committee on Shot Peening***

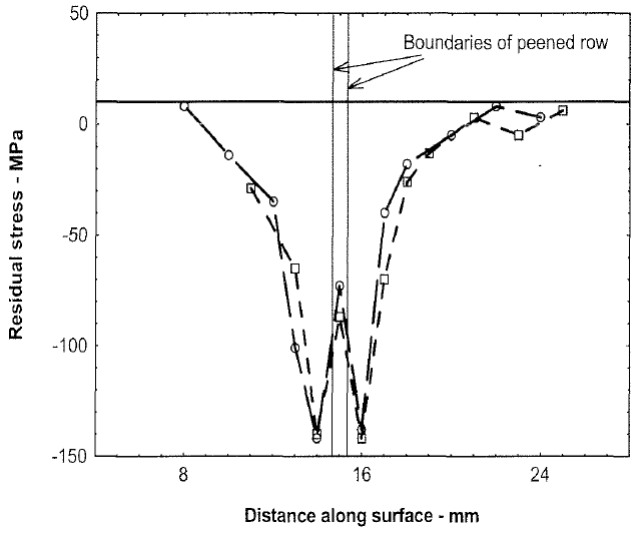

Surface residual stress profile across single row of indentations

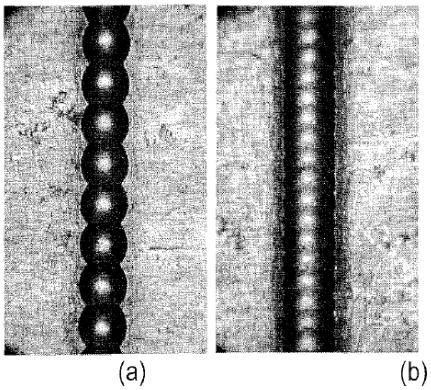

Single row of indentations.
(a) spacing 0.5mm
(b) spacing 0.25mm

Figure 29: Extract from Kirk and Hollyoak [23], showing the residual stress profile across a line of indentations on a 3mm thick sample. ***Permission to reproduce figure granted from the International Scientific Committee on Shot Peening***

The data shown in Figure 28 showed that for the array of indentations the compressive residual stress profile extended approximately 5mm outside the

indentation area. A similar pattern was measured on the single rows of indentations as shown in Figure 29. This information is very useful in explaining the formation of residual stress profiles in partial coverage conditions.

The fatigue results recorded in the preceding papers by Prevéy and Cammett [**20**], [**21**] Meguid [**22**] used reversed bending on fatigue samples. This type of loading is not well suited to shot peening evaluations as the compressive load cycle of the bending load is superimposed on the shot peened residual stress, which can cause localised yielding. In addition the results do not take into account local notch-induced constraints on a structure such as exist in the top serration of the turbine blade fir tree root. Prevéy and Cammett did however use an R ratio of 0.1 whereas Meguid used an R ratio of -1.

More recently a study by Soady et al [**24**] focussed on the effects of low cycle fatigue on notched samples loaded in a three point bend jig, with the notch being loaded in tension on each load cycle. The samples used were manufactured from turbine blade material similar in content to that being used in this thesis. Shot peening conditions were specified at 200% coverage with the intensity varying at 4A, 13A and 18A. The 13A intensity was the standard used for comparison. Two different notch radii, 4.5mm and 10.5mm, were also used.

The work by Soady et al [**24**] is directly relevant to that done in this thesis as the notch configuration is very similar to the fir tree root serration. The data shown in Figure 30 correlates very well with the results from the FE model for the overspeed conditions shown in section 5.6, where a more detailed comparison is presented.

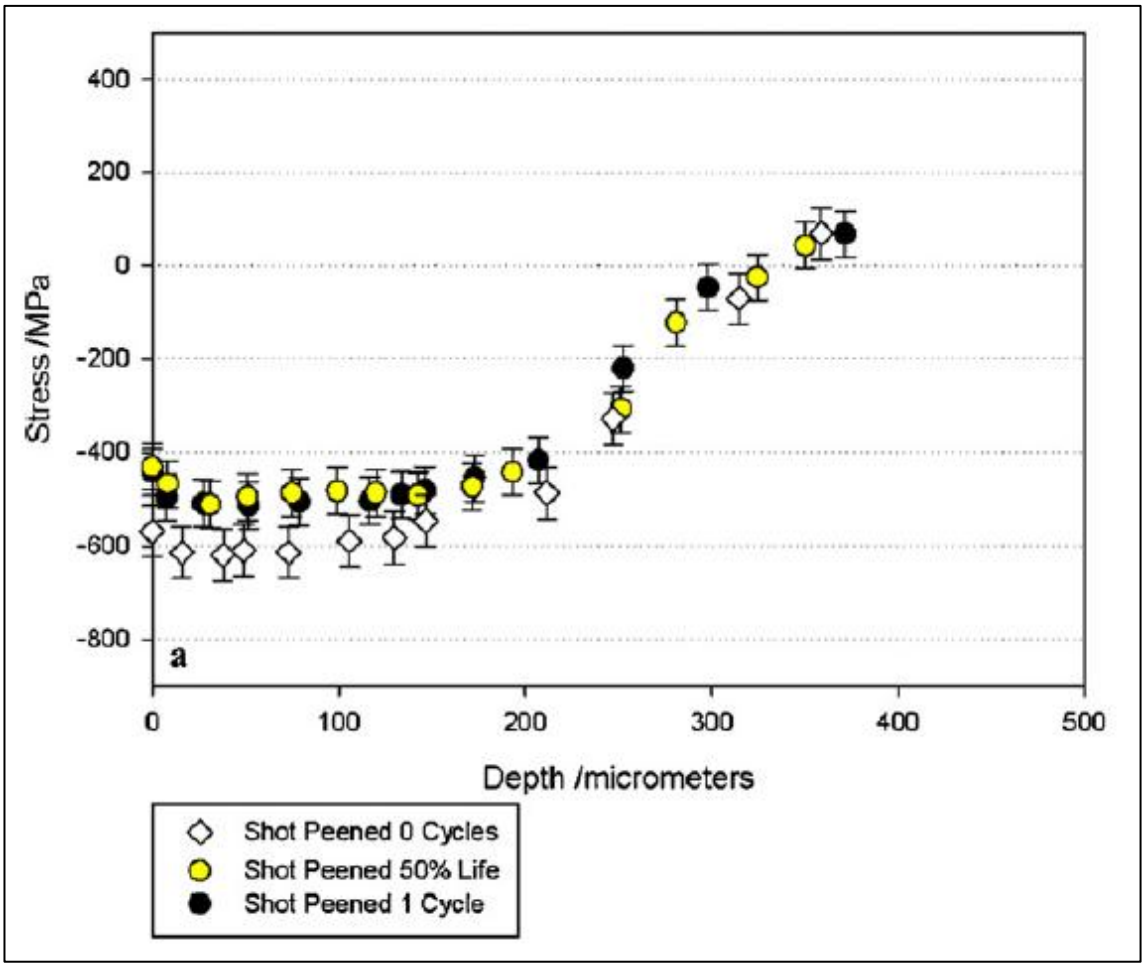

Figure 30: Extract from figure 9, Soady et al [24] showing the through-thickness stress profile for 0 cycles, 1 cycle and at 50% of life. ***Permission to reproduce figure granted from Elsevier***

The conclusions of the study relevant to this thesis are summarised below;

- Shot peening of notched samples increases the total fatigue life, even when operating in low cycle fatigue conditions.
- Cyclic plastic deformation of a notched shot peened component under three point bend results in the retention of any near-surface compressive residual stresses (for example resulting from the shot peening process) in the direction of loading and relatively small relaxation in the orthogonal direction (to approximately 80% of the original value).

2.3 Residual stress

Residual stress is the internal stress remaining in a body when no external loads are applied. The stresses are caused by distortions or misfits in the structure that are constrained by the structure itself on either a macro or micro scale [**25**]. Macroscopic residual stresses (Type I) would occur over several grains, whereas microscopic residual stresses occur over one grain (Type II) or on an atomic scale (Type III). These are illustrated schematically in Figure 31 extracted from a National Physical Laboratory (NPL) report [**26**]. This report was developed to provide a guide in the selection of residual stress measurement methods. Because of their size scale, macroscopic residual stresses are most relevant to fatigue performance of engineering structures. As the residual stresses are not due to external loads they are self-equilibrating over their characteristic distance [**27**].

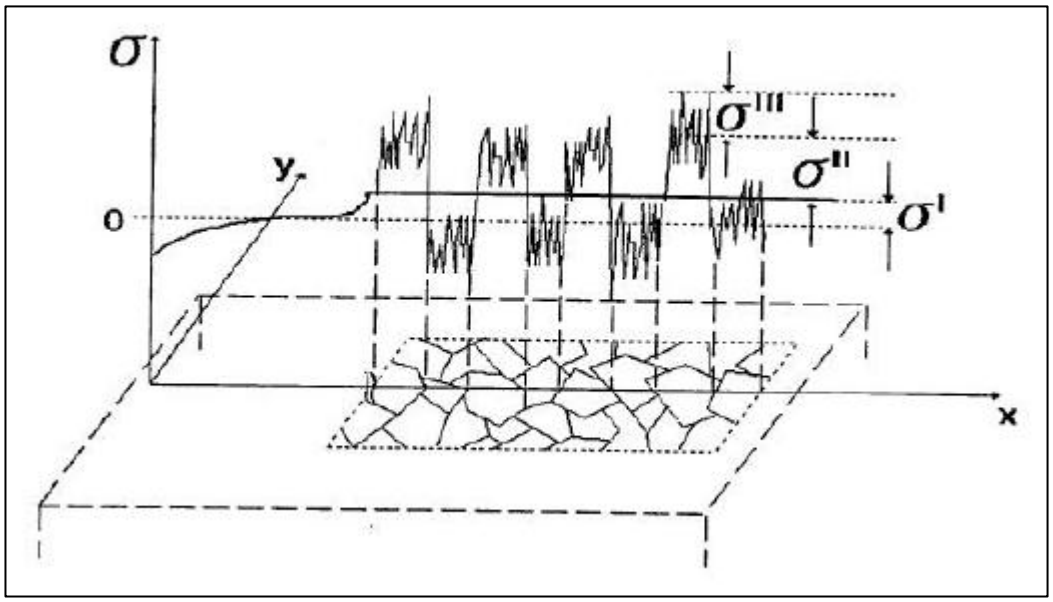

Figure 31: Extract from Fig 1 of report NPL Report MATC(A)04 [26**], illustrating the difference in the scale over which different residual stresses are applied.** ***Permission to reproduce figure granted from National Physical Laboratory, UK, Middlesex***

The differences between the different residual stresses is illustrated further in an extract from a useful review paper by Withers and Bhadeshia [**27**], shown in Figure 32. The diagram gives a good illustration of the differences between macroscopic and microscopic residual stresses.

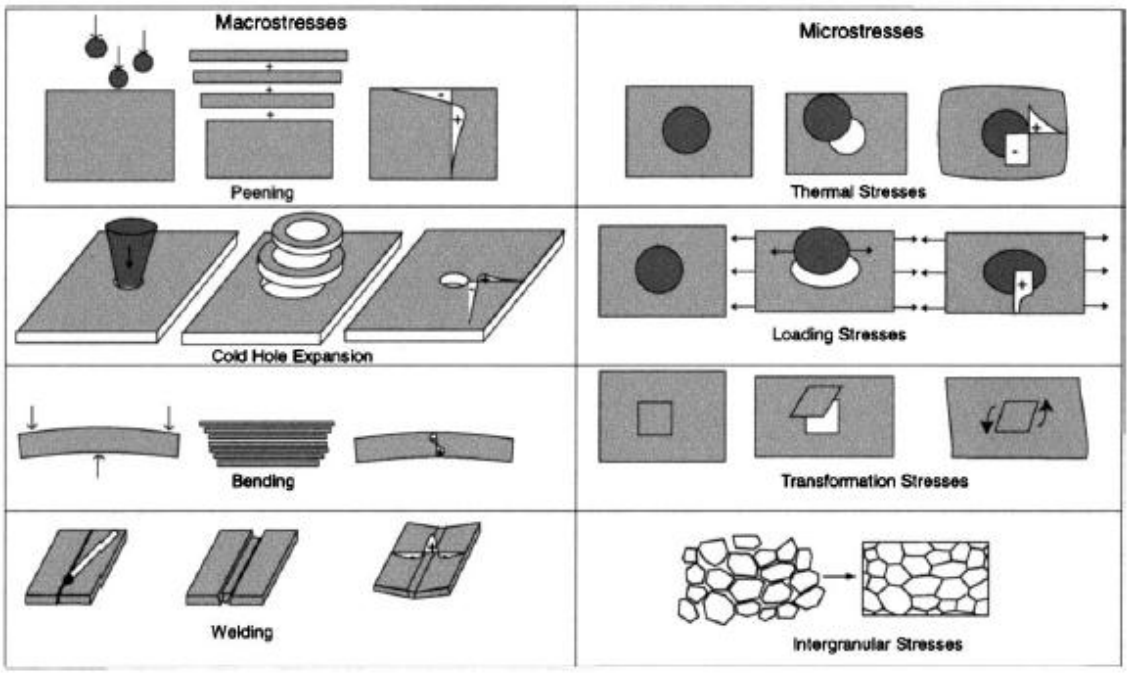

1 Residual stresses arise from misfits (eigenstrains) either between different regions or between different phases within material: different types of residual macro and micro residual stress are illustrated

Figure 32: Types of Residual stress listed by Withers and Bhadeshia [27**],** ***Permission to reproduce figure granted from Maney Publishing, http://maneypublishing.com/index.php/journals/mst/***

Residual stresses can be extremely harmful, particularly when combined with applied stresses, in circumstances when unexpected overloading may take place. On the other hand they can be highly beneficial if properly applied and quantified. In the case of shot peening the induced stresses are compressive and are beneficial both for fatigue and stress corrosion cracking [**4**], [**6**], [**24**].

The magnitude and distribution of residual stresses in a component or structure are a significant source of uncertainty in engineering design and can also affect subsequent machining as well as life prediction and assessment of structural reliability. Residual stresses are an unavoidable concomitant of almost all

manufacturing and fabrication processes and can also arise during service; they will occur under any set of circumstances that leads to differential expansion or contraction between adjacent parts of a body in which the local yield strength is exceeded. Their influence depends on their magnitude, sign and extent relative to the controlling length, area or volume of material associated with any particular mode of failure. Several illustrative examples of such influences are given in Figure 33 from James, [**28**]

Magnitude	Sign	Extent	Primary Effect	Induced Effect
Moderate to high	+ve or -ve	Component dimensions	Distortion during machining	Higher scrap rate Fretting and fatigue crack initiation
	+ve or -ve	Localised microstructure	Increase in dislocation density	Higher corrosion rates, e.g. in HAZ of welds in marine environment
	+ve or -ve	Component dimensions	Change in eccentricity of stress application along column	Change in buckling mode and load for welded columns
	-ve	Critical zone for crack initiation	Increase in resistance to fatigue cracking or fracture	Enhanced service life
	+ve	Component dimensions	Adds to tensile applied stress	Increased possibility of fast fracture in service
	+ve	Local defects, e.g. inclusions, weld defect	Decrease in resistance to fatigue cracking	Decreased service life
	+ve	Critical zone for crack initiation	Possibility of environmentally assisted cracking	Decreased service life

Figure 33: Extract from James (table 1) [28**], Illustration of the dependency of the effect of residual stresses on the mechanism of failure and on their magnitude, sign and extent**
Permission to reproduce figure granted from Elsevier

2.3.1 Measurement of residual stress

Residual stresses can be measured in a variety of ways, most of which are at least semi-destructive. The most common methods are listed in Figure 34 and Figure 35 below in extracts from NPL Report MATC(A)04 [**26**].

Measuring the effects of shot peening requires a method that is non-destructive and that is able to establish the profile with depth over the first 0.5mm. This requires a spatial resolution in the order of 30µm. The obvious choice would be synchrotron X-ray diffraction (SXRD), however access to this type of equipment can be difficult to obtain. Laboratory X-ray techniques can be used to complement the synchrotron experiment, either for surface measurements or semi-destructively using layer removal techniques. Neutron diffraction has the advantage of deep penetration into the sample, but the spatial resolution as shown in Figure 34 is approximately 500µm. At the ILL facility collimators are available down to 200µm, but this is still insufficient for determining shot peening residual stress profiles.

Technique Selector: Table 3 – Physical Characteristics

Key Techniques	Physical Characteristics							
	Resolution	Penetration	Stress Type	Stress State	Stress gradient	Uncertainty	Sampling Area /Volume	Remarks
Hole Drilling	50-100 µm depth increment	= hole diameter	Macro	Uniaxial Biaxial	Yes – difficult to interpret	Varies with depth	1-2 mm diam. 1-2 mm deep	
X-ray Diffraction	20µm depth 1mm laterally	5 µm – Ti 50µm – Al 1mm – layer removal	Macro Micro	Uniaxial Biaxial	Yes – with layer removal	Limited by several factors	0.1-1 mm^2 0.05-0.1 mm	Resolution for steel 1 mm diameter (min) 15µm depth
Synchrotron	20µm lateral to incident beam. 1 mm parallel	>500µm 100 mm - Al	Macro Micro	Uniaxial Biaxial Triaxial	Yes	Limited by grain sampling	0.1 mm^3	Measures strain only. Rarely possible to obtain stresses.
Neutron Diffraction	500µm	100 mm – Al 25 mm – Fe 4 mm - Ti	Macro Micro	Uniaxial Biaxial Triaxial	Yes	Limited by number of counts	>1 mm^3	
Curvature and Layer Removal	Depends on material & measurement method	Not applicable	Macro	Uniaxial Biaxial	Yes			Layer removal can be combined with other measurement methods such as XRD and magnetic to give information on stress profiles
Magnetic	1 mm	20-300µm (Barkhausen)	Macro	Uniaxial Biaxial	No		>2 mm^2	Sensitive to microstructure, anisotropy and texture.
Ultrasonic	5 mm	> 100 mm along specimen	Macro	Uniaxial Biaxial	No		1-400 mm^2	
Raman/ Fluorescence	0.5 µm	Surface	Macro	Uniaxial Biaxial				

Figure 34: Extract from Table 3 of report NPL Report MATC(A)04 [26**],**
Permission to reproduce figure granted from National Physical Laboratory, UK, Middlesex

Table 4: Advantages and disadvantages of the various techniques

Technique	PROs	CONs
Hole Drilling	• Quick, simple, • Widely available • Portable. • Wide range of materials • Deep hole drilling for thick section components	• Interpretation of data • Destructive • Limited strain sensitivity and resolution
X Ray Diffraction	• Versatile,widely available • Wide range of materials • Portable systems • Macro and micro RS	• Basic measurements • Lab-based systems, small components
Synchrotron	• Improved penetration & resolution cf X-rays • Depth profiling • Fast • Macro and micro RS	• Specialist facility only • Lab-based
Neutron Diffraction	• Excellent penetration & resolution • 3D maps • Macro and micro RS	• Specialist facility only • Lab-based
Curvature and Layer Removal	• Relatively simple • Wide range of Materials • Can be combined with other techniques to give stress profile	• Limited to simple shapes • Destructive • Lab-based
Magnetic	• Very fast • Wide variety of magnetic techniques • Portable	• Can apply to ferromagnetic materials only • Need to separate the microstructure signal from that due to stress
Ultrasonic	• Generally available • Very fast • Low cost • Portable	• Limited resolution • Bulk measurements over whole volume
Raman/Fluorescence	• High resolution • Portable systems available	• Surface measurements • Interpretation • Calibration • Limited range of materials

Figure 35: Extract from Table 4 of report NPL Report MATC(A)04 [26**].**
Permission to reproduce figure granted from National Physical Laboratory, UK, Middlesex

The basics of diffraction are covered extensively by Withers [**29**]. He states that "*Diffraction has become perhaps the most important non-destructive means of determining residual stress fields within crystalline materials and engineering components"*. Electron, X-ray, synchrotron or hard X-ray and neutron beams are used depending on the application and stress profile required. Depth of penetration and spatial resolution are two of the main distinguishing characteristics, when setting up an experiment. Table 1 summarises the beam properties as listed by Withers [**29**].

Property	Electrons	X-rays	Hard X-rays	Neutrons
Energy	200keV (100keV to 500keV)	Cu 9keV	35keV to 80keV	10meV (1meV to 100meV)
Mass (relative e^- mass)	1.4	0.017	0.150	1825
Wavelength (nm)	0.0025	0.154	0.015	0.29
Velocity (ms^{-1})	$2.1x10^8$	$3x10^8$	$3x10^8$	1400
Temperature (K)	$2.1x10^9$	$1x10^8$	$8x10^8$	12 116 580
Penetration in Fe	~100nm	~10µm	~10mm	~50mm
Gauge dimensions	5nmx5nmx100nm (thick)	1mmx5mmx0.01 mm (deep)	50µmx50µmx1000 µm	1mmx1mmx1m m

Table 1: Extract from Withers (table 1) [29**], summarising beam characteristics** ***Permission to reproduce figure granted from Elsevier***

The concept of using the crystalline lattice as an atomic strain gauge is explained, as shown in Figure 36. Changes in the lattice spacing either extensions or reductions can be measured by changes in the diffraction peak positions. Diffraction techniques can thus measure the strain in the material and the stress may be inferred using the material constants.

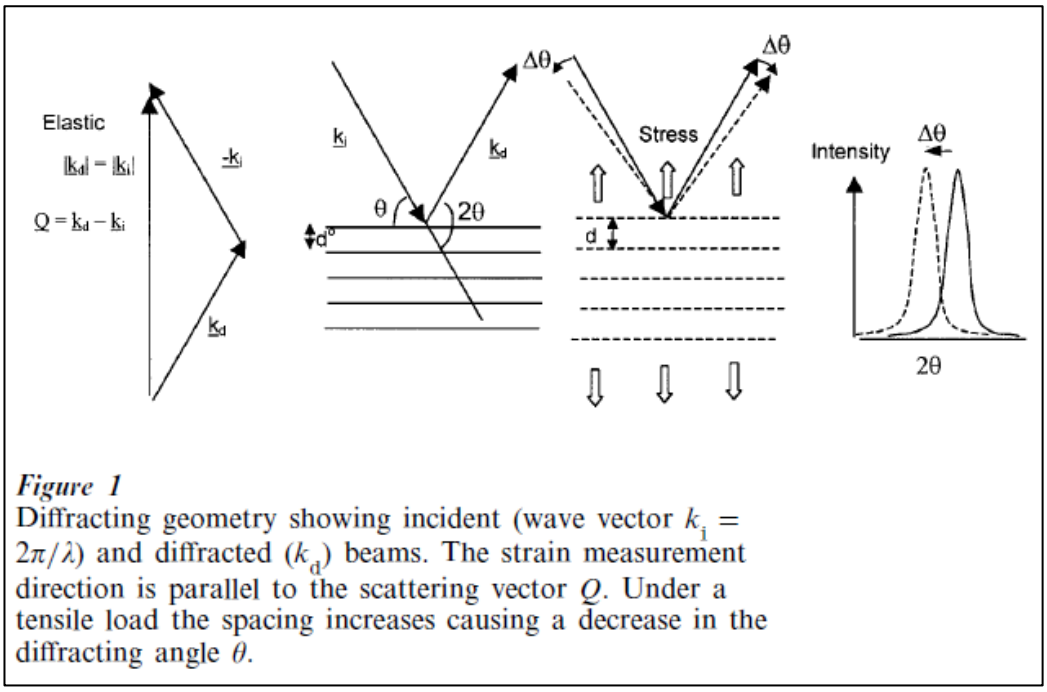

Figure 1
Diffracting geometry showing incident (wave vector $k_i = 2\pi/\lambda$) and diffracted (k_d) beams. The strain measurement direction is parallel to the scattering vector Q. Under a tensile load the spacing increases causing a decrease in the diffracting angle θ.

Figure 36: Extract from Withers (figure 1) [29], explaining diffraction strain measurement and reference axes. ***Permission to reproduce figure granted from Elsevier***

Strain may be measured by using either the reflected or transmitted beam as shown in Figure 37.

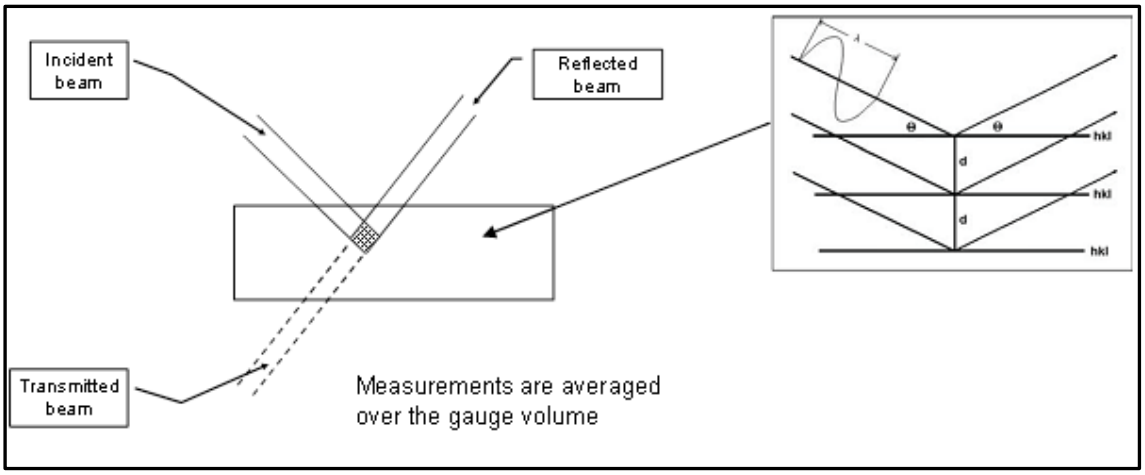

Figure 37: Schematic of diffracted beam

The changes in the diffracted angle are defined by Bragg's equation, [**29**], as shown in Equation 1.

$$\lambda_{hkl} = 2d_{hkl} \sin\theta$$

Equation 1 – Bragg's equation

where;
λ_{hkl} = incident wave length
d_{hkl} = lattice plane spacing
θ = half the scattering angle

The strain may be calculated from the difference between the measured spacing *d* and the strain free spacing d_0, divided by d_0.

$$\varepsilon = \frac{d - d_0}{d_0}$$

Equation 2 – Lattice strain

Withers [**29**] states that in neutron and synchrotron measurements the d_0 value can be determined or estimated in a number of ways; using powder samples, stress and moment balancing, annealed reference samples, comb samples or choosing an area that is as stress free as possible.

As stated by Hughes et al [**30**] *"Measurement of residual strain using neutron or synchrotron X-ray diffraction relies on the determination of the change in lattice parameter relative to a reference or "strain-free" lattice parameter"* . They investigated the use of comb samples, which typically have a cross section of 3mmx3mm and rely on the stress in the reduced sections being relieved during the machining process. In the case of the strain direction parallel to the length of the teeth there was convergence in the scattering angle for all teeth at the teeth ends. This corresponded to the value measured for the direction perpendicular to the teeth, and agreement was observed with a reference obtained by using force and moment balance across the full section. A typical comb sample used in a neutron diffraction experiment is shown below in Figure

38. The d_0 scans should be taken as close as possible to the end of the comb and if possible a number of scans should be averaged to obtain better accuracy.

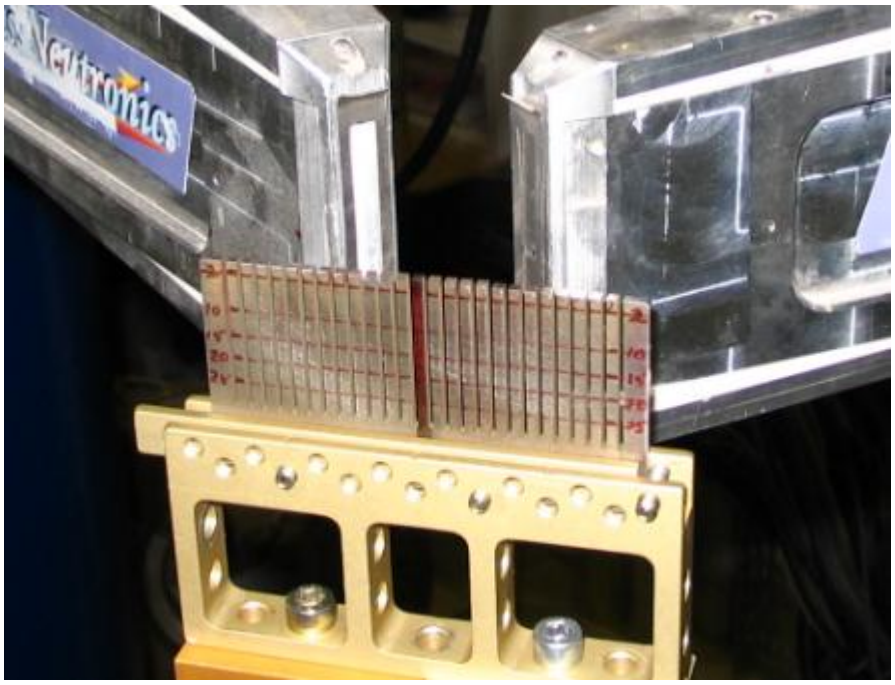

Figure 38: Comb sample from a neutron diffraction experiment. Cross section of fingers 3mmx3mm

Stress and moment balancing is often used as a cross check of the d_0 estimation [**29**], [**30**] and is very effective provided the specimen is homogenous and the strain free lattice is the same across the section. A welded joint would thus not be as suitable due to the changes in microstructure. In addition the measurement matrix should be designed so that through-thickness profiles have symmetrical spacing across the section being measured. This was the case in this thesis as the flat samples were shot peened on both sides simultaneously and the synchrotron beam was able to penetrate completely through the 5mm thickness.

In lab XRD measurements the d_0 problem described above can be overcome if the material properties are known so that the X-ray elastic constants can be calculated, and the $sin^2\psi$ technique is used to analyse the data [**29**], [**31**]. The technique is explained below and illustrated in Figure 39 and Figure 40.

As stated by Withers [**29**] and with reference to Figure 36, strain is a tensor quality and by making strain measurements in six directions the strain tensor can be calculated as follows;

$$\frac{\Delta d_{\phi\psi}}{d^0_{hkl}} = \sum_{i,j} l_i l_j \varepsilon_{ij} = \varepsilon_{11} cos^2\phi sin^2\psi + \varepsilon_{12} sin2\phi sin^2\psi + \varepsilon_{22} sin^2\phi sin^2\psi$$

$$+ \varepsilon_{33} cos^2\psi + \varepsilon_{13} cos\phi sin2\psi + \varepsilon_{23} sin\phi sin2\psi$$

Where l_i are direction cosines with respect to a Cartesian axis system (L_1, L_2, L_3) chosen to represent the sample geometry, ψ is the angle between Q and L_3 and ϕ is the angle between L_1 and the projection of Q onto the L_1L_2 plane. Refer to Figure 36.

Equation 3 – Strain tensor

For an isotropic material the X-ray elastic constants S_1 and S_2 may be calculated from the bulk elastic constants [**32**] as shown in Equation 4 below;

$$S_1 = \frac{-\nu}{E} \qquad \frac{1}{2} S_2 = \frac{1+\nu}{E}$$

Equation 4 – X-ray constants

where;
$E = Elastic\ \ Modulus$
$\nu = Poisson's\ \ ratio$

Equation 3 can then be rewritten in terms of stress and the elastic constants S_1 and S_2 [**29**]

$$\frac{\Delta d_{\phi\psi}}{d^0} = \frac{1}{2}S_2(\sigma_{11}cos^2\phi + \sigma_{12}sin2\phi + \sigma_{22}sin^2\phi - \sigma_{33})sin^2\psi + \frac{1}{2}S_2\sigma_{33}$$

$$+ S_1(\sigma_{11} + \sigma_{22} + \sigma_{33}) + \frac{1}{2}S_2(\sigma_{13}cos\phi + \sigma_{23}sin\phi)sin2\psi$$

Equation 5 – Strain equation

Since the normal stress must be zero at the surface, if the penetration distance is small, then the biaxial assumption is valid (leading to all σ_{i3} = 0). The difference in strain between that measured at (ϕ, ψ) and that normal to the surface, $\varepsilon_\perp$, is given by:

$$\varepsilon_{\phi\psi} - \varepsilon_\perp = \frac{d_{\phi\psi} - d_\perp}{d_\perp} = \frac{1}{2}S_2\sigma_\phi sin^2\psi$$

Equation 6 – Strain from $sin^2\psi$

The $sin^2\psi$ technique relies on the linear relationship between the lattice spacing and the sin^2 value of the angle of inclination (ψ) of the sample, as shown in Figure 39. Approximately ten data points should be recorded over a change in ψ of about 70°. The slope of the graph $d_{spacing}$ vs $sin^2\psi$, combined with the X-ray elastic constants will enable the stress to be calculated, as illustrated in Figure 40. The slope of the graph is proportional to S_2. The strength of this method is that it is independent of d_0, but the alignment of the beam is very important for a successful measurement as the focal point of the beam should not move to different points in the microstructure as the specimen rotates through the angle ψ.

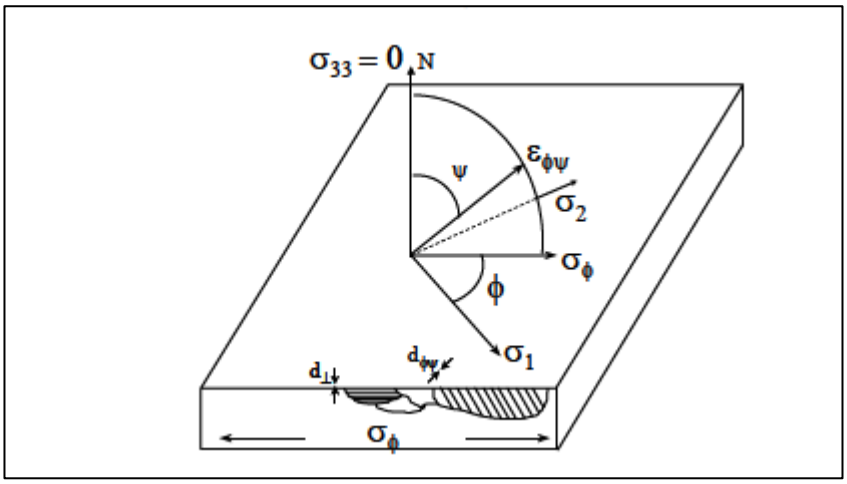

Figure 39: **Extract from NPL guideline (fig5.3) [33], schematic showing diffraction planes and angle of inclination ψ.** ***Permission to reproduce figure granted from National Physical Laboratory, UK, Middlesex***

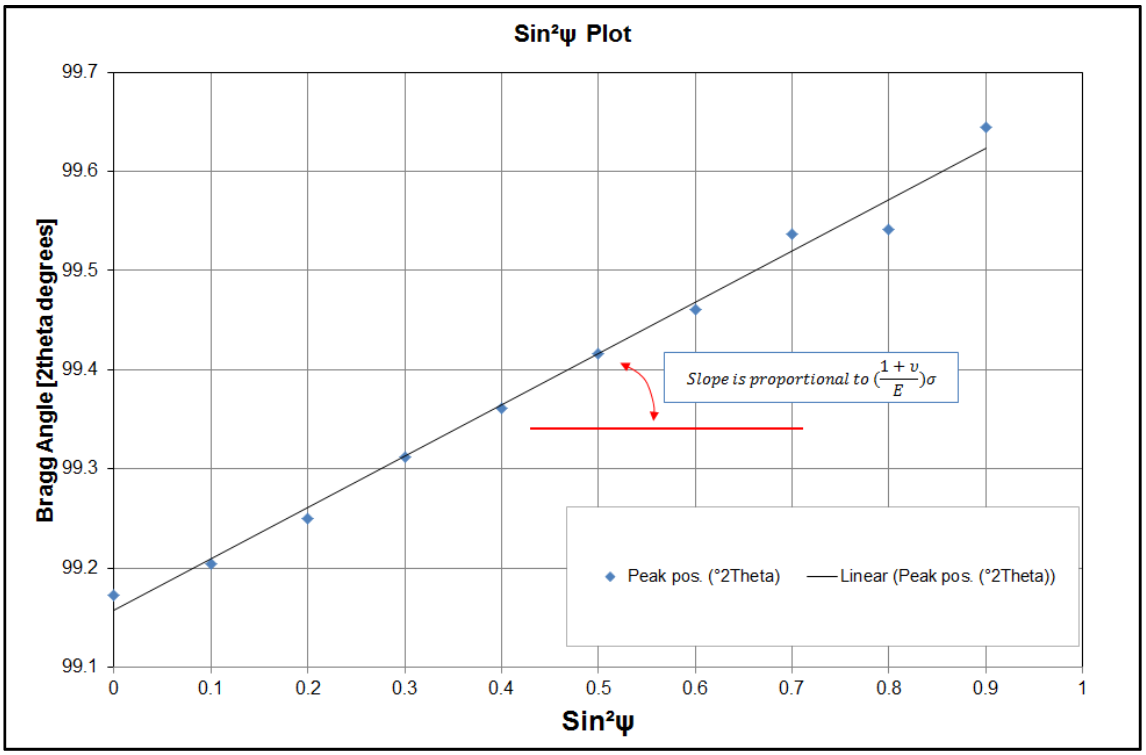

Figure 40: **Illustration of $sin^2\psi$ plot from a sample with a surface stress of -670MPa**

2.3.2 Layer removal

Layer removal with lab XRD measurements has been used by several authors as a method to determine the profile of residual stresses [**11**], [**21**], [**24**]. The recommended layer removal technique is electro-polishing [**34**] in order to avoid inducing spurious surface stresses. The chemicals generally used in a variety of electrolyte combinations, for stainless steels, are perchloric acid, orthophosphoric acid, sulphuric acid, acetic acid, ethanol and water [**35**], [**34**]. The specimen face that requires polishing is immersed in the electrolyte and connected as the anode. The cathode terminal may be inserted separately into the electrolyte, or connected to the container holding the electrolyte. When the correct voltage, current density, temperature and time are applied the result should be superior to mechanical polishing.

There are many variables that influence the results of electro-polishing, some of which are listed below;

- Size of sample (effect on current density).
- Initial state of sample surface (generally a 600 grit mechanical polish required to start).
- Voltage and current density.
- Cathode material.
- Position and orientation of sample in bath.
- Immersion time.
- Anode to cathode spacing.

There are some disadvantages to the process. The chemicals used are normally difficult to work with and require careful handling. This is particularly important due to the poisonous and explosive nature of some combinations of the chemicals. Perchloric acid falls in this category. A mixture of perchloric acid and acetic acid exploded in a Los Angeles factory in 1947, killing 15, injuring 400 and causing damage estimated at $2 million.

Figure 41 shows a triangular diagram from Palmieri [**36**] for perchloric acid, acetic acid and ethanol indicating the safe area of electrolyte mix and the larger danger area.

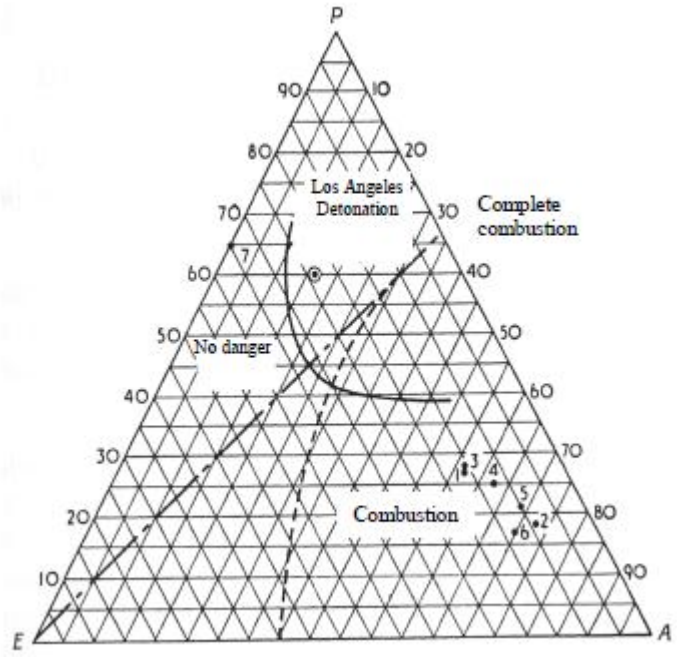

Figure 41: Triangular diagram of perchloric acid, acetic acid and ethanol [36**]. *Permission to reproduce figure granted from Dr V Palmieri***

Another potential problem for this study is that electro-polishing of multiphase alloys has been shown to be very difficult due to preferential attack of the carbide phases in the matrix [**34**].

Once a layer has been removed and the new surface stresses measured, compensation should be made for the change in structure of the specimen if necessary. This change can result in so-called ghost stresses as the existing residual stress changes when a layer of material is removed and the stress then redistributes in the remaining structure in order for equilibrium conditions to be maintained [**31**], [**37**].

2.3.3 Modelling of residual stress

In order to derive a technique for optimising shot peening on a turbine blade attachment area, it will be necessary to develop a finite element model that can replicate the measured residual stress profile and superimpose the operational centrifugal loading so that the possible degradation of the residual stress profile can be determined and hence the effect of fatigue and corrosion resistance assessed.

The mechanics of elastic impacts as developed by Hertz was found to be insufficient [**19**] for analysing the interaction of a shot ball impacting on a surface, due to the plastic deformation that takes place during shot peening, which results in non-linear behaviour. Initial methods of modelling shot peening simulated the effect of one spherical impact by applying pressure to the surface of an elastic/plastic finite element model [**15**], [**19**] and then releasing the pressure so that the constraint of the underlying layers could be applied. Kyriachou [**19**] reported that "*Modelling with Finite Element Methods has been found to be very versatile and a powerful means for investigating the shot-peening process. Although modelling cannot substitute experiments it provides*

the means for improving understanding of the mechanics of the shot-peening process".

A number of studies have been done in modelling the shot peening process, Meguid et al [**12**] report that early attempts involved a quasi-static analysis and that experimental tests to validate models showed that using a static ball to indent the surface did not give the same result as when the ball was dropped. The dynamic impact process creates a different plastic flow stress field. Later work applied multiple impact models and in the case of Meguid et al [**12**], a symmetry cell consisting of multiple identical shots was proposed and applied using the explicit commercial finite element code LS-DYNA.

Hong et al [**38**] report that modelling started from the early 1970's when the problem of modelling a rigid sphere indenting an elastic-perfect plastic half space was solved by Hardy, Baronet and Tordion [**39**]. The modelling is generally regarded as very difficult as the process is dynamic in nature, and in addition there are a large number of variables involved. These include the type and size of shot, angle of impact, velocity and extent of the coverage. Hong et al [**38**], also states that the FE method is limited in modelling the complexity of a stream of many shots impacting a target as well as the shot-shot collisions, and as a result the number of shots used in most simulations is low.

The development of discrete element modelling packages has opened up more possibilities for modelling dynamic events. Discrete element modelling is a method used in particle simulation, originally developed by Cundall et al [**40**], that is based on an explicit numerical analysis of the contact and motion of the

particles, and has to be used in conjunction with FE modelling for shot peening applications. Work has been published in this area in the last few years by a number of researchers including Meguid et al [**12**] and Hong et al [**38**]. Both used commercially available modelling packages, LS-Dyna and EDEM, to model the dynamic impact of the shot on the surface of the sample. Hong et al [**38**], in particular used discrete element modelling that allowed for modelling millions of impacts, previous studies had used multiple shots, but not a stream of discrete shots.

Very little work has been done in verifying the accuracy of modelling, using measured residual stress data, and none using full profiles across a sample as can be obtained from synchrotron experiments. In addition the application of modelling techniques onto curved surfaces has been limited.

An alternative technique of modelling residual stresses in structures is to use time dependent elastic plastic modelling of temperature quench processes. These techniques have been applied to structures such as railway lines [**41**] in order to analyse the internal stresses in a rail structure. Fata et al report *"First, with an initial temperature field and appropriate heat transfer boundary conditions specified, the heat conduction equations are solved to provide the temperature field as a function of time during cooling. Second, with specification of initial (usually zero) stress values, appropriate mechanical boundary conditions, mechanical properties as functions of temperature, and the temperature-time field from the first step, the equations of incremental plasticity are solved to obtain the time-dependent stress fields."*

Gür et al [**42**] modelled a steel cylinder made from C45 material that was quenched from 680°C into 20°C oil and obtained results that correlated well with neutron diffraction experimental results. This work showed that the technique could be applied successfully in a three dimensional sample, including curved surfaces, and uses the material phase transformation as part of the modelling process.

Generating a residual stress profile in the model of the fir tree root requires a technique that can be applied to the shape of the fir tree. Adapting the techniques listed by Fata and Gür [**41**], [**42**] and applying a transient thermal cycle, termed quench loading, to a model a thin plastic deformation layer will be generated on the surface of the structural model that will result in a compressive residual stress after the temperatures have returned to equilibrium.

Temperature quench loading of a simplified 2D plane strain finite element model will be used to generate a residual stress profile similar to that measured in the synchrotron experiments.

CHAPTER 3 SYNCHROTRON X-RAY DIFFRACTION EXPERIMENTS

The European Synchrotron Radiation Facility (ESRF) [**43**] is located in Grenoble, France and is a research institute focussing on cutting edge research with photons. The facility has twelve main member countries, with seven smaller contributors; the biggest shareholders are France, Germany and the United Kingdom. Beam time is allocated according to the scientific merit of applications, of which approximately 2000 are received annually.

Synchrotron radiation was detected in 1947 for the first time, at a particle accelerator at General Electric USA. It was only in the 1960s that the potential of synchrotron radiation as a source of bright X-rays was recognised, which led to the development of third generation synchrotron facilities in the late 1980s and early 1990s. This includes the ESRF, the Advanced Photon Source in the United States and SPring-8 in Japan.

X-rays are electromagnetic waves with short wavelengths of less than a nanometer due their position in the light spectrum. This makes X-rays suitable for the study of atoms and bonds. The principal difference between synchrotron light and the X-rays used in hospital is the brilliance: a synchrotron source is ten thousand billion times brighter than a hospital X-ray source [**43**].

Laboratory XRD machines are able to penetrate steels to a depth of approximately 15µm. Beam line ID31 at the ESRF can penetrate up to 7mm of steel and ID15A can penetrate approximately 70mm of steel. This is because the ESRF produces X-rays of high energy, called “hard” X-rays, which have

wavelengths of 0.10 to 0.01 nm or energy in the range 10 to 120 keV. (In synchrotron science, it is more usual to speak of energies.) Because of their higher energies, hard X-rays penetrate deeper into matter than soft X-rays, those with energy below 10 keV. The synchrotron X-ray beam can have other valuable properties, including time structure (so that it flashes), coherence (making it a parallel beam) and polarisation.

At the ESRF electrons emitted by an electron gun are first accelerated in a linear accelerator (linac) and then transmitted to a circular accelerator (booster synchrotron) where they are accelerated to reach an energy level of 6 billion electron volts (6 GeV). These high-energy electrons are then injected into a large storage ring where they circulate in a vacuum environment, at a constant energy, for many hours.

X-ray photons are initially accelerated in a linear direction, in a linac, and then guided into the synchrotron ring, which is actually a “n” sided polygon. The photons travel in a vacuum tube and are forced to change direction by undulators at each of the “n” corners of the polygon. Each time these electrons pass through an undulator, a device consisting of series of alternating magnets, they emit X-rays which because of their high relative light speed (~0.6c) are tightly focussed and can be directed along beam lines. The diameter of the ring is 300m, and a number of beam lines extract X-rays tangentially to the ring for different scientific purposes at each undulator position; there are currently forty nine different beam lines open or being commissioned supporting a variety of different scientific areas, see Figure 43.

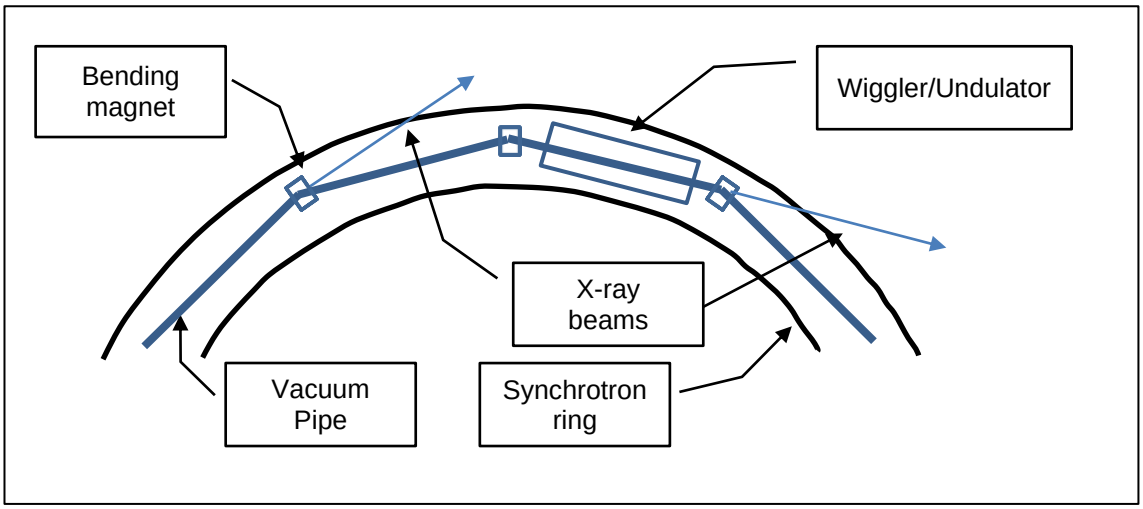

Figure 42: Schematic of synchrotron ring where bending magnets guide the electron beam around the ring and X-ray beams are taken off at the magnets or at wiggler/undulators

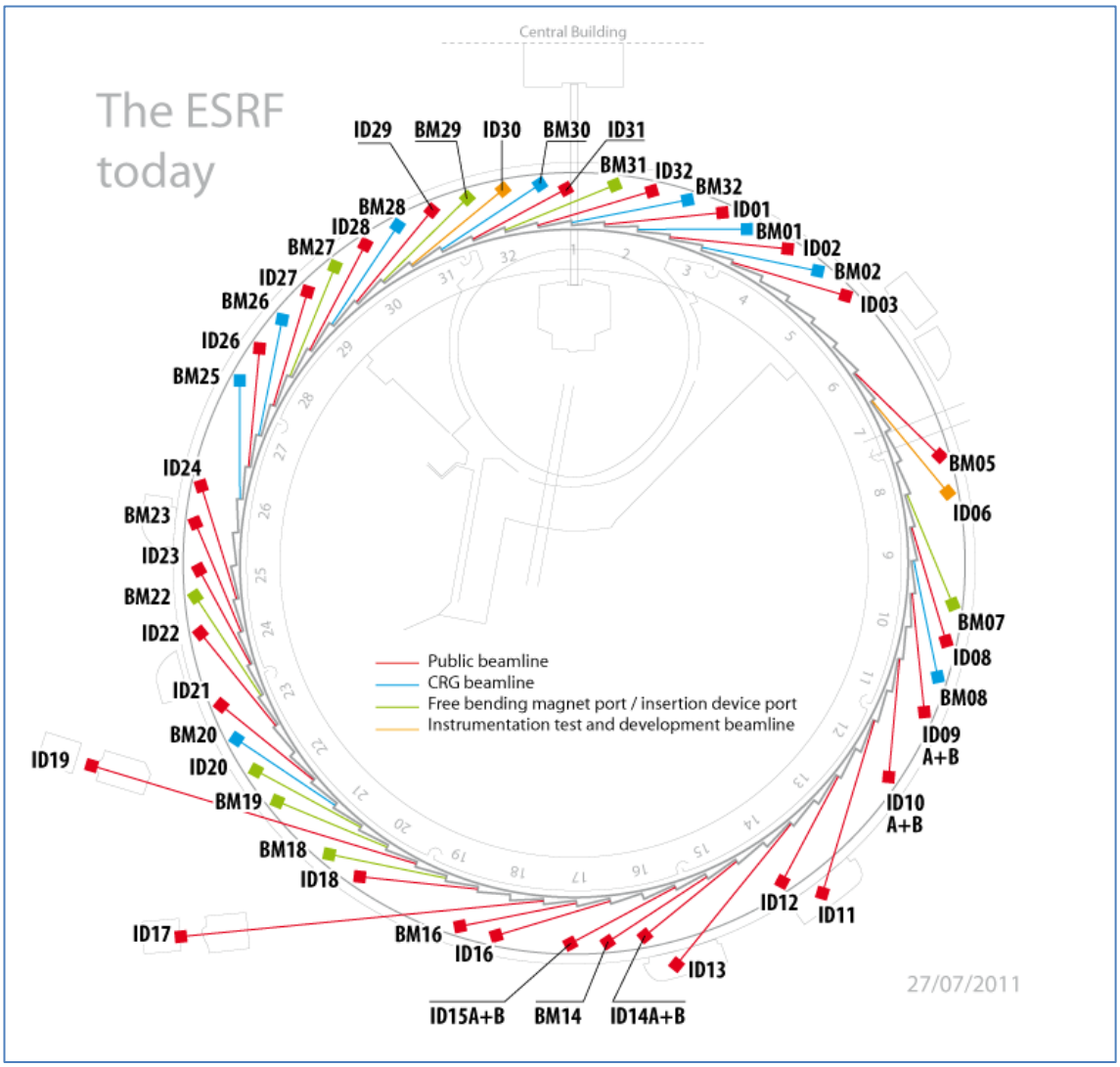

Figure 43: Layout of ESRF beam lines *(courtesy ESRF website)*

Two of the beam lines, ID31 and ID15A cater to research into materials using diffraction techniques, and more specifically residual strain measurement.

3.1 Beam Line ID31 – Experiment MA326

As explained above, the ESRF synchrotron produces hard X-rays at energy levels high enough to penetrate steel samples. Beam line ID31 has a mono-chromated beam with energy levels in the 5 to 60keV range. These energy levels allow for transmission diffraction experiments on steel samples of approximately 7mm thickness. The diffracted beam angle is measured by a precision detector as shown in Figure 44. The beam line configuration allows for the diffracted beam to pass through Si_{111} crystals before arriving at an array of detectors. This gives a very well defined beam with narrow peaks and combined with the mechanical integrity of the diffractometer results in small systematic errors and peak positions reproducible to a few tenths of a millidegree.

Advantages of the SXRD Technique:

- "Non-destructive" technique (although d_0 samples may need to be extracted or beam access windows cut)
- Good penetration depths – 20mm in steel, 100mm in aluminium (total beam path lengths)
- Tri-axial residual stress measurements by specimen manipulation
- Small gauge volume (typically <1mm^3) and thus suitable for measuring stress gradients
- High magnitude residual stresses are measured accurately

- Complex shapes can be measured, although beam access windows may need to be cut
- Indifferent to surface finish
- Nominal accuracy: 10MPa – Aluminium, 30MPa – Steel, 15MPa – Titanium
- Fast measurement process
- Macro and micro stresses measured.

Disadvantages of the SXRD Technique:

- Laboratory based measurements with specimen size and weight restrictions
- Only applicable to polycrystalline materials
- Accuracy affected by grain size and texture
- Very long lead times before measurement unless beam time paid for commercially
- Elongated gauge volume.

The peak positions are typically analysed using the LAMP software developed at the ESRF. The software reads in the measurement matrix and applies a curve fit methodology chosen by the user (Gaussian, Lorentzians or Pseudo-Voight) which determines the peak position, height, full width at mean height and background, as well as the associated errors. A typical output plot and data table is shown in Figure 45. In the ID31 configuration a setup angle of approximately 45° is subtracted from the centre position angle leaving a 2θ value of approximately 10°, depending on material type and residual stress magnitude.

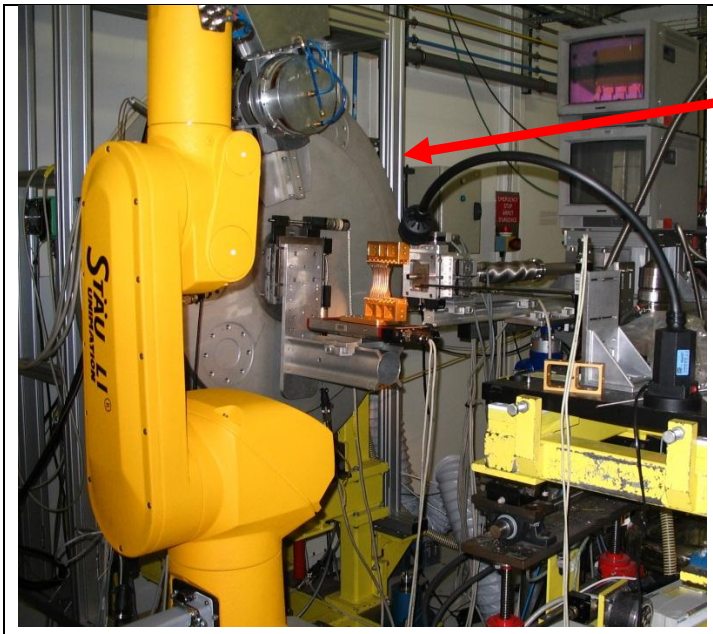

View of ID31 hutch with samples in position for measurement for experiment MA326

Close up of diffractometer *(courtesy ESRF website)*

Figure 44: ID31 Beam line

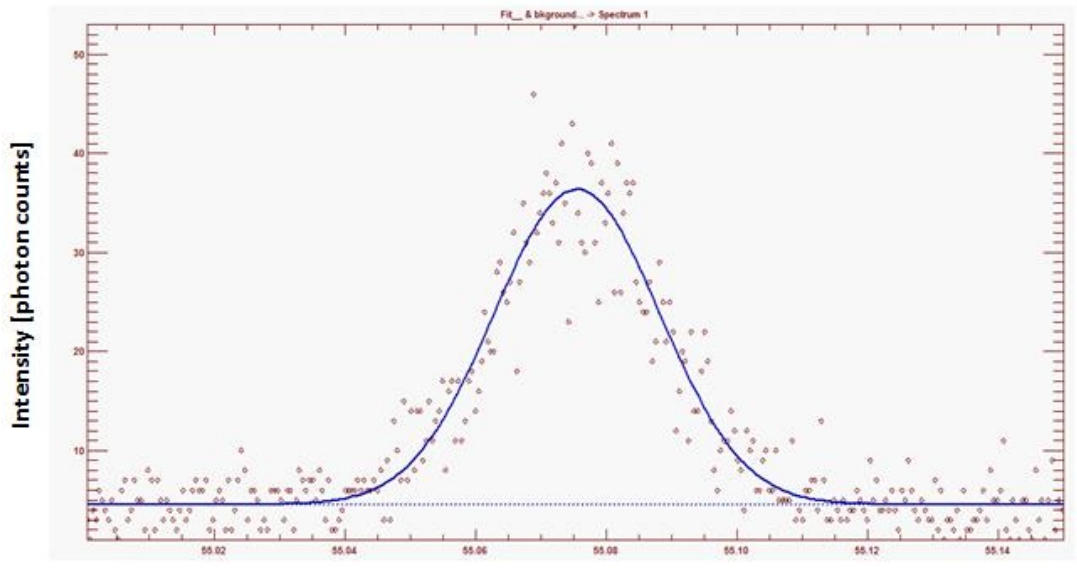

P1.height	error	P2.center	error	P3.fWmH	error	background	error
31.7562	0.629683	55.07548	0.000277	0.02971	0.000734	4.657224	0.255857

Figure 45: Typical diffraction peak recorded on ID31 (scan time approximately two minutes). Error is listed for each reported data set

3.2 Beam Line ID15A - Experiment ME1165

The experimental work on ID31, generated data that quantified the as-peened residual stress state very accurately. Unfortunately the fatigue tests yielded limited data as the loading parameters were too high. The maximum stress of 888MPa that was reached during the fatigue cycles was above the 0.2%yield point by 20MPa, this yielding across the specimen section resulted in a rapid loss of residual stress. A further opportunity was exploited to test one of the spare samples on beam line ID15A, during part of a long term experiment ME1165.

ID15 A is more powerful than ID31 with energy levels between 70 and 400keV and in addition it is equipped with two detectors, which allows for two strain directions to be measured simultaneously. The beam line uses an energy dispersive arrangement that results in a range of Bragg reflections being collected together by means of a solid state Germanium detector. The strain vector is then calculated from an average of these reflections.

Upgrades since 2004 include;

- Sample positioning system for specimens up to 400kg
- Instron 25kN tensile testing frame that can be mounted on the sample positioning system
- Vacuum oven (up to 1200°C) with integrated 5kN tensile testing machine
- Cryo-magnet for martensitic transformation studies
- Mirror based focussing lamp for studying thermal barrier coatings
- An industrial robot for manipulating non-regular samples

The strain vectors recorded from either ID31 or ID15A instrument allowed for the material stress to be inferred using the formulae shown below, under the assumption of an equi-biaxial stress state [**33**], [**44**]. For the equi-biaxial stress state, the longitudinal and transverse stresses from the shot peening are equal and the normal or through-thickness stress is zero, thus the through thickness strain is caused by the Poisson's ratio effect from the longitudinal and transverse stresses.

The strain was calculated from Equation 1, Bragg's equation, using θ, half the recorded scattering angle and the wave length of the beam. The longitudinal stress can be calculated from either the measured longitudinal strain or the measured through-thickness strain according to formulae 7 and 8 below.

$$\sigma_l = \frac{E(1+\nu)}{(1-\nu^2)}\varepsilon_l$$

Equation 7 – Longitudinal stress from longitudinal strain vector

$$\sigma_{lt} = \frac{-E.\varepsilon_t}{2\nu}$$

Equation 8 – Longitudinal stress from through-thickness strain vector

where;

$\sigma_l = longitudinal\ stress\ from\ longitudinal\ strain$

$\sigma_{lt} = longitudinal\ stress\ from\ through-thickness\ strain$

$\varepsilon_l = longitudinal\ strain$

$\varepsilon_t = through-thickness\ strain$

$E = Elastic\ Modulus$

$\nu = Poisson's\ ratio$

CHAPTER 4 EXPERIMENTAL METHODOLOGY

All the samples cut from a single turbine blade, i.e. twelve flat samples and three fir tree samples, were exposed to controlled shot peening conditions that were representative of industry standards for turbine blades. The Eskom guideline [**3**] was used to determine the shot peening parameters as discussed in detail in section 4.3. The parameter that was varied on the flat samples during the sample preparation was percentage coverage. The rationale behind this was discussed on page 11.

Residual strains were measured in the samples in two orthogonal directions in the as-peened condition and again after fatigue loading. Results will indicate the range of peening conditions necessary to achieve high compressive residual stresses and adequate depth of peened layer to resist relaxation during subsequent fatigue cycling. Finite element modelling was used to develop a predictive tool that links shot peening conditions to fatigue life via the residual stress distribution. The methodology is broken down into a number of sections below.

4.1 Description of material

The material that was used to manufacture the samples was 12CrNiMo martensitic steel, Din No 1.4939, and a trade name of Jethete [**2**]. This material is a creep and corrosion resistant, hardened and tempered steel with an operational upper temperature limit of 560°C. It is widely used in the manufacture of steam turbine blades, particularly low pressure turbines. It has

exceptional toughness and creep rupture strength. A typical microstructure is shown in Figure 46.

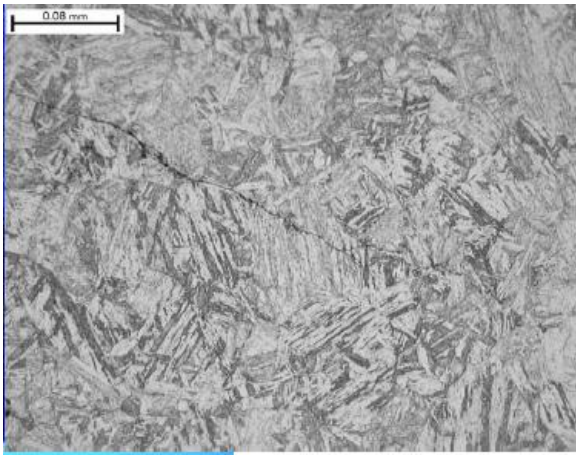

Figure 46: Typical martensitic microstructure from a cracked turbine blade

The average chemical composition of the material from the manufacturer's data sheet is shown in Table 2. Mechanical tests were conducted on three specimens cut from the material and the average results are show in Table 3 below.

C	Si	Mn	Cr	Mo	Ni	V	N
0.12	0.20	0.80	11.70	1.70	2.70	0.30	0.04

Table 2: Chemical composition by percentage

0.2% Proof Stress [MPa]	UTS [MPa]	Elastic Modulus [GPa]
868	1048	204

Table 3: Measured material properties from tensile tests

4.2 Sample preparation

All the samples were cut from a single used turbine blade, shown in Figure 9, to ensure minimal variation in material properties. Twelve flat hour glass samples were machined as shown in Figure 8 and Figure 10 with a reduced cross section of 5x5mm. Three fir tree samples were machined as shown in Figure 12. Three tensile test samples, 5mm diameter, were prepared for determining material properties; i.e. elastic modulus, 0.2% yield stress and the ultimate tensile strength.

The fir tree and flat samples were all machined using electro-discharge machining, and then ground, to minimise machining stresses.

4.3 Shot peening process

The samples were shot peened at the South African Airways technical services division located at the OR Tambo airport in Johannesburg. Most of the turbine blades used in South African power stations have been treated at this facility.

The shot peening was conducted according to the guideline used by Eskom [**3**]. The guideline conforms to the shot peening standard SAE AMS-S-13165 and calls for six nozzles to be used during the turbine blade shot peening process. Only four nozzles can be used at any one time due to the shot peening booth configuration. Four of the nozzles were used to peen the concave and convex surfaces of the fir tree, then once they had completed this part of the shot peening process two of the nozzles were reconfigured and used to peen the un-serrated end face of the fir tree root. The nozzles were each mounted at

specific angles and heights, but all were located at standoff distances of 228.6mm (9”) from the blade or flat sample surface, as shown in Figure 47.

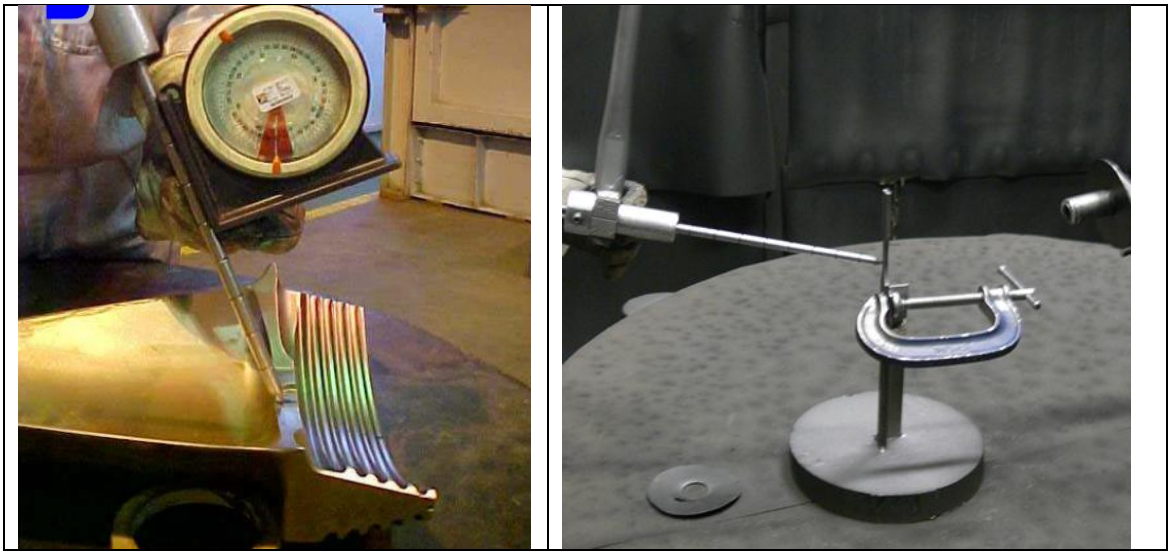

Figure 47: Illustration of how standoff distances were set before shot peening

Figure 48: Shot Peening chamber at South African Airways Technical Services

The flat samples were subjected to four different coverage conditions (75%, 100%, 150%, 200%). This resulted in three specimens for each coverage condition. The samples were shot peened from both sides simultaneously to prevent any bending of the sample and to allow for symmetrical analysis during the diffraction measurements. The standoff distance for the nozzles was set to 228.6mm and the angle of impact was 75°. The turntable, which rotated at 10rpm, was run for 6 minutes to achieve 100% coverage.

Three fir tree samples were made and mounted in an old blade as shown in Figure 12, in order to get conditions that closely simulated those experienced by a normal blade root during peening. As per the Eskom procedure the coverage in this case was 200%.

The six nozzles were mounted at specific angles and distances from the blade surface. The blade was mounted on a turntable, as shown in Figure 49, and as this rotated, the blade root area travelled through the nozzle matrix. The nozzles also moved up and down vertically during this process. When the system was being set up, a test blade with place for seven Almen strips was mounted on the turntable and the time required to achieve 100% coverage was measured, as shown in the saturation curve in Figure 51. This time was then doubled to obtain 200% coverage. The parameters for the blade are shown in Table 5 below.

The flat samples were treated in a similar way but only using two nozzles instead of six. The flat samples were mounted on the turn table as shown in Figure 47 and Almen strips used to determine the saturation curve shown in

Figure 50. The 100% coverage condition was determined to have taken place after 6 minutes of exposure. The samples were then treated to the four different coverage conditions as shown in Table 4 below.

SAMPLES	TIME	COVERAGE
1, 2 and 3	4.5 minutes	75%
4, 5 and 6	6 minutes	100%
7, 8 and 9	9 minutes	150%
10, 11 and 12	12 minutes	200%

Table 4: Flat sample shot peening exposure conditions

Figure 49: Turbine blade mounted on turn table inside shot peening chamber

PARAMETER	VALUE
Intensity:	8A-12A (deflection of 0.203 to 0.305mm)
Air Pressure:	Set to achieve Almen curve (32psi)
Distance from work piece	9”
Turn Table Speed:	10 rpm
Exposure Time:	Set to achieve Almen curve
Nozzle Size:	5/16”
No. of Nozzles:	6
Lance travel:	145mm (6.150”)
Lance cycles:	1.5 cycles for set distance
Recommended Shot Size:	CW28 = S-230 (or smaller) (0.023” = 0.584mm diameter)
Actual Shot Size:	S-170 (0.432mm diameter)
Coverage:	200%

Table 5: Shot Peening Parameters [3]

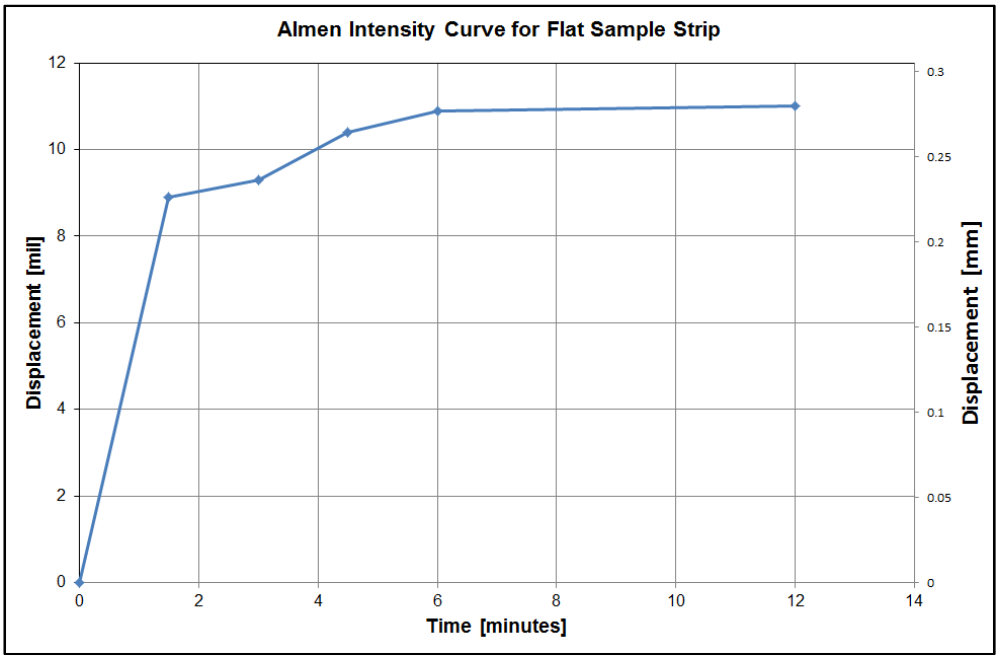

Figure 50: Saturation curve for flat sample Almen strips

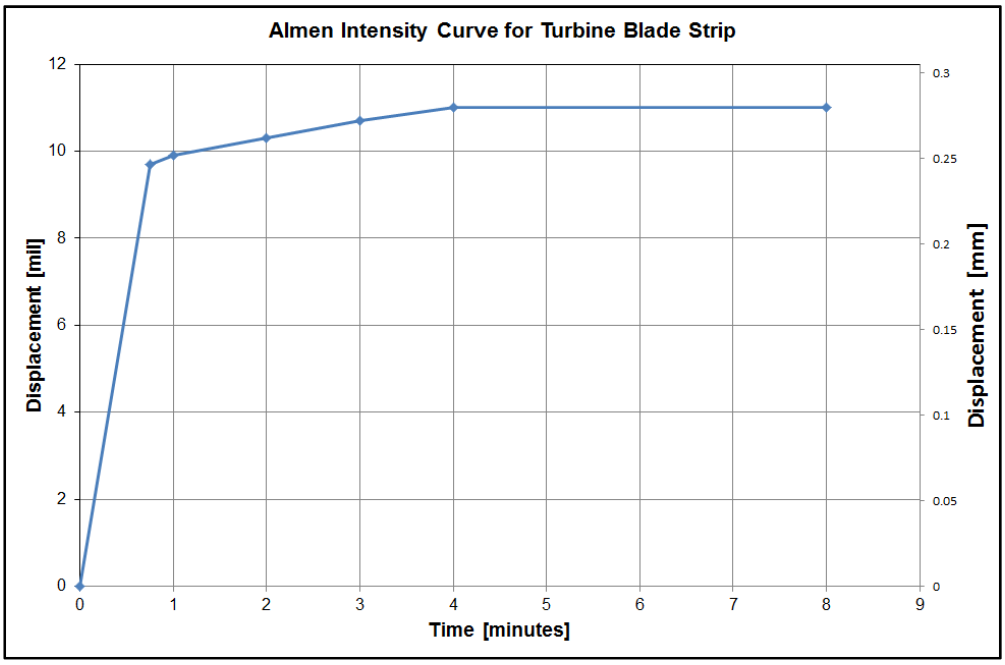

Figure 51: Saturation curve for turbine blade sample Almen strips

4.4 XRD measurements

The flat sample specimen design was oversized in length so that 20x20mm pieces at the end could be cut off. This then allowed the consistency of the shot peening to be checked using laboratory X-ray diffraction measurements, before the synchrotron tests commenced. The samples were analysed using a PANalytical X'pert Pro X-ray diffraction machine at Pretoria University in May 2007.

These samples were also used later for layer removal analysis of residual stresses for comparison with the synchrotron residual stress data. The first attempts at layer removal were done on the PANalytical X'pert Pro system, but were not very successful due to problems with the electro-polishing technique. The specimen material was very resistant to layer removal, and various electrolytes were tried, finally a combination of orthophosphoric acid, ethanol and perchloric acid was used. This electrolyte removed material, but it was too

aggressive and also removed the carbides around the grain boundaries. This resulted in the surface of the samples being stress relieved and the residual stress data was meaningless. A light mechanical polish removed the stress relieved layer and the compressive residual stress was again apparent.

A later set of measurements was recorded in the Eskom laboratory using a Proto iXRD machine and a customised electro-polishing unit from Proto Manufacturing, Canada. This set of measurements was successful with the layer removal process working properly and the results correlating well with the synchrotron data.

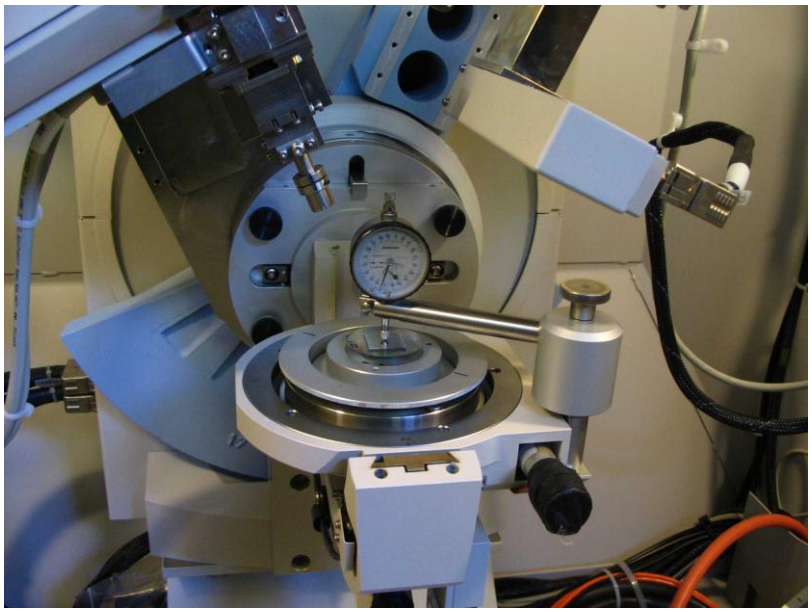

Figure 52: Sample mounted in Panalytical XRD machine

4.5 Synchrotron measurements

An application for beam time at the European Synchrotron Radiation Facility (ESRF) in Grenoble was submitted through Plymouth University. This peer reviewed application was successful and five days were allocated on beam line ID31 in June 2007.

Beam line ID31 has a mono-chromated beam with energy levels in the 5 to 60keV range. This allows for transmission diffraction experiments on steel samples of approximately 7mm thickness. The diffracted beam angle is measured by a precision detector as shown in Figure 44 and illustrated schematically in Figure 53.

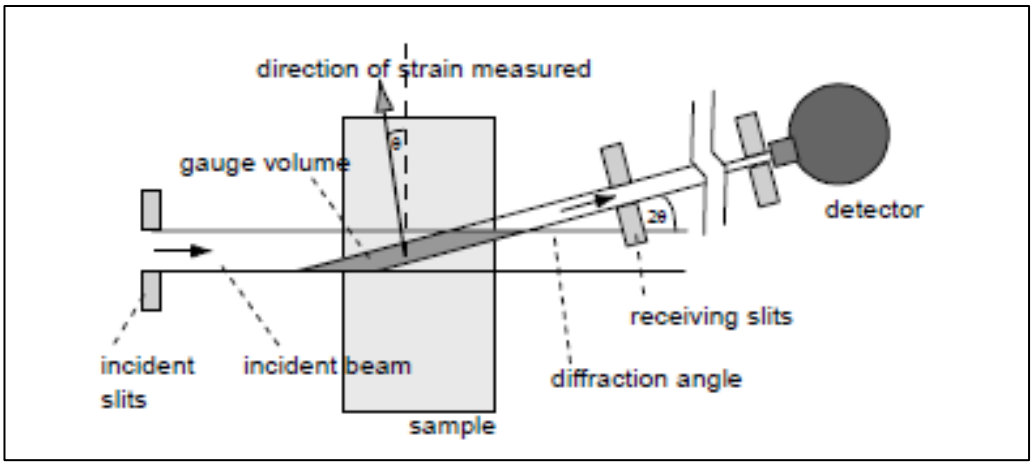

Figure 53: Schematic of X-ray beam and detector

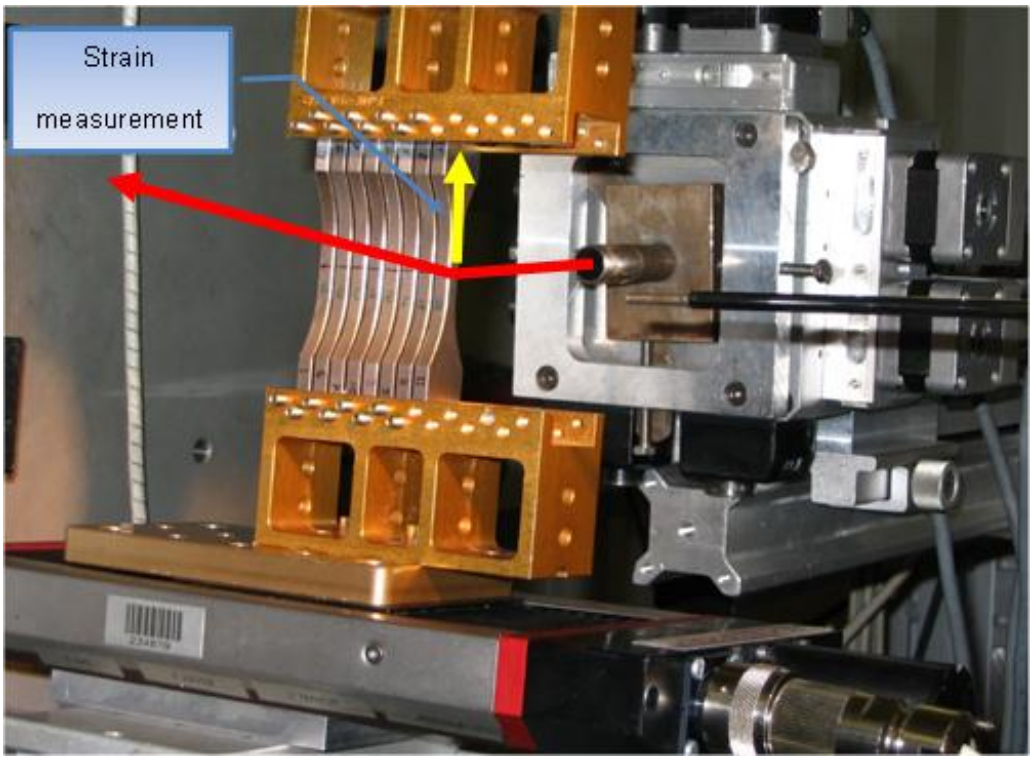

Figure 54: Beam line ID31 sample arrangement for longitudinal scans, showing strain measurement direction. Slit sizes of 50µm and 100µm were used

The sample arrangements are shown in Figure 55, Figure 56 and Figure 56.

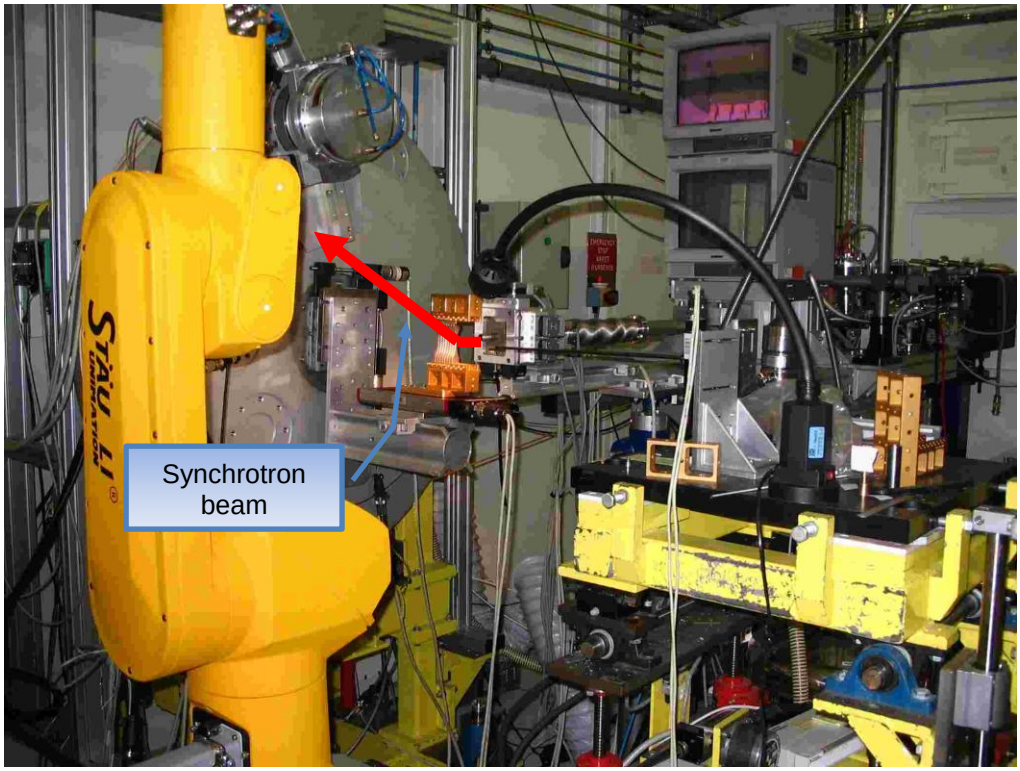

Figure 55: Beam line ID31 general arrangement of instrument

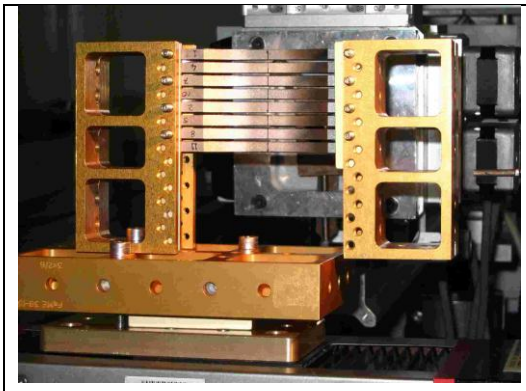

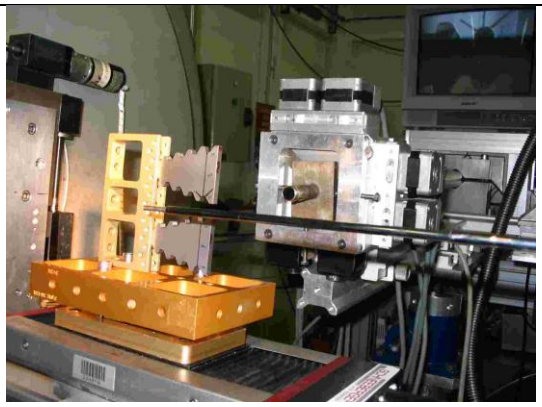

Through-thickness scan	Fir tree scan

Figure 56: Beam line ID31 sample arrangement for through-thickness and fir tree scans

The samples were mounted in brackets so that the residual stresses could be measured sequentially in each desired direction. The time required to acquire a peak is very quick at the ESRF, typically less than two minutes for this

experiment and mounting several samples together helps to optimise use of the beam time.

The movement stage where the samples were mounted allowed for very precise location of the samples. The scans were programmed so that the beam started outside the specimen surface on one side of the sample and the specimen was then moved through the beam. Ten increments of 20µm were followed by six steps of 50µm and then four steps of 1mm. The specimen was then moved past the beam and gradually brought back into it using the 20µm and 50µm steps. This resulted in thirty six scans per sample for one direction of measurement. When the longitudinal scans were complete, with the samples having moved in a horizontal direction, the bracket holder was rotated through 90° as shown in Figure 56 and the specimens were moved in a vertical direction through the beam for the through-thickness measurement.

The test matrix for experiment MA326 is described below, and summarised in Table 6;

- Two samples of each shot peened condition (75%, 100%, 150% and 200%) were measured in the as-peened condition, in both longitudinal and through-thickness directions.
- One sample from each condition, i.e. four samples in total, was then loaded in a single cycle to a stress of 868MPa (0.2% proof stress) and the residual stress profiles were then re-measured.
- These samples were then loaded in a single cycle to a stress of 910MPa (0.5% proof stress) and the residual stress profiles re-measured.

- The other four samples, one from each condition, were loaded in a single cycle to a stress of 600MPa (limit of proportionality) and the residual stress profiles were then re-measured.
- These samples were then loaded to a mean stress of 868MPa and a dynamic stress amplitude of ±20MPa was applied for 10,000 cycles. The residual stress profiles re-measured.
- In each test the strain was measured in the longitudinal and through-thickness directions.

Experiment MA326						
Sample	Coverage	Measurements recorded after load condition				
1	75%	As-peened	868MPa	910MPa		
2	75%	As-peened			600MPa	868MPa±20MPa 10,000 cycles
3	75%	Used as test piece in Instron, no diffraction measurements				
4	100%	As-peened	868MPa	910MPa		
5	100%	As-peened			600MPa	868MPa±20MPa 10,000 cycles
6	100%	Not tested				
7	150%	As-peened	868MPa	910MPa		
8	150%	As-peened			600MPa	868MPa±20MPa 10,000 cycles
9	150%	Not tested				
10	200%	As-peened	868MPa	910MPa		
11	200%	As-peened			600MPa	868MPa±20MPa 10,000 cycles
12	200%	Not tested				

Table 6: Summary of tests conducted during experiment MA326

The fatigue tests in experiment MA326 were performed at a mean stress that was at the 0.2% yield point; with a maximum stress 20MPa above this (888MPa). Due to the flat sample configuration this stress was applied uniformly across the section of the specimen, resulting in a rapid loss of residual stress as the material yielded. The data from this test thus had limited application in assessing the reduction in residual stress from fatigue cycles.

A further opportunity was sought to obtain data for residual stress after the application of fatigue cycling at lower mean stress values. A subsequent opportunity arose whereby two days of beam time on beam line ID15A, allocated to experiment ME1165, could be utilised for these measurements Another set of data was therefore recorded on Sample 6 during experiment ME1165 on beam line ID15A. A summary of the measurement matrix for ME1165 is listed in Table 7.

Experiment ME1165		
Sample	Coverage	**Fatigue loading**
6	100%	First scan, **As peened**
		Second scan **, First load 15.902kN (623MPa)**
		Third scan **,Second load - 10 cycles 15,295kN with dynamic of 0,51 0-pk (600 ±20MPa)**
		Fourth scan, **100 cycles (600 ±20MPa)**
		Fifth scan - **1000 cycles (600 ±20MPa)**
		Sixth scan **10000 cycles (600 ±20MPa)**
		Seventh scan **100000 cycles (600 ±20MPa)**
		Eighth scan, **Load to 22.14 kN (868MPa)**
		Ninth scan, **100 cycles mean 21,63kN ±0,51kN (848 ±20MPa)**
		Tenth scan, **10000 cycles mean 21,63kN ±0,51kN (848 ±20MPa)**
		Eleventh scan, 45° direction,

Table 7: Summary of tests conducted during experiment ME1165

4.6 Finite element modelling

A finite element modelling technique was developed to simulate the residual stress profiles on the fir tree after shot peening, and to correlate these results with experimental values. The model was further used to determine the effect of centrifugal loading on residual stress profiles.

Having considered the various finite element modelling methodologies listed in 2.3.3, and considering the superposition requirement for the centrifugal loading, it was decided to use a quench loading technique in the model in order to generate the residual stress profile. The model was created in ANSYS ver12. Models for both the flat samples and the fir tree were constructed and analysed. The modelling process was initially applied to the flat sample so that the results could be correlated with the synchrotron data. The quenching simulation of shot peened residual stresses was then applied to the fir tree model.

The models were constructed in ANSYS as 2D plane-strain models. Elastic-perfectly plastic material was assumed. The models were analysed using two different element types both of which had eight nodes. The PLANE77 element, shown in Figure 57, is a higher order 2D 8-node or 6-node thermal solid element. The element has one degree of freedom, temperature at each node. The element is applicable to a 2D steady state or transient thermal analysis. If the model containing this element is to be analysed structurally, then it should be replaced by and equivalent structural element PLANE183.

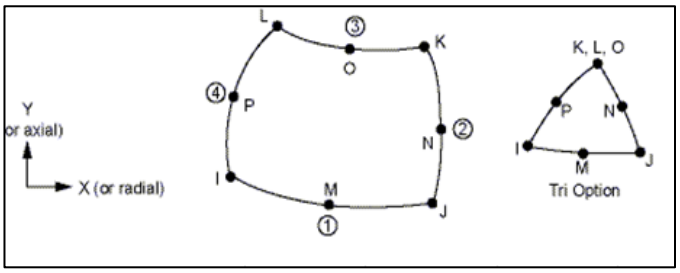

Figure 57: ANSYS PLANE77 element

The PLANE183 element, shown in Figure 58, is a higher order 2D 8-node or 6-node structural solid element. The element has a quadratic displacement behaviour and is well suited to modelling irregular meshes. The element is defined by 8 nodes or 6 nodes having two degrees of freedom at each node. The element may be used as a plane stress or plane strain analysis and has plasticity, hyper plasticity and large strain capabilities. The similarity to the PLANE77 element is clear from Figure 57 and Figure 58.

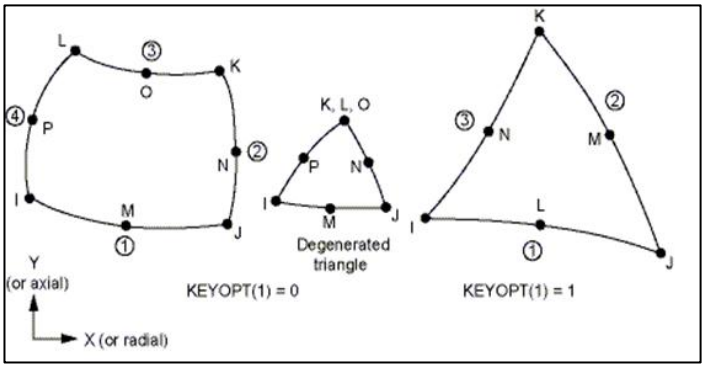

Figure 58: ANSYS PLANE183 element

A transient thermal analysis was run, using ANSYS Plane77 elements, that generated the temperature profile for quenching. The model was then changed to ANSYS Plane183 elements for the structural analysis and the temperature profile applied, which resulted in the generation of residual compressive stresses. The mesh for the fir tree model is shown in Figure 59.

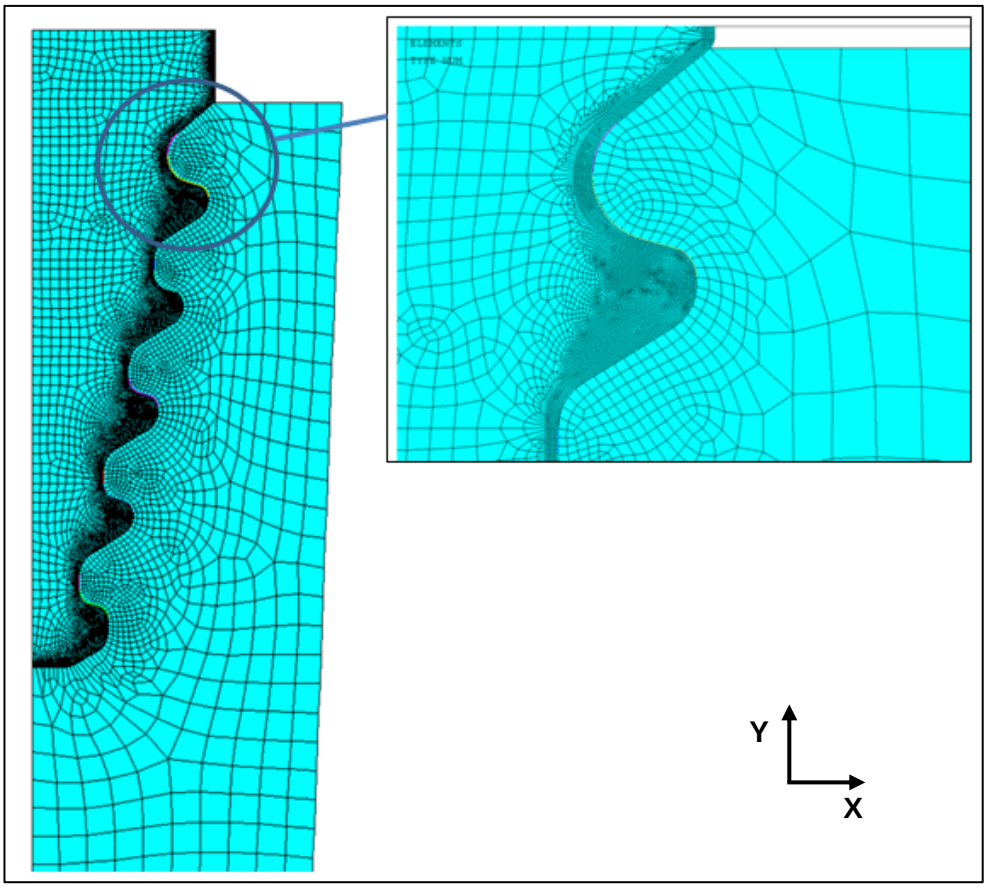

Figure 59: Mesh of turbine blade fir tree root. The inset shows the detail around the top serration

The material properties used in the model are shown in Table 8 below;

PROPERTY	VALUE	SOURCE
Density:	7700kg/m^3	DIN1.4939 [**2**]
Specific heat:	460J/kgK	DIN1.4939 [**2**]
Elastic modulus:	204GPa	Tensile tests on blade samples, see Table 13
Thermal coefficient of expansion	1.16E-5	Assumed after iterative process
Thermal conductivity:	0.1 W/m$^{2\circ}$C	Assumed after iterative process
Yield strength:	868MPa	Tensile tests on blade samples, see Table 13

Table 8: Material properties used in finite element model

In order to generate the residual stress profile a quench loading simulation process was applied that would result in a thin plasticised layer on the surface of the model of approximately 100µm: The constraint of the elastic region below the plasticised layer generated the compressive residual stress profile.

The modelling process was in two parts, the first being the thermal transient analysis and the second was the structural analysis. The object of the modelling was purely to generate the residual stress profile in the structural model and so no account was taken of material microstructure or of surface roughness effects.

The process steps are listed in Table 9 below. The reported residual stress profiles from the model were obtained through an iterative process and correlated with the measured residual stress profiles on the flat samples from the synchrotron data.

The quench loading process was then applied to the fir tree model. For the fir tree model, the steady state analysis listed in Steps 7 to 12 in Table 9 was applied after the residual stress simulation. Models with no shot peening were also analysed for centrifugal loading in the steady state analysis, so that the results could be compared the shot peened models.

STEP	PROCESS
Steps 1-3 were run as a transient thermal analysis to obtain a temperature distribution from the surface of the model	
1	Apply uniform temperature on all the elements of 500ºC
2	Apply convection to the surface elements with a coefficient=110000W/m^2°C and bulk temperature of -1300 ºC for a period of 0.4s
3	Apply convection to surfaces with coefficient =3500W/m^2°C and bulk temp 0ºC for a period of 0.1s
The following steps were run as steady state structural analysis	
4	Apply temperature distribution as calculated in Step 3. This results in tensile yielding on surface
5	Apply uniform temperature of 500ºC to return to the original state in Step 1. This results in a compressive surface residual stress
After generating the residual stress profile, apply centrifugal loads to the fir tree model and report superimposed residual stress profiles	
7	3000 rpm
8	0rpm
9	3300rpm
10	0rpm
11	3600rpm
12	0rpm

Table 9: Finite element modelling process

CHAPTER 5 RESULTS

5.1 Initial laboratory XRD results and roughness measurements

The results from the laboratory XRD measurements conducted at Pretoria University, using the PANalytical X'pert Pro instrument, are shown in Table 10 and Table 11 below. Measurements were recorded in both longitudinal and transverse directions on the shot peened surface in order to check that the equi-biaxial assumption was correct. The final stress was calculated from the two measurements.

SAMPLE NUMBER	SHOT PEENING CONDITION	STRESS [MPa]	ERROR [MPa]	PERCENTAGE DIFFERENCE BETWEEN LONGITUDINAL AND TRANSVERSE MEASUMENT [%]
1	75%	-568.5	19.9	11.3
2	75%	-549.6	18.8	1.7
3	75%	-576.5	18.4	-15.5
4	100%	-588.9	13.5	6.3
5	100%	-572.8	12.8	4.2
6	100%	-596.0	9.3	-0.1
7	150%	-552.6	11.7	-2.5
8	150%	-555.9	14.4	3.3
9	150%	-550.1	11.1	3.8
10	200%	-544.0	13.7	-1.6
11	200%	-576.0	14.1	1.3
12	200%	-564.3	14.9	-3.9

Table 10: XRD results after shot peening

Condition	75%	100%	150%	200%
Mean	-564.9	-585.9	-552.9	-561.4
Standard Error	8.0	6.9	1.7	9.3
Median	-568.5	-588.9	-552.6	-564.3
Standard Deviation	13.8	11.9	2.9	16.2
Range	26.9	23.2	5.8	32.0
Minimum	-576.5	-596.0	-555.9	-576.0
Maximum	-549.6	-572.8	-550.1	-544.0

Table 11: Statistical summary of Stress data from laboratory XRD results

The data showed that there was consistency between samples with the same coverage condition. The maximum standard deviation of 16.9MPa was recorded for the three samples in a 200% coverage condition, which is within the measurement error of one specimen as shown by the typical $sin^2\psi$ plot in Figure 60 where the error is ±36.4MPa. The difference between the longitudinal and transverse measurements showed that the equi-biaxial assumption was correct. Thus the samples were acceptable for the synchrotron experiment.

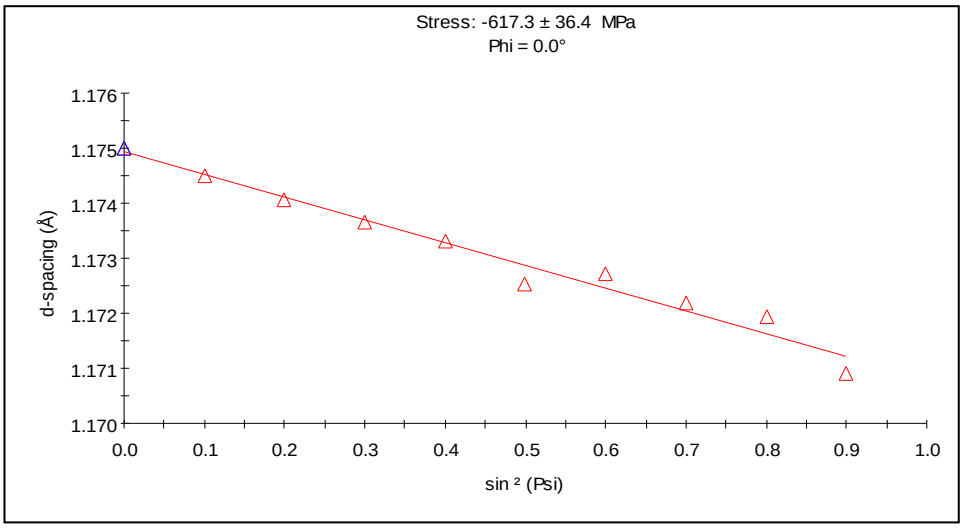

Figure 60: Sample 10 XRD data

The surface roughness after shot peening was estimated by examining cross sections of the samples under an electron microscope and calculating the average peak values Rp according to the JIS B 0031 standard. The results are shown in Table 12 below. There is a marked increase in roughness as the shot peening coverage increases. If the 100% coverage condition is taken as the datum then the average peak-peak roughness increases by 8.8% when the coverage increases from 100% to 200%, whereas the roughness is 17.6% lower at 75% coverage. As shown later in Figure 70, there is very little change in the residual stress profiles over all the coverage conditions. The increased surface roughness is however disadvantageous for ease of assembly of the turbine blades onto the shaft.

SAMPLE	CONDITION	Peak-Peak [µm]	Average Peak-Peak [µm]
Sample 1	75%	16.09	16.60
Sample 2		17.30	
Sample 3		16.41	
Sample 4	100%	18.26	20.15
Sample 5		23.58	
Sample 6		18.60	
Sample 7	150%	20.29	21.03
Sample 8		19.76	
Sample 9		23.04	
Sample 10	200%	23.44	21.93
Sample 11		18.41	
Sample 12		23.93	

Table 12: Surface Roughness Measurements

5.2 Treatment of Errors

No measurements are exact and it is necessary to determine the level of uncertainty of the experimental work by considering potential sources of error. It is important to observe the experimental work closely to identify unexpected errors during the experiment.

In the case of the synchrotron measurements it was decided to adopt the system of maximum error analysis. There were two main sources of error in the experiments; peak position of the diffracted beam and material properties of the steel samples.

The strain calculation was based on the variation in 2θ from which the lattice spacing d_a was obtained, Equation 1 and Equation 2. The error in this measurement was determined during the peak fitting routine by the LAMP software package, and an error value for the peak position was generated for each measurement position.

The material properties were determined by physically testing three tensile test specimens machined from the same blade as the residual stress test samples. The results are shown in Table 13 below. The elastic modulus E is difficult to determine accurately and this is reflected in the scatter shown in the results for E where a standard deviation of 13.7GPa was obtained.

The maximum error estimation for the stress calculation must take into account the product of two variables as determined by Equation 7 and Equation 8 where the calculated strain is multiplied by the material property constants.,

Consider a function *z=x.y* *(where x represents the strain and y represents the material constants)*

The fractional error in a product is the sum of the fractional errors in *x* and *y*.

$$\delta z = y.\delta x + x.\delta y$$

Equation 9 – Fractional error

Therefore for Equation 7 the fractional stress error for the longitudinal strain measurement $\delta\sigma_l$ is;

$$\delta\sigma_l = \frac{E(1+\nu)}{(1-\nu^2)}\delta\varepsilon_l + \frac{\varepsilon_l(1+\nu)}{(1-\nu^2)}\delta\mathrm{E}$$

Equation 10 – Fractional stress error from longitudinal strain measurement

And for Equation 8 the fractional stress error for the through-thickness strain measurement $\delta\sigma_{lt}$ is;

$$\delta\sigma_{lt} = \frac{-E}{2\nu}\delta\varepsilon_t + \frac{-\varepsilon_t}{2\nu}\delta\mathrm{E}$$

Equation 11 – Fractional stress error from through-thickness strain measurement

Specimen	Area [cm^2]	0.2 % Proof Stress [MPa]	Elastic Modulus [GPa]	UTS [MPa]	%Elongation	%Reduction of Area
No.1	0.19556	868.5	204.2	1046.1	15.6	58.9
No.2	0.19478	875.8	217.9	1056.4	13.2	58.7
N0.3	0.19556	854.1	190.4	1040.5	13.6	58.4
Mean	0.19530	866.1	204.2	1047.7	14.1	58.6
Median	0.19556	868.5	204.2	1046.1	13.6	58.7
Coefficient of variation	0.23148	1.3	6.7	0.8	9.1	0.4
Range	0.00078	21.7	27.5	16.0	2.4	0.5
Standard Deviation	0.00045	11.0	13.7	8.1	1.3	0.3

Table 13: Results of tensile tests

The error bars are shown for the strain and stress calculations on Sample 11 in Figure 61 and Figure 62 below. It is clear that the error in the strain measurement is very small, with average error of 19µm/m for this specimen. The error in the stress calculation, from Equation 7, varies according to the measured strain amplitude due to the effect of the material constants and has a maximum of 60MPa when the residual stress is -780MPa, i.e. 7.7% which is acceptable in residual stress terms.

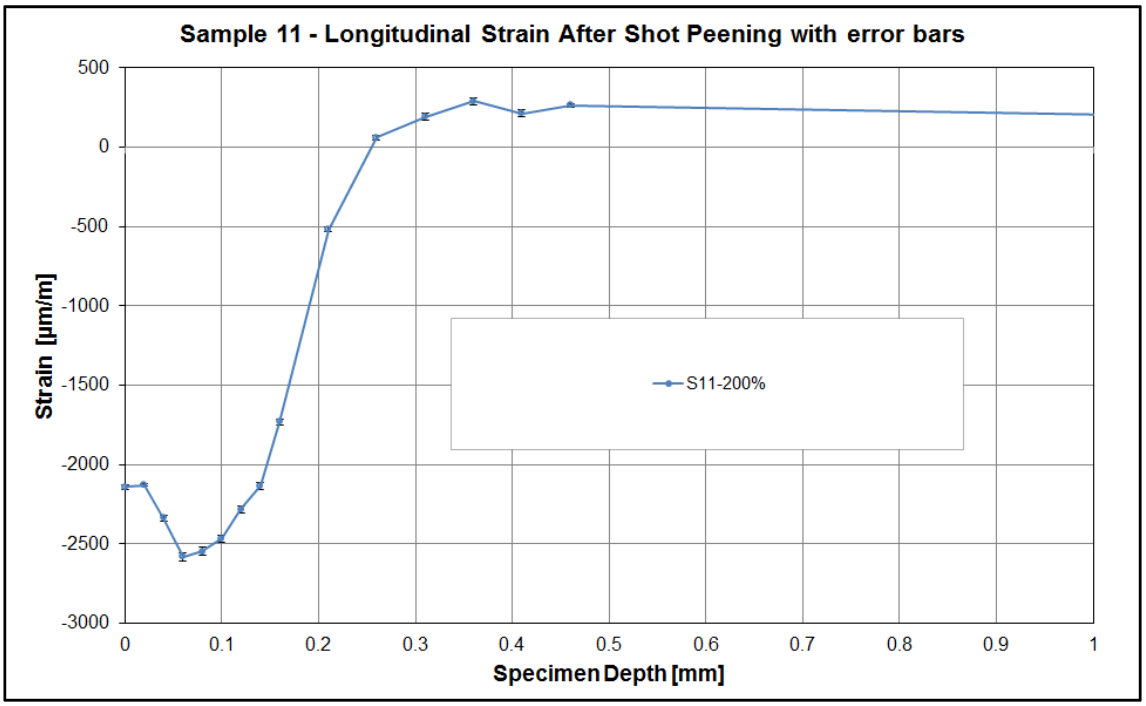

Figure 61: Measured longitudinal strain from Sample 11 showing the residual strain with error bars.

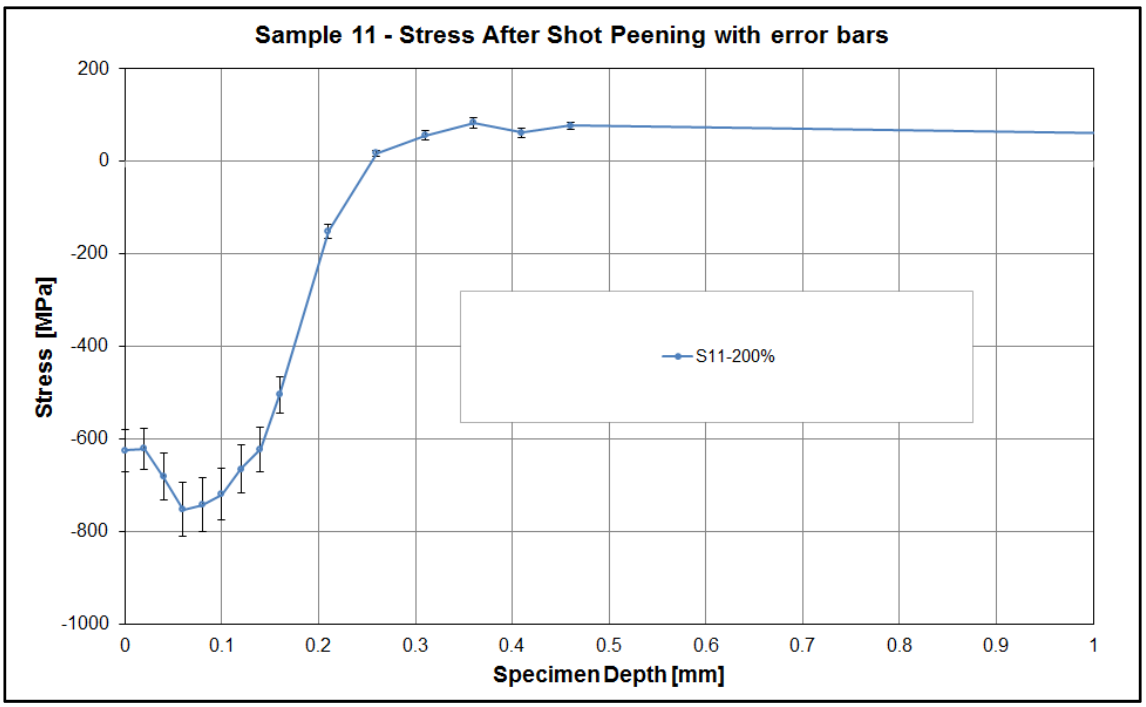

Figure 62: Calculated stress from Sample 11 showing error bars.

5.3 Synchrotron data from experiment MA326

The first synchrotron tests were conducted at the ESRF on beam line ID31 in June 2007. The residual stress samples were orientated so that the strain could be measured first in the longitudinal direction and then in the through-thickness direction. The samples are shown in Figure 54, Figure 55 and Figure 56 in section 4.5 and the measurement directions are shown in Figure 63. It was not possible to measure strains in the third orthogonal direction due to the length of the samples. The stresses were assumed to be equi-biaxial, as was the case for the XRD measurements. This meant that the longitudinal stress could be calculated from either the longitudinal or the through-thickness strain [**44**]. The wavelength of the synchrotron beam during the experiment was 0.2072Å and reflection off the {211} diffraction plane was measured.

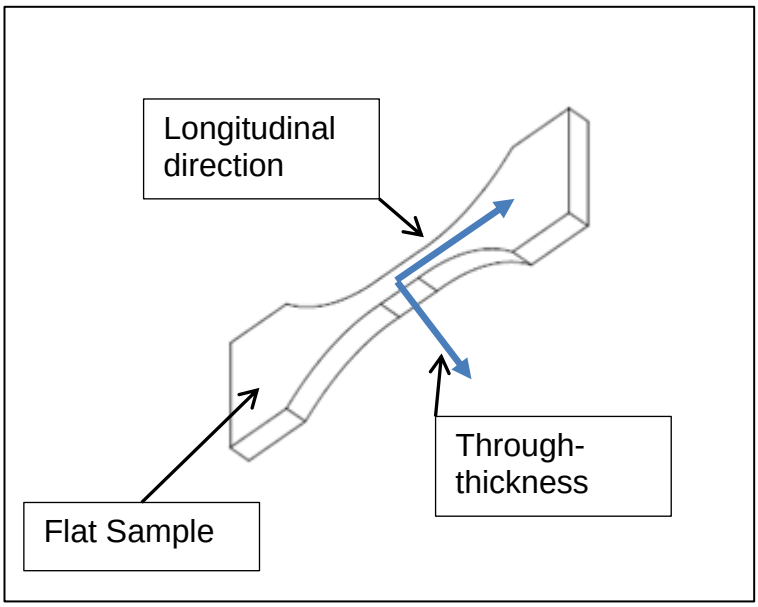

Figure 63: Schematic of flat sample showing strain measurement directions

The experimental process was given in section 4.5 and summarised in Table 6, but is repeated below for clarity;

- The residual stresses were measured in two samples of each shot peened condition (75%, 100%, 150% and 200%) in the as-peened condition, in both longitudinal and through-thickness directions.
- One sample from each condition, i.e. four samples in total, was then given a single load cycle to a stress of 868MPa (0.2% proof stress) and the residual stress profiles were then re-measured.
- These samples were then given a second single load cycle to a stress of 910MPa (0.5% proof stress) and the residual stress profiles re-measured.
- The other four samples, one from each condition, were given a single load cycle to 600MPa (limit of proportionality) and the residual stress profiles were then re-measured.
- These samples were then loaded to a mean stress of 868MPa and a stress amplitude of ±20MPa was applied for 10,000 cycles. The residual stress profiles were re-measured.
- In each test the strain profile was measured in the longitudinal and through-thickness directions.

In each case the ID31 instrument was programmed to take scans from the initial point at the surface commencing at 20µm intervals for ten steps, then 50µm intervals for six steps and then 1mm steps across the specimen thickness. The beam shape was controlled by using 50µm and 100µm slits with the 50µm dimension orientated in the translation direction of the sample. In the case of the longitudinal strain measurement, the beam passed through the complete

thickness of the specimen as soon as the specimen encountered the beam and the beam was fully immersed after 50µm. In the case of through-thickness strain measurement, the beam entered with the tip of the gauge volume first and was only completely immersed after approximately 0.27mm. This effect is illustrated in Figure 64 below.

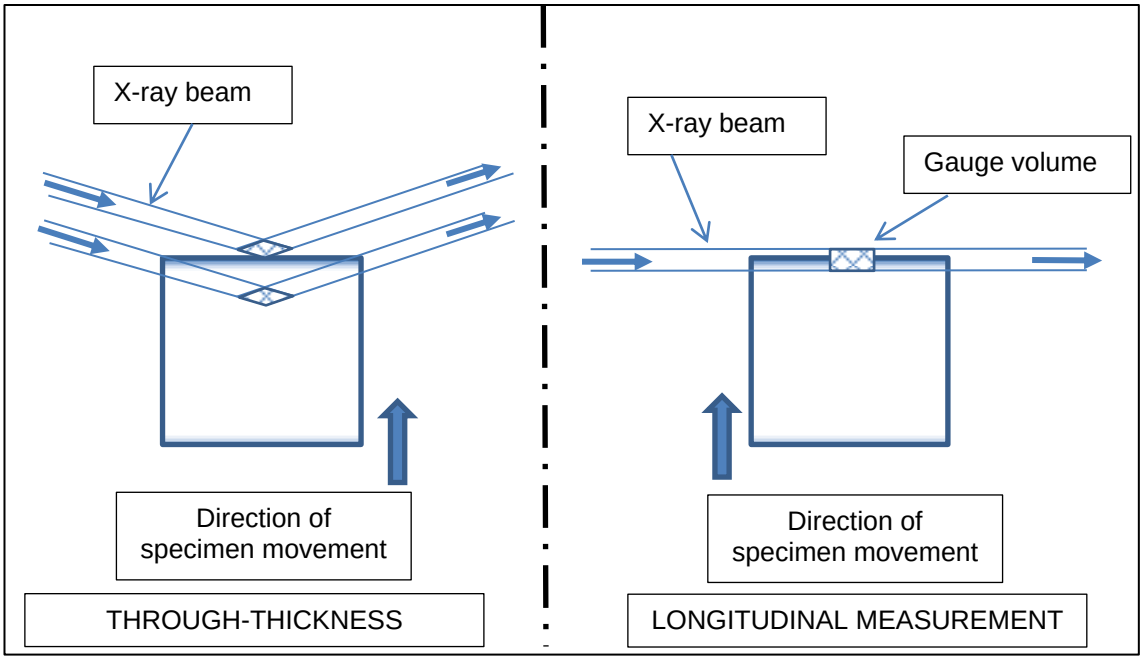

Figure 64: Schematic of Synchrotron X-ray beam entering specimen for Through-thickness and Longitudinal strain measurement directions. In the case of the Through-thickness measurement the path length of the beam increases as the specimen moves until the gauge volume is approximately 0.27mm below the surface. The path length of the Longitudinal measurement is constant for all the positions

The raw data from ID31 was reduced to a lattice spacing value d_a for each scan using the LAMP software supplied by the ESRF and a customised Python routine including *scipy* and *kinfit* for the curve fitting procedures. The reason that the Python routine had to be used was that the ID31 instrument partially malfunctioned during the experiment resulting in faulty positional values at the start of some of the tests, which LAMP could not read. This partial malfunction meant that the data could not be viewed effectively during the experiment and

some of the problems with the through-thickness measurement only became apparent during post-processing of the data.

The strain was then calculated from the peak position at each point and the beam wavelength using Equation 1 and Equation 2. As the synchrotron X-ray beam could penetrate fully through the specimen, it was possible to get a full residual strain profile and therefore calculate a stress balance across the specimen section in order to obtain a d_0 value. The average d_0 obtained by this method was 1.185558Å. The residual strain profiles for the longitudinal measurement direction are shown in Figure 65 for Sample 11 and in Figure 68 for all eight samples. The material properties listed in Table 13 were applied and the inferred stress calculations based on an equi-biaxial stress state were calculated using Equation 7 from the longitudinal strain measurement and Equation 8 from the through-thickness strain measurement.

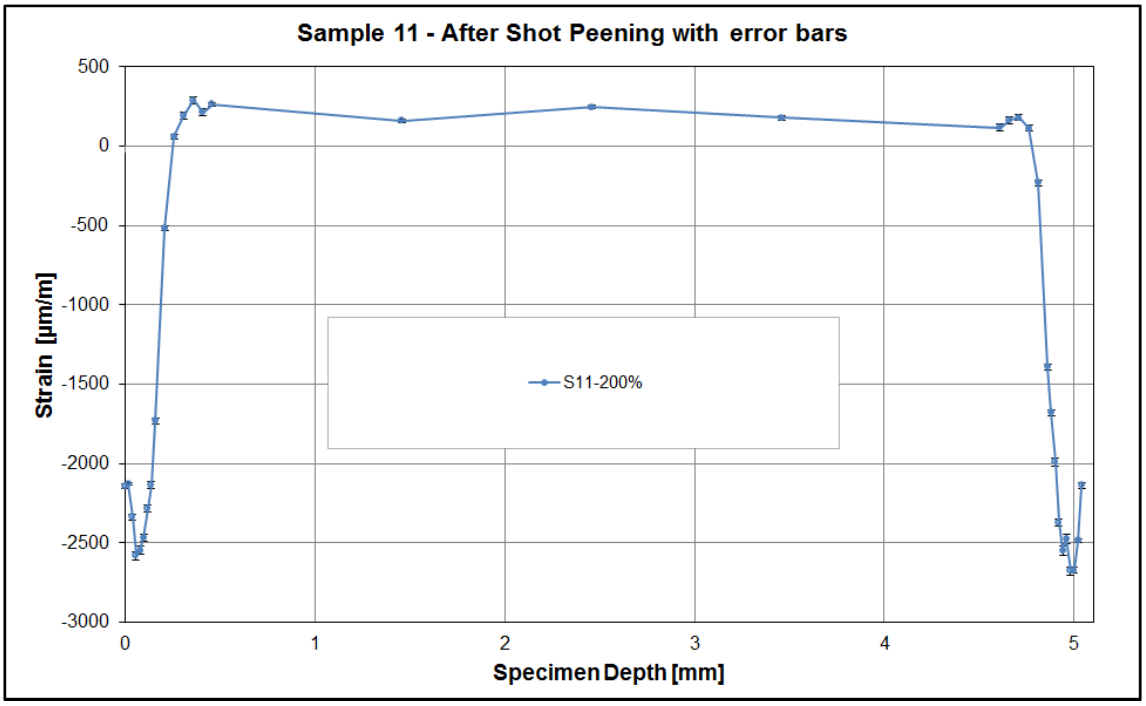

Figure 65: Complete longitudinal strain profile across the thickness of Sample 11

Figure 65 shows the measured residual strain, from the longitudinal strain vector, across the full thickness of Sample 11 (200% coverage). The shape of the curve follows the expected residual strain profile from shot peening, with the maximum compressive strain occurring approximately 60µm below the surface. The quality of the data was very good with an average error of 19µm/m reported from the peak fitting routine, the error bars are shown on the graph.

The through-thickness strain measurement was not as successful as the longitudinal measurement due to the entry path of the synchrotron X-ray beam into the specimens as illustrated in Figure 64. This resulted in a convolved data set as discussed by Xiong et al [**45**], who developed a MATLAB routine for separating out the underlying function in a data set, and validated the technique specifically for measured data from a synchrotron experiment. As stated in the paper [**45**]; *"The MATLAB code for our statistical deconvolution algorithm together with the mathematical formalism is available from our website (http://www.sdc.manchester.ac.uk/soft/)".* The MATLAB routine was used to correct the through-thickness scan data as illustrated in Figure 66 for the strain data and Figure 67 for the stress calculation. This correction was only done for the top side of the sample, where the beam entered first, as the quality of data from the bottom side was significantly worse than the top. It can be seen that the MATLAB routine is most effective in correcting the data in the first 180µm, when the spatial sampling was highest with steps of 20µm, after which the correlation between the longitudinal and through-thickness measurements falls away. This is consistent with the findings of Xiong et al [**45**], that the routine works best with higher spatial sampling.

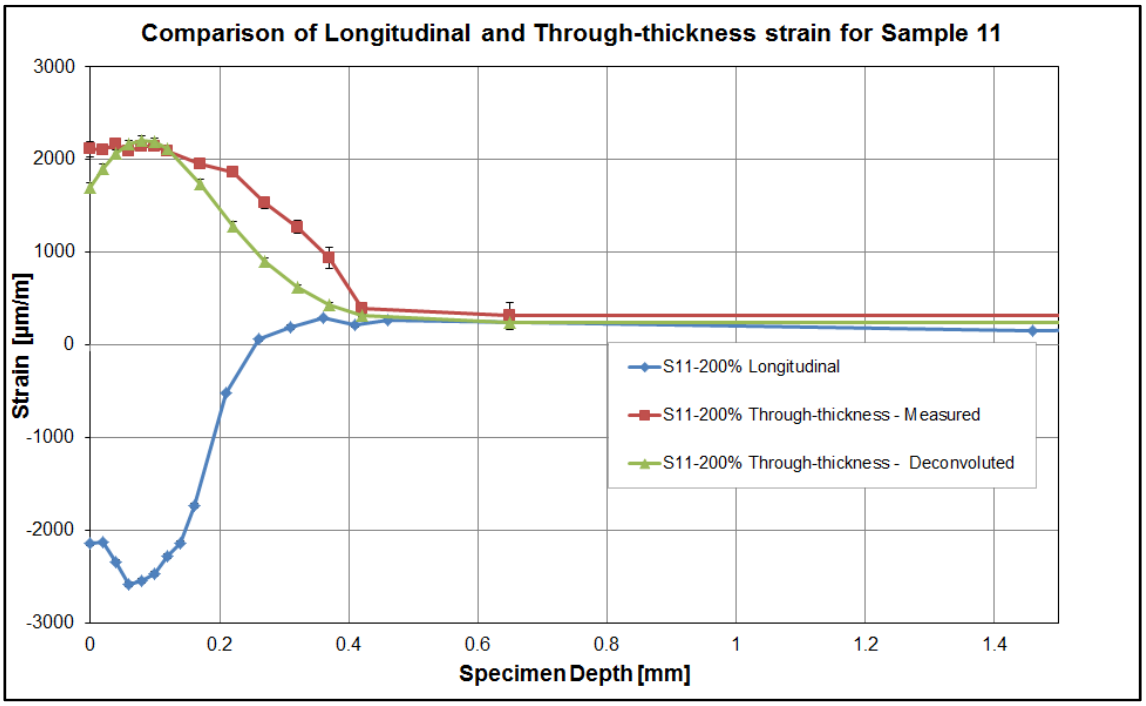

Figure 66: **Illustration of correction for convolution effect in through-thickness strain data. The through-thickness strain is opposite in sign to the longitudinal strain and should be equal in magnitude**

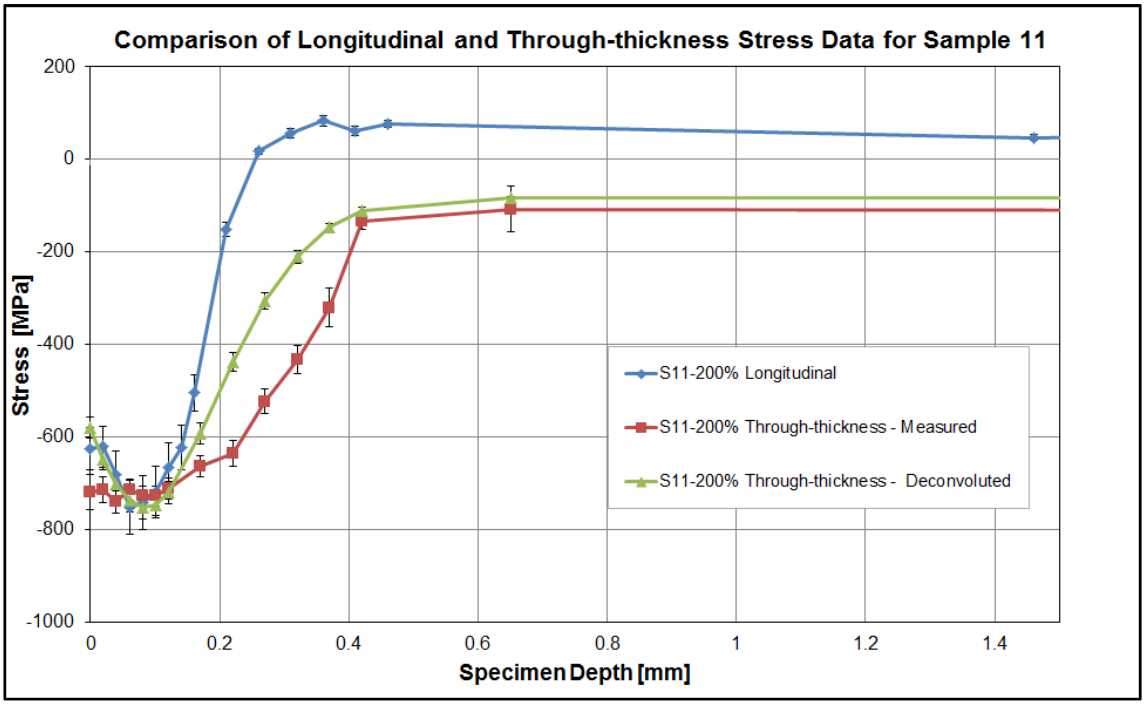

Figure 67: **Illustration of correction for convolution effect in through-thickness stress data. There is good agreement of the residual stress profile between the through-thickness and longitudinal stress calculations over the first 180µm.**

The strain depth profile for the longitudinal direction was confirmed in the tests done in experiment ME1165 and later laboratory XRD measurements using layer removal as shown in Figure 74 on page 102, and in Figure 81 on page 110. The longitudinal strain data from the flat samples was thus used in the further analysis of the residual stress profiles.

The measured residual strain data in the longitudinal direction for all eight samples is shown in Figure 68. The data points for the full strain profile across the 5mm thick sample are shown, and it is clear that there is very good consistency between samples with the same coverage condition, but more importantly, there is also very little difference between the different coverage conditions. The expanded view of the first 0.5mm from the surface highlights this further. The error bars, shown in the expanded view, for the strain data are less than the size of the series markers.

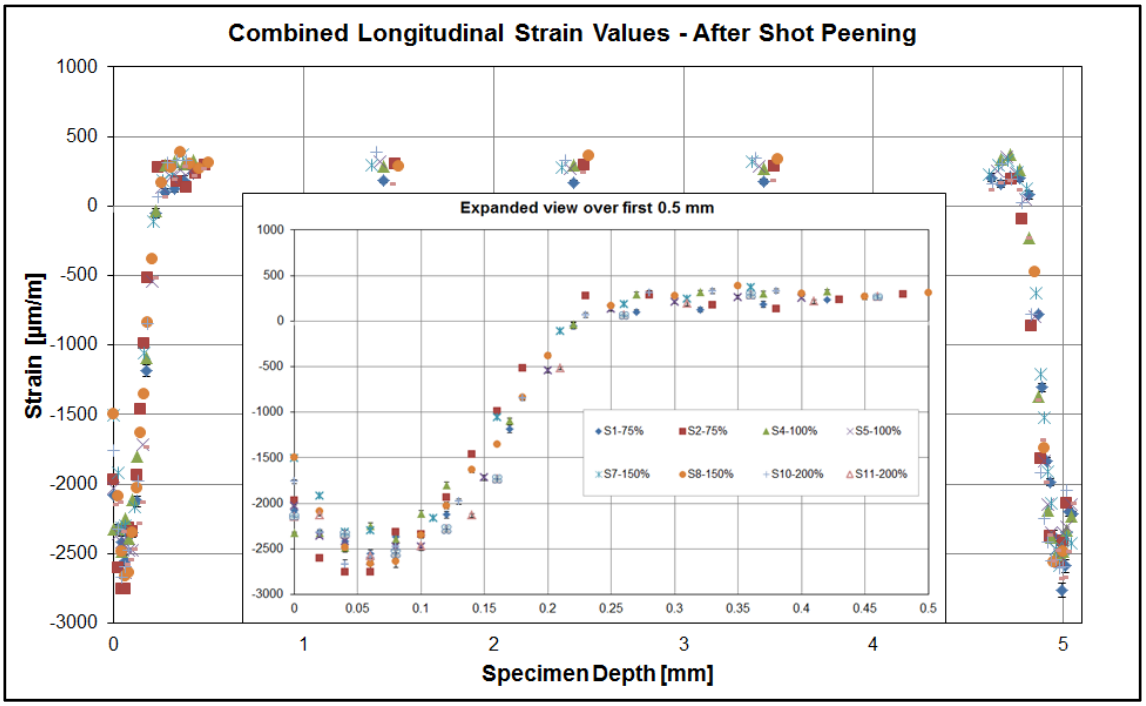

Figure 68: Measured longitudinal strain across eight samples with an expanded insert of the first 0.5mm from the surface

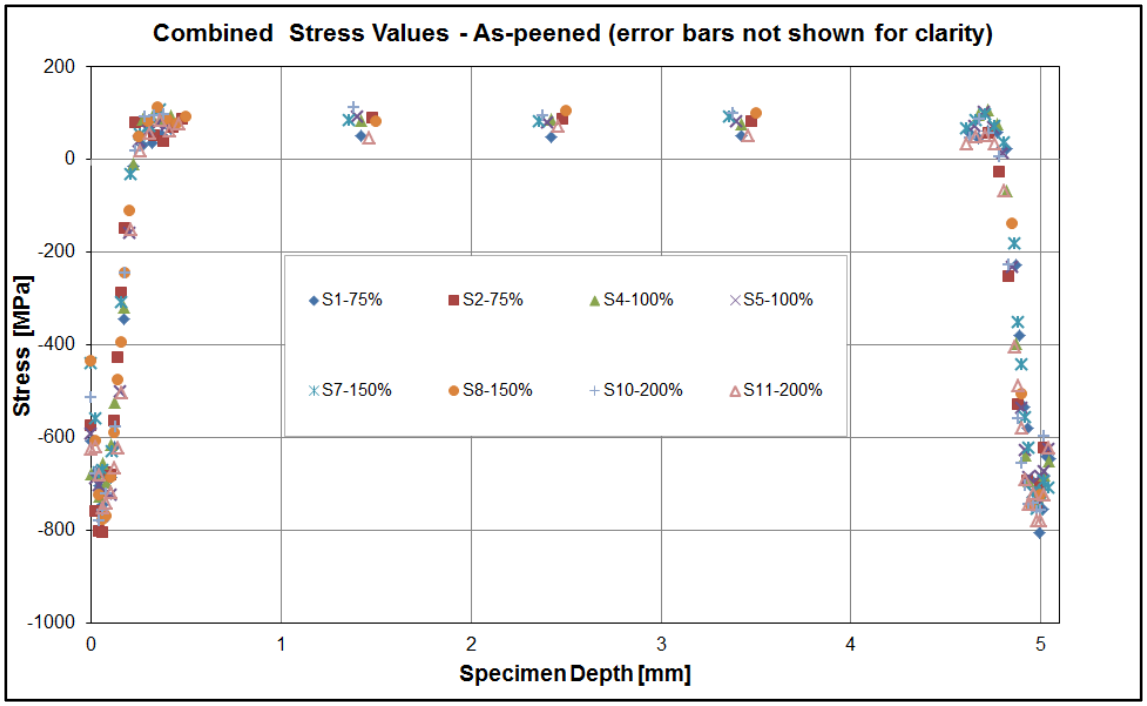

Figure 69: Synchrotron data for the as-peened condition (error bars not shown for clarity)

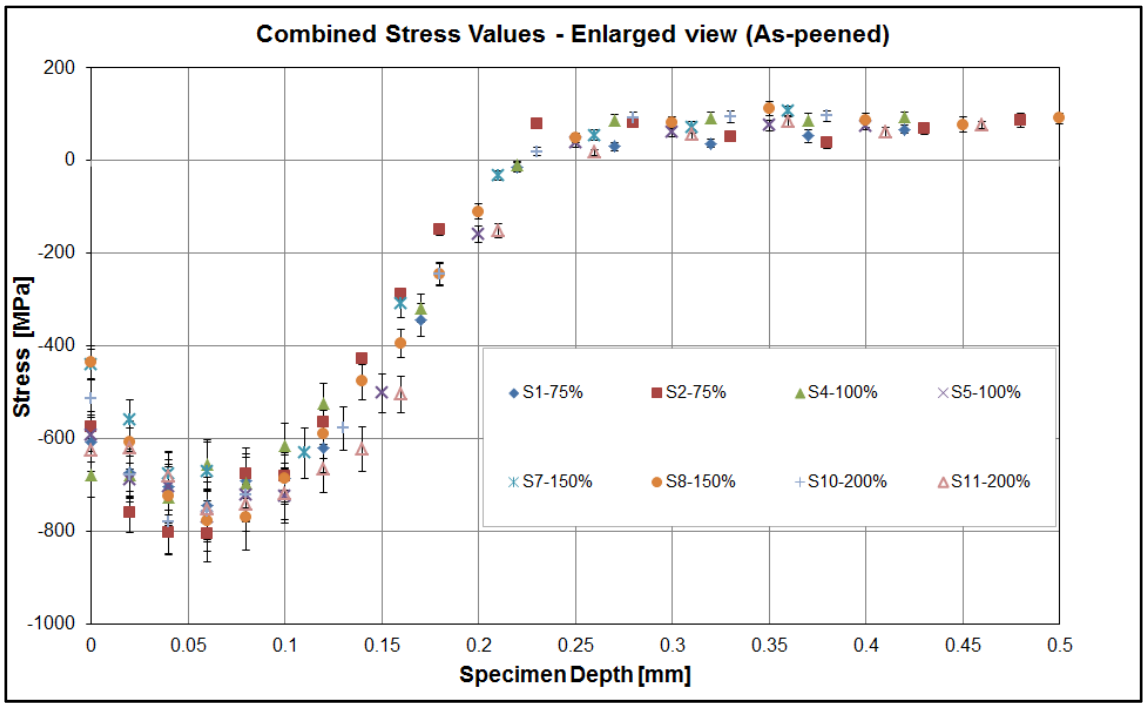

Figure 70: Enlarged section of synchrotron data for the as-peened condition

Figure 69 shows the calculated stress data from the eight samples, two from each coverage condition. Figure 70 shows the data over the first 0.5mm depth into the sample. The stress profile is consistent with those seen in other published data where a compressive stress maximum is observed just below the surface, with the residual stress trend going tensile approximately 0.25mm into the depth of the samples. There was no significant difference observed between the residual stress data for all four different shot-peening conditions. Figure 70 illustrates that the highest compressive stress, of approximately 800MPa, occurred on Sample 2 with 75% coverage. There were some differences in the depth of penetration and, as expected, the greatest depth of penetration was on a sample with 200% coverage.

The as-peened data shown in Figure 69 and Figure 70 for the 12Cr turbine blade steel is in agreement with the work done by Prevéy and Cammett, [**20**], [**21**] which showed that shot peening coverage as low as 20% resulted in an almost fully developed residual stress profile on aircraft quality 4340 (NiCrMo) steel plate.

Once the as-peened residual stress condition had been measured the samples were subjected to further tensile and fatigue loading as listed in Table 6 on page 76. Figure 71 summarises the residual stress data measured after applying these loads. The measurements on Sample 10 after the application of the 0.2% proof stress of 868MPa showed that the residual stress had reduced significantly, which was to be expected as some yielding would occur across the section of the flat sample. The next cycle to 910MPa reduced the residual

stress completely, with a resultant tensile stress of approximately 100MPa being induced on the surface of the specimen. The fatigue loading on Sample 11, of 868MPa ±20MPa for 10,000 cycles, resulted in the stress being relaxed in a similar way to the single stress cycle of 910MPa.

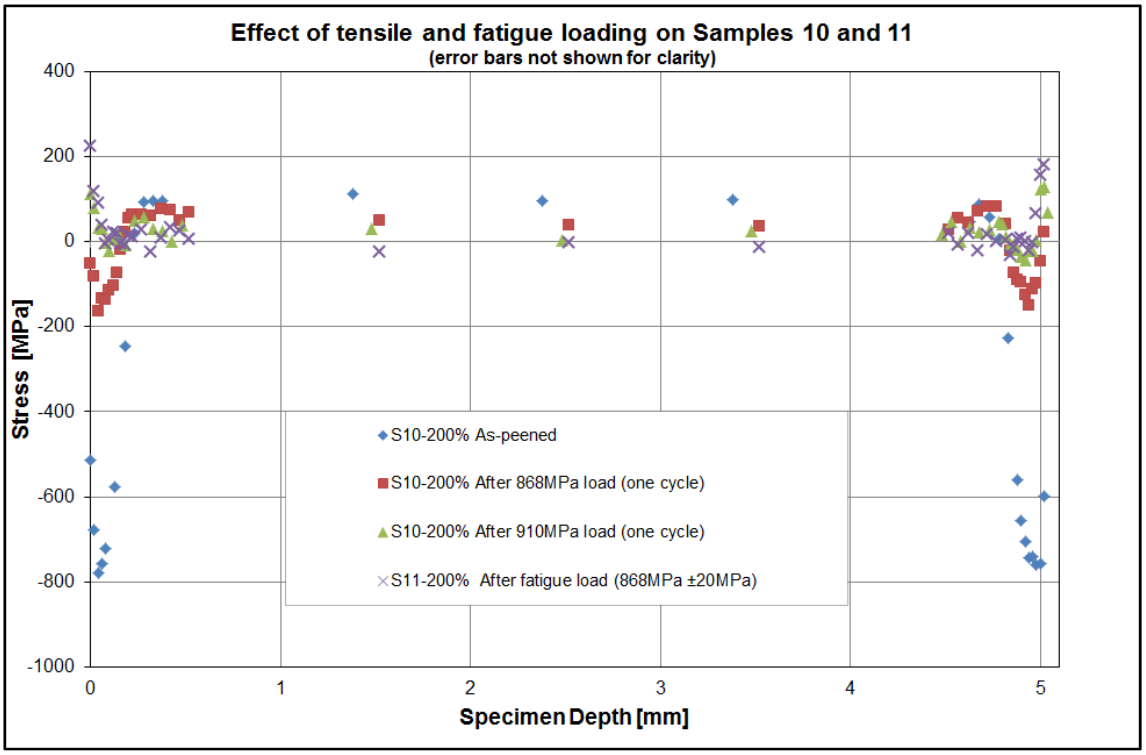

Figure 71: Summary of the effects of tensile and fatigue loading on Samples 10 and 11.

The fir tree samples only had the residual stresses measured in the through-thickness direction as the intention was to try and measure profiles at different positions around the top serration to establish the uniformity of the residual stress field. A similar convolution problem to that of associated with the through-thickness scans on the flat samples, as explained on page 953, was also experienced with these fir tree measurements.

Figure 72 shows the residual stress profile calculated from the measured through-thickness strain for fir tree sample 2, while Figure 73 shows the

calculated residual stress profiles for two fir tree samples together with the deconvoluted profiles obtained from using the MATLAB routine. The data from the flat Sample 11 is also shown for comparison. Stresses in the fir tree specimen were calculated in the through-thickness direction and were found to have magnitudes at the surface comparable to those observed with the flat specimens, with a peak stress value depth similar to those seen in the through-thickness flat specimen data, as shown in Figure 73. The assumption can therefore be made that the longitudinal residual stress profile in the fir tree specimens is similar to that observed in the flat samples.

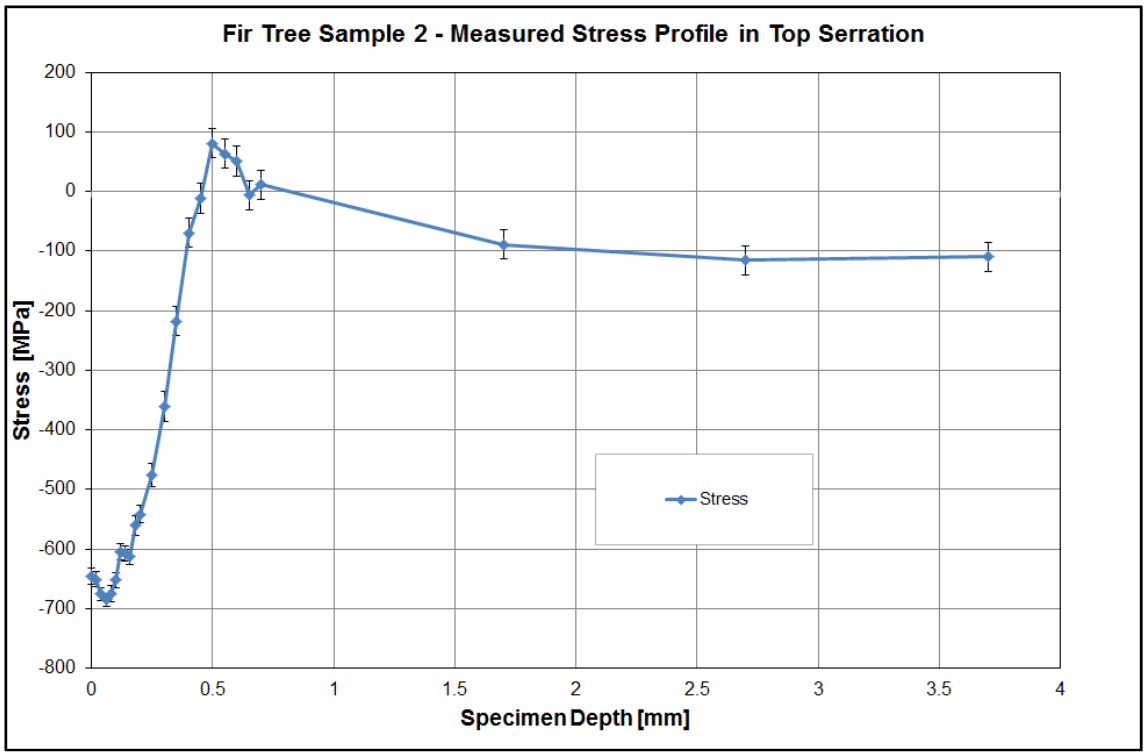

Figure 72: Residual stress in the top serration of the fir-tree (determined from the through-thickness strain tensor)

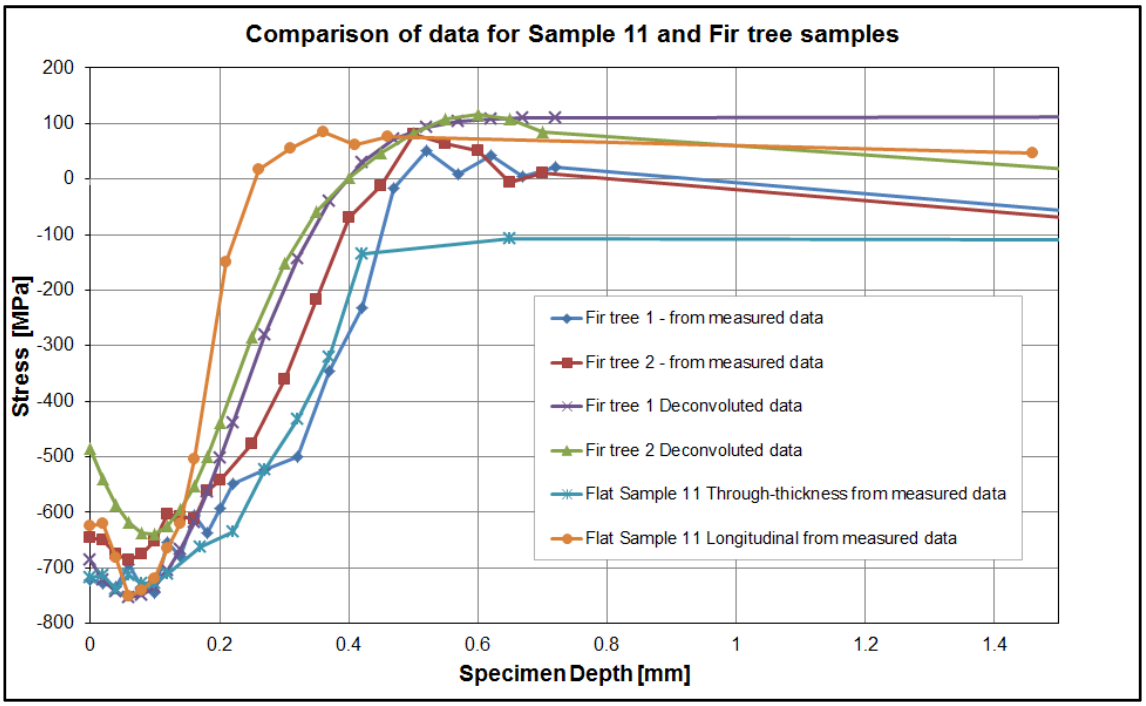

Figure 73: Comparison of measured and de-convoluted stress data (error bars have been removed for clarity)

5.4 Synchrotron data from experiment ME1165

The fatigue tests that were conducted during ESRF experiment MA326 showed that the residual stress profile, on flat samples, reduced significantly under the applied stress, but did not allow for any trending of the rate of reduction in residual stress. A further opportunity was sought to obtain better data for the change in residual stress after the application of fatigue cycling at lower mean stress values. A subsequent opportunity arose in December 2008 whereby two days of beam time on beam line ID15A, allocated to experiment ME1165, could be utilised for these measurements.

The fatigue loading experiment was therefore repeated on beam line ID15A using Sample 6, which had been subjected to a 100% peening coverage, and which had not been used during experiment MA326 on beam line ID31. Two

levels of mean stress were applied, initially 600MPa was used and then later 848MPa was used. The maximum stress was limited to the 0.2% proof stress value of 868MPa, either due to a once off load or from the maximum load in the fatigue cycle. This was based on the experience of the specimen response in experiment MA326 on ID31. The fatigue loading was applied off the beam line using an INSTRON dynamic testing frame rated to 25kN, serial number 2114.

The applied stress amplitude of ±20MPa was based on a conservative estimate of the dynamic forces experienced by a turbine blade during normal operation. The stress matrix shown in Table 14 was applied to Sample 6 to give a structured series of incremental fatigue loadings.

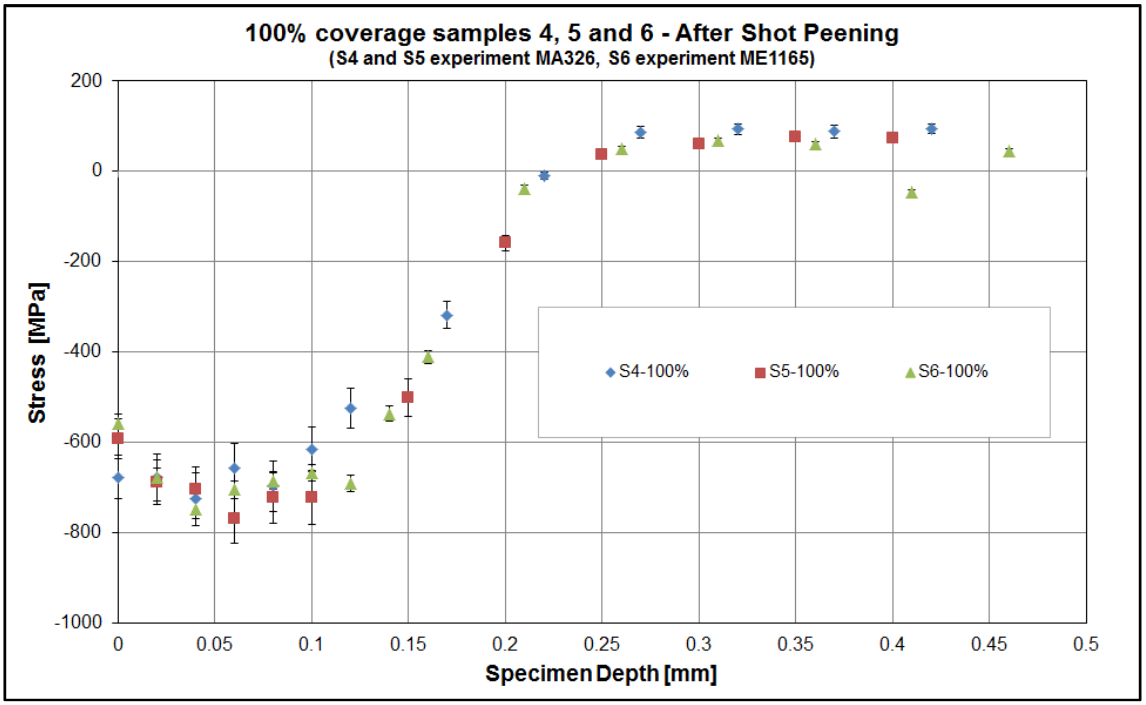

Figure 74: Comparison of as-peened data over the first 0.5mm of depth for the three 100% coverage condition specimens, highlighting the consistency of data between experiments MA326 and ME1165

The as-peened residual strain profile in Sample 6 was measured first and the calculated residual stress results compared to the two other samples with 100%

peening coverage that had been previously analysed in experiment MA326. The results are shown in Figure 74, and there was excellent correlation between the data sets recorded on the two different beam lines giving confidence in the relevance of the subsequent measurements of residual stresses after fatigue cycling. The strain processing on ID15A was done by obtaining a lattice parameter using several of the diffraction peaks in the spectrum, not just the {211} reflection.

STRESS	NUMBER OF CYCLES
620MPa	1 cycle
600 ± 20MPa	10; 100; 1,000; 10,000 and 100,000 cycles R=0.935, f=5Hz
868MPa	1 cycle
848 ± 20MPa	100 and 10000 cycles R=0.953, f=5Hz

Table 14: Load matrix for fatigue testing of Sample 6

The R ratio of 0.935, given in Table 14, represents a realistic loading condition for a number of areas in the fir tree root that are not at the most highly stressed region. The 600MPa stress was hence chosen to obtain a reasonably high R ratio of 0.935, but still have a peak stress below the 0.2% yield value of 868MPa (600MPa was at the limit of proportionality in the tensile tests conducted on the material). The residual stress was not expected to degrade at this applied stress level, but loading a flat hour glass sample in tensile fatigue should be done carefully to avoid inadvertent overload conditions in the tensile testing machine. The applied stress is constant across the specimen section and there is no constraint support as in the case of a notched sample, so any load that results in plastic deformation has a rapid effect on the residual stress.

A summary of the residual stress data after the fatigue cycling for the tests with a mean load of 600MPa is shown in Figure 75 and Figure 76. The results in Figure 75, which has measurement data for the whole cross-section, show that the fatigue loading up to 100,000 cycles had no discernible effect on the residual stress profiles.

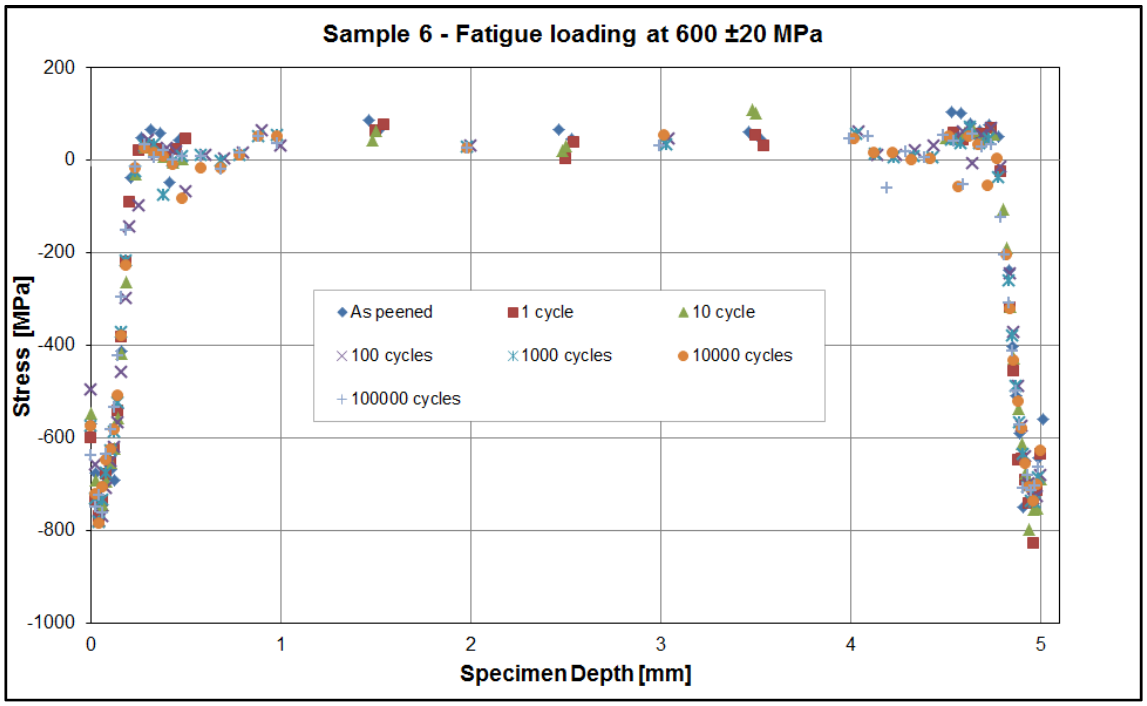

Figure 75: Residual stress profiles for different fatigue cycles with a mean stress of 600MPa on Sample 6

This is further illustrated in Figure 76 which shows the data over the last 0.25mm of the sample width. This is important information when interpreting the predicted stress levels from the finite element analysis, particularly in the transition zones from localised plastic deformation to lower stress elastic deformation.

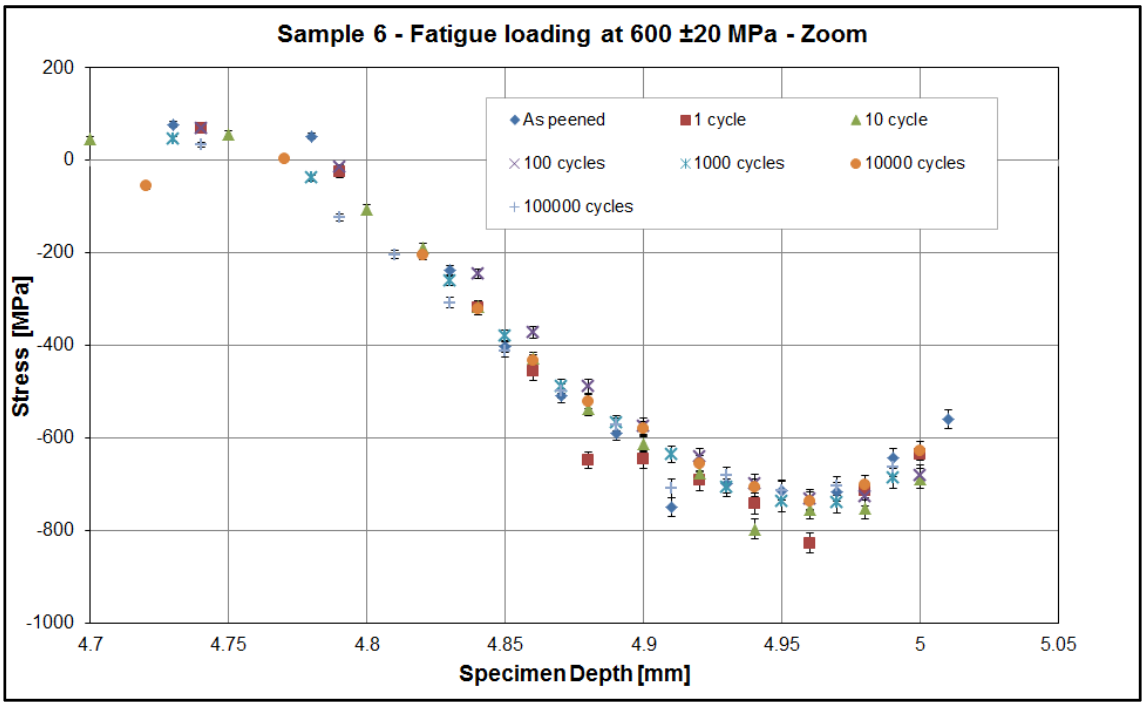

Figure 76: Detail of the last 0.25 mm of the residual stress profiles for the fatigue loading resulting in a mean stress of 600MPa (including error bars)

The next stage in the fatigue testing was the application of loading to achieve a maximum stress of 868MPa. The residual stress data after the first cycle of loading is shown in Figure 77, together with the equivalent data obtained after the further application of 100 and 10,000 cycles. Limitations in experimental time prevented measurements being made after further load cycling. The results shown in Figure 77 have been calculated from the longitudinal strain tensor, but a measurement at 45° to the longitudinal axis after the 10,000 cycle condition showed that some relaxation had taken place and as a result the strain error increased by a factor of 2. This is taken into account in the error bar calculation for the data shown in Figure 77.

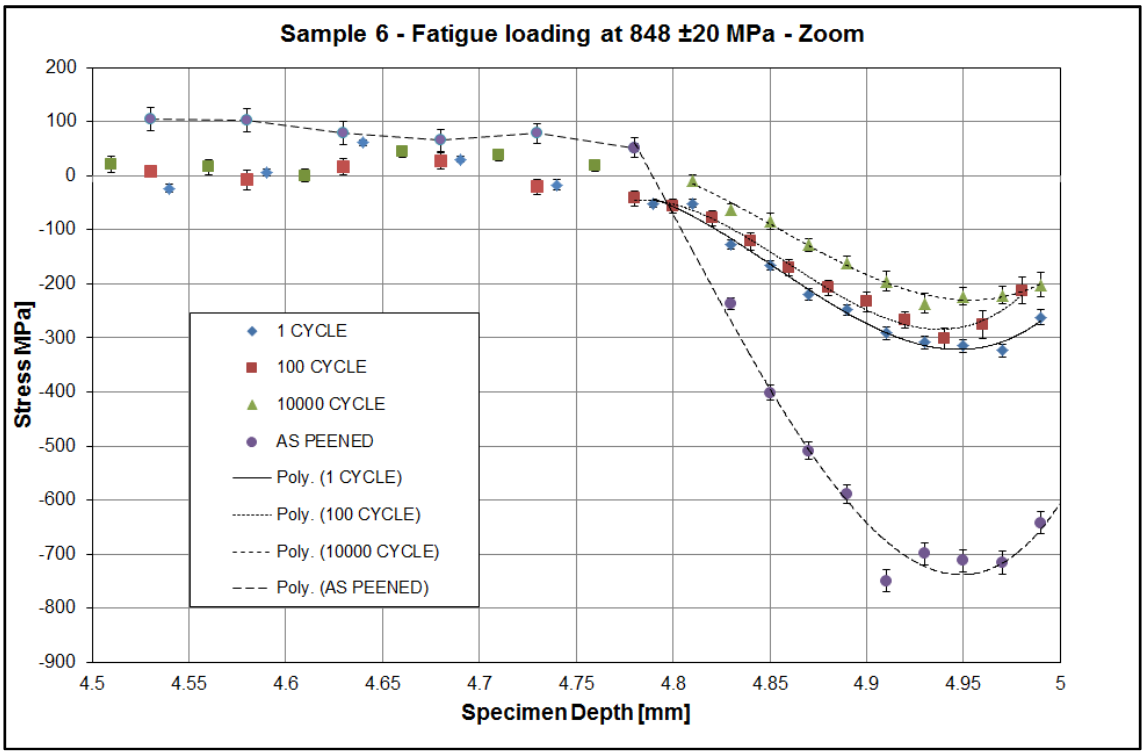

Figure 77: Residual stress profiles after fatigue tests at a mean stress of 848MPa with a maximum of 868MPa

Figure 77 shows the calculated residual stress data obtained over the last 0.5mm of the sample with a third order polynomial fit applied over the last 0.25mm. The reduction in residual stress as a result of the fatigue cycling is clearly evident. The maximum compressive stresses have reduced, but so have the maximum tensile stresses in order to balance out this change. This implies that there will be less of a metallurgical notch in the transition from compression to tension, at approximately 0.25mm below the surface.

The polynomial formulae from the curve fitting were used to calculate the values of the maximum residual stresses, for each curve, at a depth of 50µm below the surface and these values have been plotted in Figure 78. The data, which excludes the first cycle to 868MPa, shows a log-linear trend up to 10,000 cycles and an extrapolation has been done to 100,000 cycles as an illustration of the reduction in residual stress if this trend continued. Kodama [**46**] found a similar

relationship in fatigue tests on mild steel where the surface residual stress was found to follow a log-linear trend after the first load cycle, when plotted against the number of fatigue cycles as shown in the formula below;

$$\boldsymbol{\sigma_N^{re} = A + mlogN}$$

Equation 12 – from Kodama [46]

Where;

σ_N^{re} *is the surface residual stress after* N *cycles*

A *and* m *are material constants depending on the stress amplitude*

From Figure 78, Equation 12 may be written as;

$$\sigma_N^{re} = -323.56 + 23.3275logN$$

Equation 13 – Residual stress after N cycles

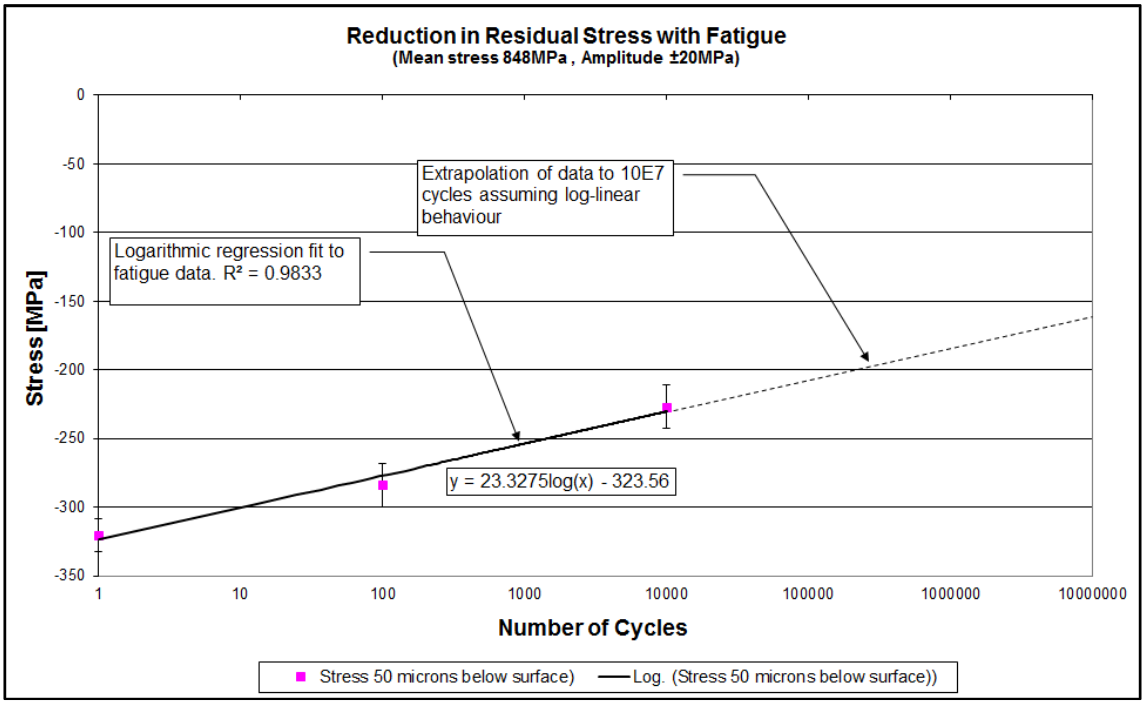

Figure 78: Illustration of the reduction in residual stress after fatigue loading at 0.2% proof stress with a stress amplitude of ±20MPa

5.5 PROTO laboratory XRD results

A set of residual stress data using the layer removal method was recorded from Sample 7 (150% coverage) using the Proto iXRD system in September 2011. A Cr-Kα X-ray source with a wavelength of 2.291Å was used with an aperture of 1mm, reflections off the {211} plane were measured. Eleven peaks were measured over a goniometer range of ±30° and the data processed using the $sin^2\psi$ technique. The longitudinal strain was measured in steps of approximately 15µm. The layer removal was done using the Proto electro-polishing system with an electrolyte comprising 15% H_2SO_4 in ethanol. The diameter of the polished area was approximately 9mm, as shown in Figure 79.

The Proto electro-polishing device is designed to be applied to a very specific small area, which minimises the amount of material removed. This reduces the effect of ghost stresses (explained in 2.3.2) significantly as the reduction in the second moment area of the sample is minimised.

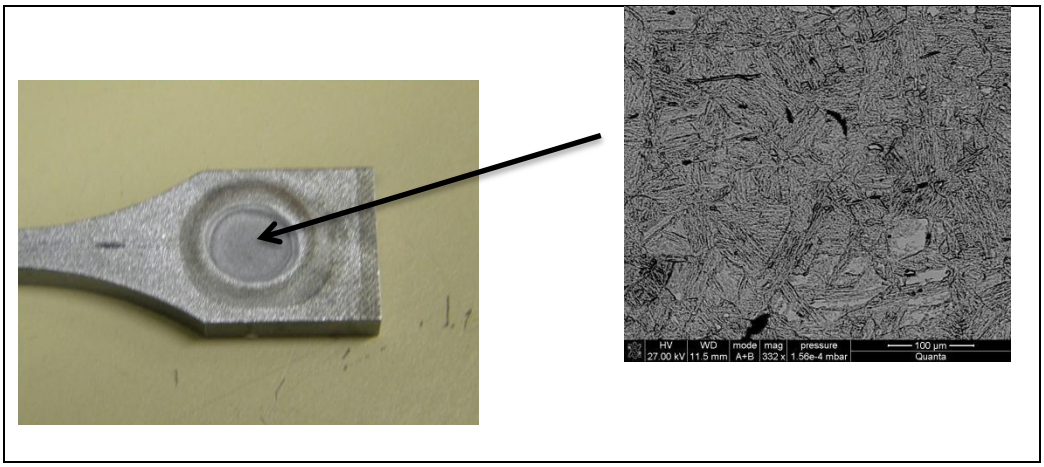

Figure 79: Electro-polishing on Sample 7

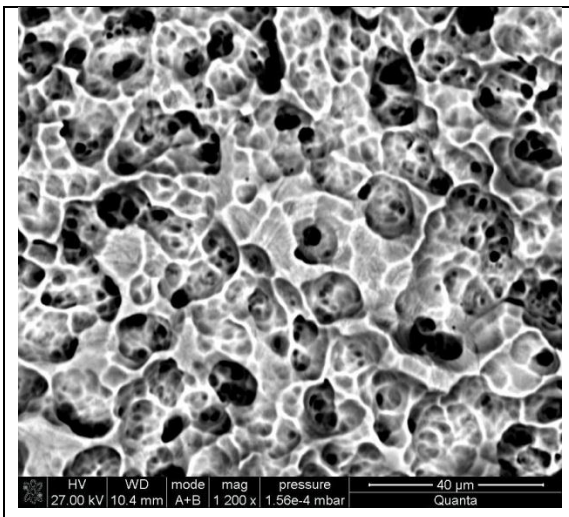

(a) Bad Polishing – Perchloric acid in ethanol and water

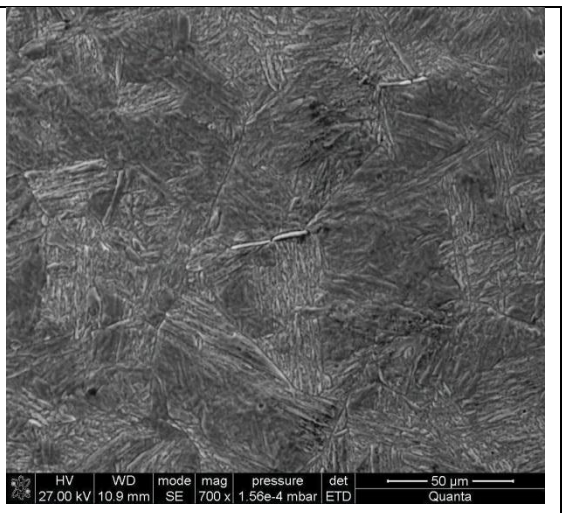

(b) Good Polishing – Sulphuric acid in ethanol

Figure 80: Examples of bad and good electro-polishing

Figure 80 shows the electro-polished surface of one of the flat samples with two different solutions. Figure 80a illustrates the effect of an incorrect process, using a solution made up of 50ml of perchloric acid, 140ml of water and 750ml of ethanol, with a voltage setting of 18 volts. This process removed material, but also attacked the grain boundaries resulting in a stress relieved surface layer, which would result in very large measurement errors.

The 12Cr turbine blade steel was very difficult to work with, but Figure 80b demonstrates the surface achieved with a successful polishing technique using the 15% H_2SO_4 in ethanol solution, obtained with Sample 7 shown in Figure 79. Electro-polishing with this electrolyte still resulted in some inconsistency of surface finish, even though the process was applied very carefully. The centre of the polished area had a slightly matt finish and the outer ring of the polished area had the desired bright finish.

The plots for the centre and edge of the polished area are shown in Figure 81. The XRD data from the edge of the polished area correlated very well with the synchrotron data. The XRD data from the centre had a flat profile in the highly stressed near-surface region of compressive stresses and also in the transition region from compressive to tensile stresses. This was due to some surface residual stress relieving still taking place during electro-polishing, as evidenced by the matt finish and highlights the amount of care required when doing layer removal experiments. The data was also corrected for the effects of ghost stresses [**31**], [**37**]. The data shown in Figure 81 illustrates the correlation obtained between the synchrotron data and the layer removal data. This is very valuable information for future work, as it indicates that significant work can be undertaken locally without having to try and get access to the synchrotron radiaiton facility in Grenoble.

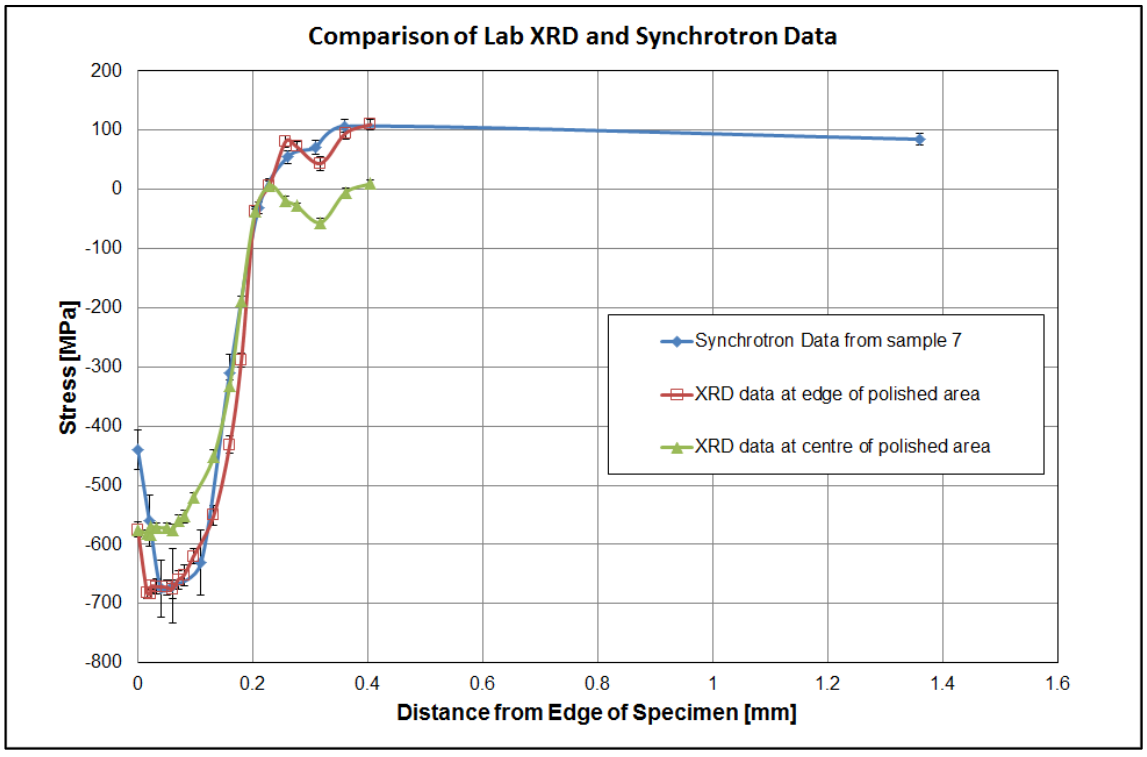

Figure 81: Comparison of synchrotron and layer removal data for Sample 7

The Proto iXRD instrument was also used to analyse the variation of the surface residual stress around the top serration of fir tree sample 3. Figure 82 shows the tabulated values on a schematic of the of the top serration, next to a photograph of the actual marked out positions.

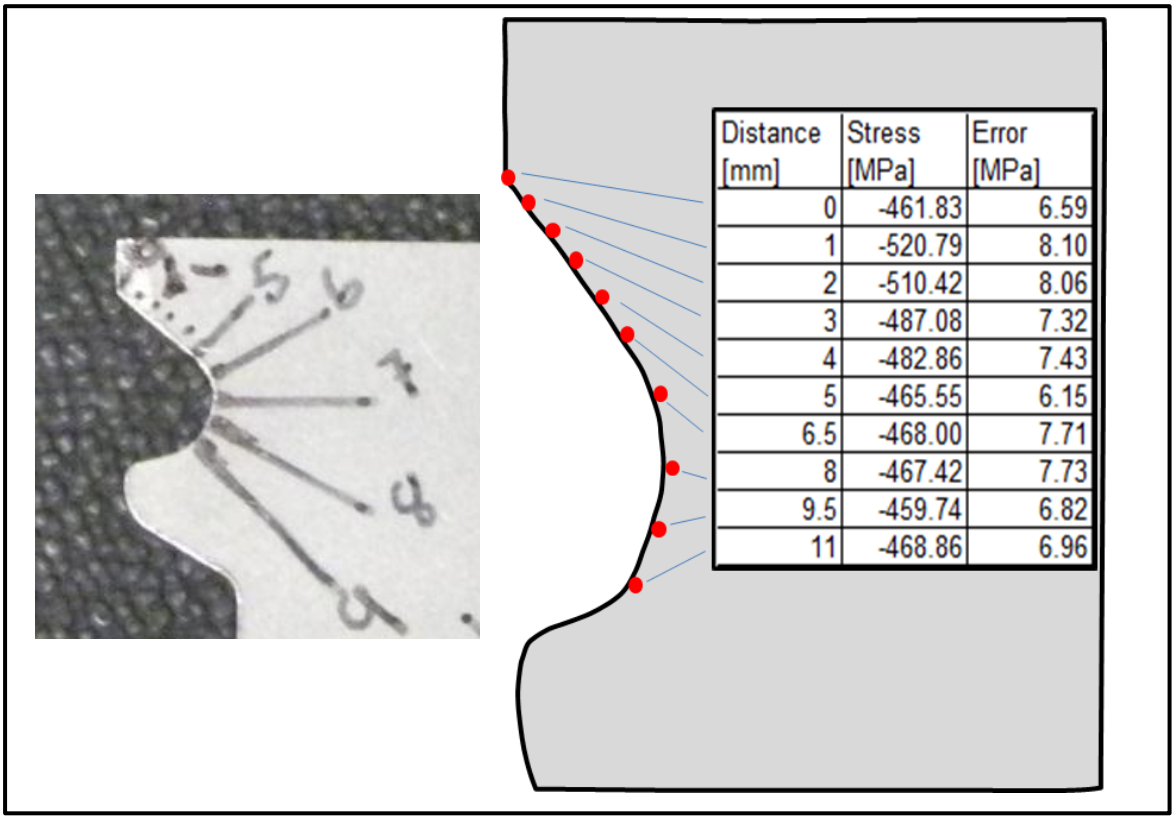

Distance [mm]	Stress [MPa]	Error [MPa]
0	-461.83	6.59
1	-520.79	8.10
2	-510.42	8.06
3	-487.08	7.32
4	-482.86	7.43
5	-465.55	6.15
6.5	-468.00	7.71
8	-467.42	7.73
9.5	-459.74	6.82
11	-468.86	6.96

Figure 82: Schematic of transverse surface stress around fir tree first serration, tabulated per measurement position

The data shown in Figure 82 was recorded on the shot peened surface, in the transverse direction (across the 5mm thickness of the sample), at ten points around the surface of the first serration using the Proto iXRD system. The data shows that the stress at the bottom of the serration (line 7), which is the main area of interest, is fairly uniform, with a compressive magnitude of approximately -465MPa. This was within the range recorded on the flat samples as shown previously in Figure 70.

5.6 Finite element modelling results

Results from the finite element modelling are shown in Figure 83 to Figure 88. Figure 83 shows the results of a centrifugal load at 3300rpm, with no shot peening having been applied. The maximum stress in the top serration is 891MPa which is above the 0.2% yield value of 868MPa.

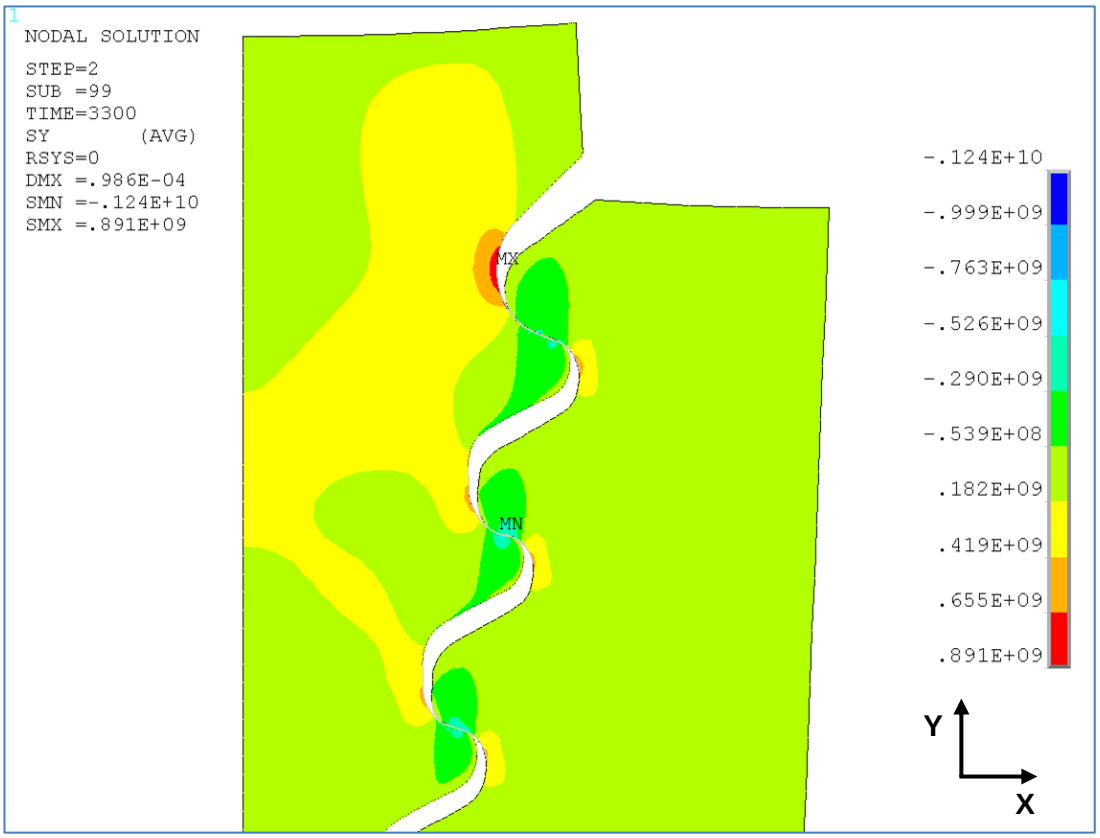

Figure 83: Finite element analysis of fir tree root for centrifugal loading at 3300rpm, resulting in localised stress in the top serration of 891MPa.

Figure 84 shows the residual stress profile generated by the quench loading on the flat sample model. As stated previously the parameters used for applying the quench loading were arrived at through an iterative process and are listed in Table 8.

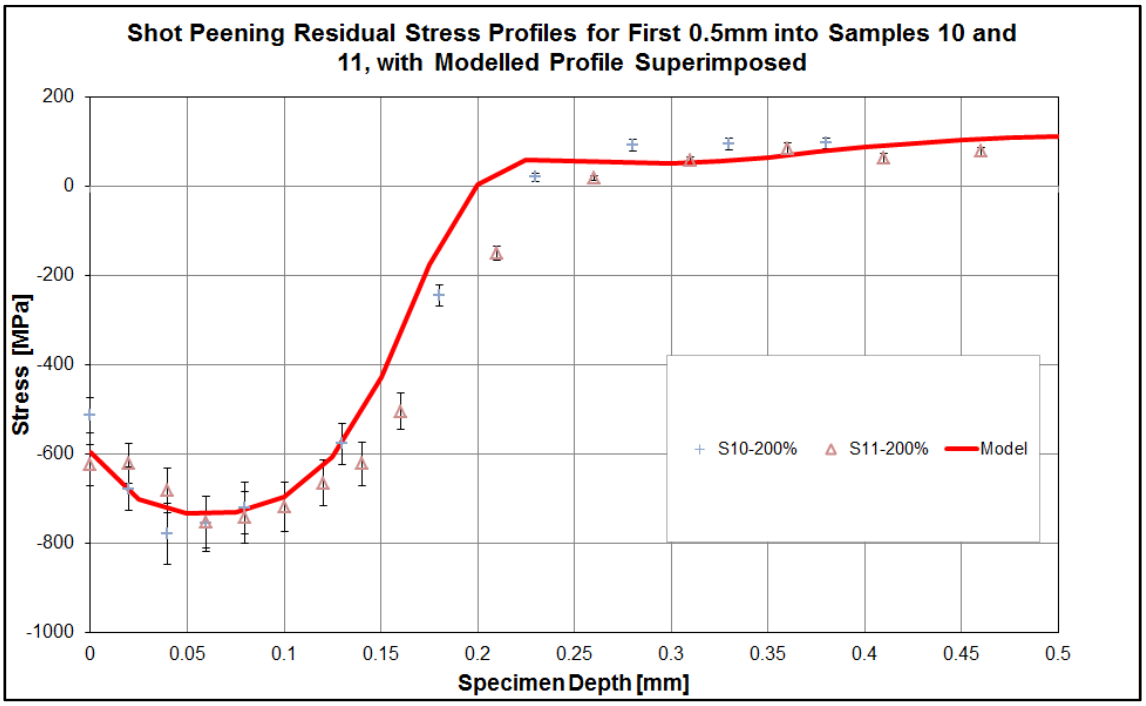

Figure 84: Comparison between the finite element and synchrotron residual stress data for the as-peened flat samples at 200% coverage

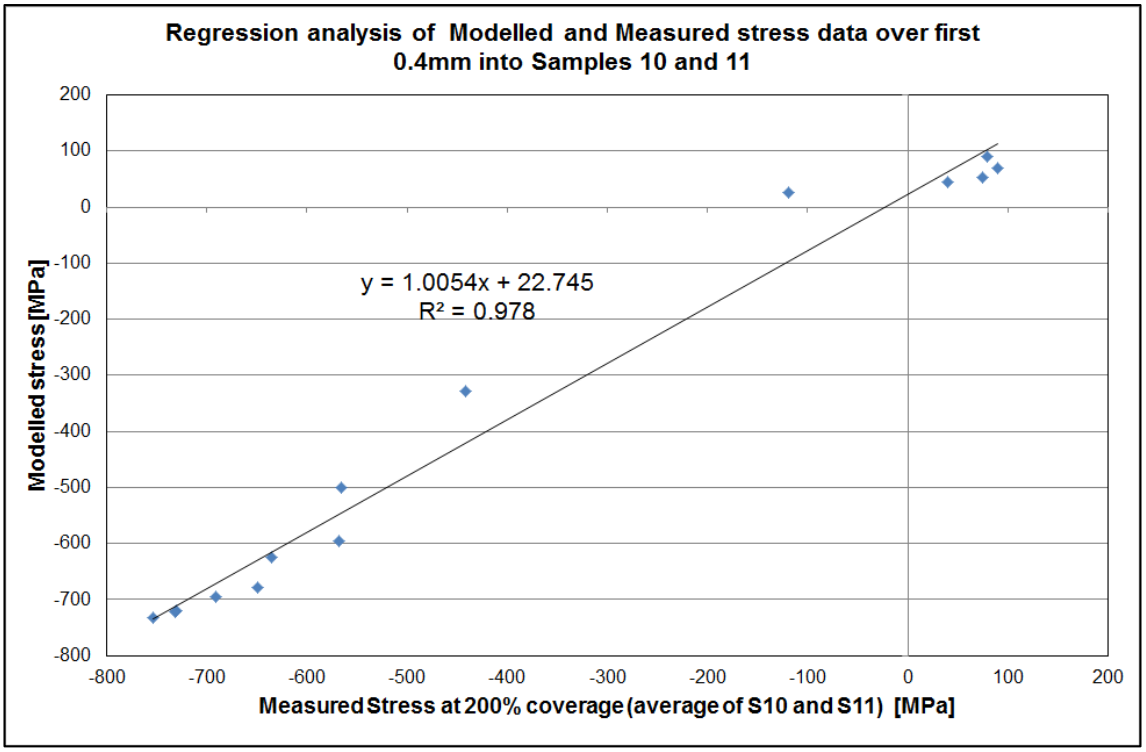

Figure 85: Regression analysis of the averaged measured data for Samples 10 and 11 vs the modelled stress data

The correlation with the measured synchrotron data for the samples with 200% coverage is very good as shown in Figure 84. A regression analysis of the averaged measured data for Samples 10 and 11 and the modelled stress data yielded the result shown in Figure 85, where the $R^2 = 0.978$.

The same process was then applied to the finite element fir tree model. Overspeed loading was applied at 3300rpm and then 3600rpm as shown in Table 15.

LOAD STEP	SHOTPEENED	LOAD STEP	NO SHOTPEEN
1	quench	1	3300rpm
2	normalise	2	0rpm
3	3000rpm	3	3000rpm
4	0rpm	4	3600rpm
5	3300rpm	5	0rpm
6	0rpm	6	3000rpm
7	3600rpm		
8	0rpm		
9	3000rpm		

Table 15: Summary of finite element modelling load cases

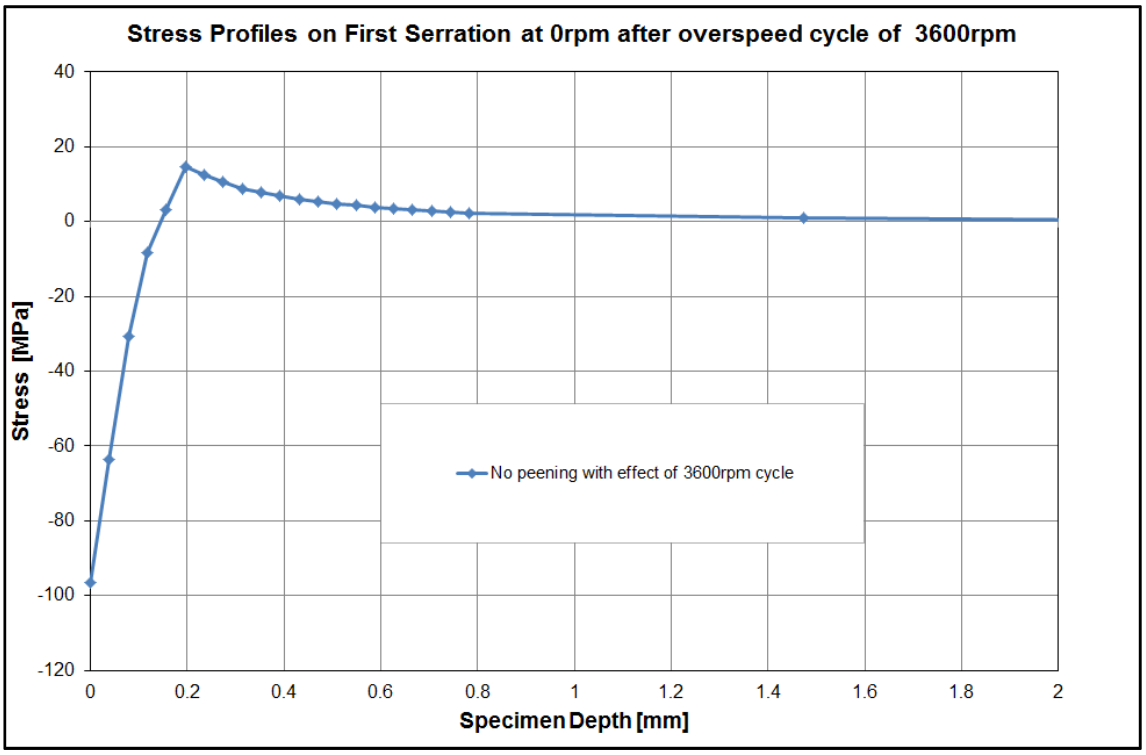

Figure 86: Finite element residual stress profile on un-peened root after overspeed cycle of 3600rpm

Figure 86 shows that when a load cycle of centrifugal loading at 3600rpm was applied to the fir tree finite element model for a blade with no shot peening localised yielding in the top serration took place. This resulted in a compressive residual stress once the centrifugal loading was removed due to the constraint of the elastic material below the plastic region. This effect, generally termed *proof testing*, has previously been applied to turbine rotors that were not shot peened as a means of improving fatigue life. The compressive stress amplitude induced by the overspeed was small compared to the shot peened residual stress.

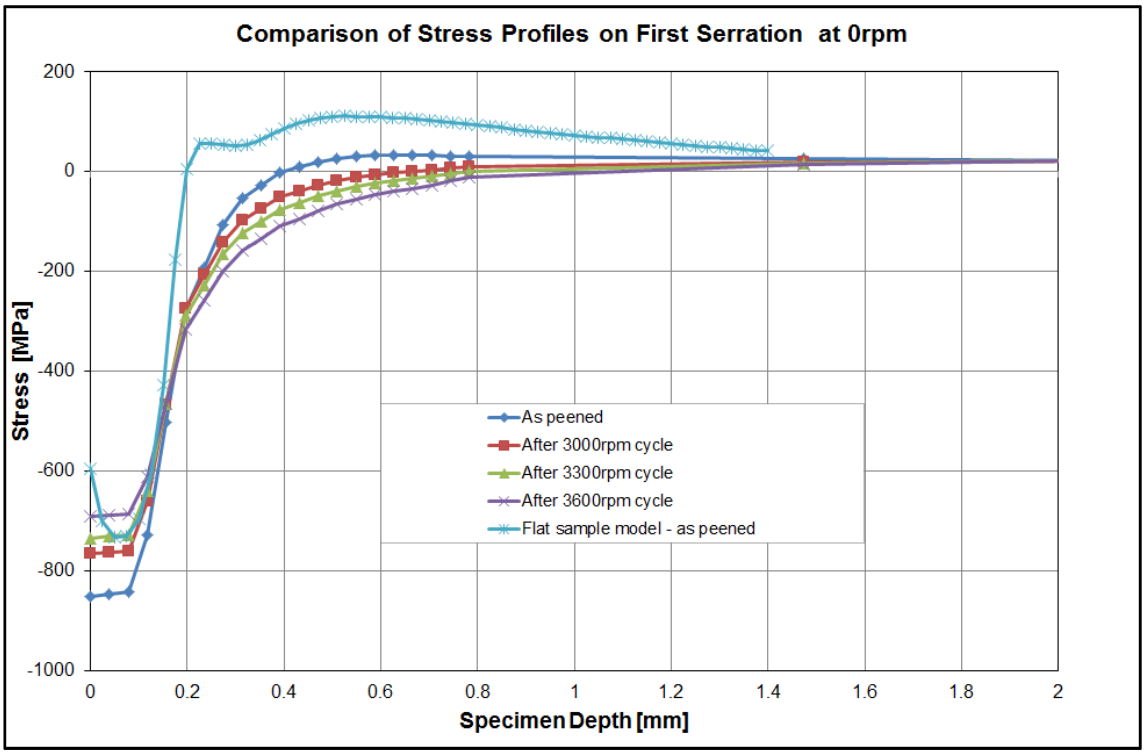

Figure 87: Comparison of residual stress profiles on the fir tree first serration at rest (0rpm), after centrifugal load cycles have been applied. The flat sample as-peened condition is shown for comparison.

Figure 87 shows a number of curves calculated by the finite element analysis of the residual stress profile for a shot peened blade at rest (0rpm) after centrifugal loading has been applied equivalent to various blade speeds. The profile for the flat sample is included to show the difference arising from the fir tree profile mainly due to increased constraint and depth of sample.

The effect of applying increasing centrifugal loads at 3000, 3300 and 3600rpm is evident. The first cycle of 3000rpm reduces the surface compressive residual stress from -850MPa to -766MPa, after 3300rpm it reduces to -734MPa and after 3600rpm it reduces to -690MPa. This reduction in the compressive peak is controlled by the constraint of the fir tree configuration, so that even though

the applied centrifugal stress at 3300rpm and 3600rpm was above yield on the surface, the reduction of residual stress on the surface was small.

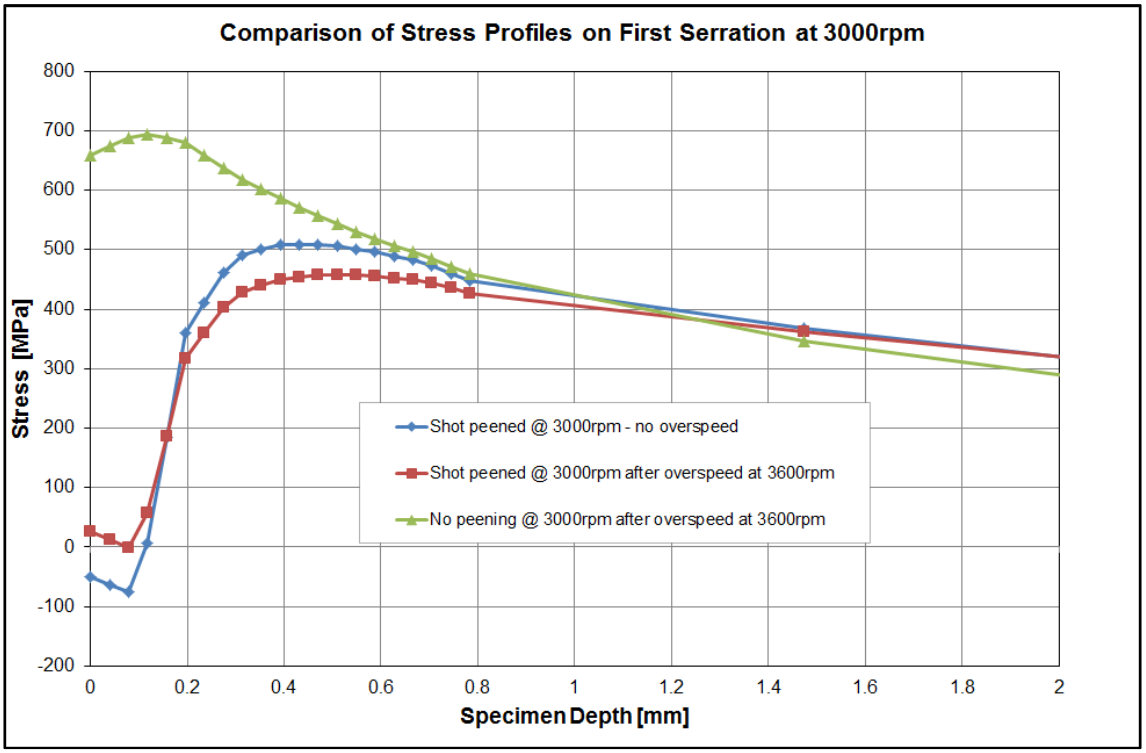

Figure 88: Comparison of stress profiles on the fir tree first serration at 3000rpm

Figure 88 shows residual stress curves at the centrifugal load equivalent to a speed of 3000rpm (the usual running speed of a turbine) for three conditions of blade;

- the shot peened condition at 3000rpm with no overspeed cycle
- the shot peened condition at 3000rpm after an overspeed cycle at 3600rpm
- the un-peened condition after an overspeed cycle at 3600rpm

It is clear that there is a significant advantage in residual stress terms to having the shot peening treatment on the fir tree root, as the resulting surface stress

after the overspeed cycle is predicted to be 25MPa as opposed to 675MPa for the un-peened condition

The results of the finite element modelling correlates well with work by Soady et al [**24**] showing that a notched specimen does not lose all of its compressive stress when localised yielding takes place and that shot peening is beneficial in low cycle fatigue applications. The results that they obtained showed that for a notched sample loaded in a three point bending rig the applied load resulted in a small change in residual stress after 1 cycle and then remained virtually unchanged at 50% of fatigue life, see Figure 30 page 36.

CHAPTER 6 SUMMARY OF FINDINGS

The synchrotron XRD results are clearly capable of generating profiles of the residual stresses throughout the entire 5mm cross section of the specimens with high spatial resolution, and also allow the effects of in-situ fatigue cycling to be followed.

The data show the typical residual stress profiles expected from shot-peening with a maximum compressive stress occurring just below the surface, gradually increasing towards tension at a distance of a few hundred microns below the surface. The synchrotron data will serve as an important reference for further work in this area, particularly in validating both finite element modelling and other residual stress measurement techniques. As this data was obtained using through-thickness measurements which allows stress balancing to be done on the data it is possible to eliminate any d_0 measurement errors and this lends the data a high degree of industrial credibility.

The variation in the compressive residual stress profile for specimens subjected to coverage values between 75% and 200% is minimal, and this supports the conclusions reached by Prevéy and Cammett, [**20**], [**21**] that coverage below 100% was still very effective against fatigue on aircraft quality 4340 (NiCrMo steel plate) and IN718 (Ni based super alloy). This implies that the residual stress profile resulting from 100% shot peening coverage is sufficient for the turbine blade fir tree root even though the Eskom standard currently requires 200%. A coverage condition of 100% would also result in reduced surface

roughness of the shot peened area, which would aid in the assembly of the blades as well as potentially reducing susceptibility to SCC and fatigue.

There was no discernible effect on the as-peened residual stresses from the fatigue loading of the flat samples, with an amplitude of 20MPa when the mean stress was set at 600MPa (69% of the 0.2% proof stress). However, cycling with a mean stress of 848MPa and an amplitude of 20MPa (giving a peak stress in the fatigue cycle equal to the 0.2% proof stress of 868MPa), produced a definite effect on the residual stress, with the compressive peak stress value decreasing with a log-linear trend as a function of number of cycles. The application of 10,000 such cycles reduces the peak compressive stress by some 30%. Clearly, this would have a significant effect on expected performance during service cycling if the peak stress reaches the 0.2% yield stress or higher. The material constraint of the fir tree root configuration does however provide significant mitigation against reduction in residual stress as discussed in the next paragraph. The dynamic stress amplitude of ±20MPa is conservative and a value of 10MPa is more likely, however turbine blades accumulate fatigue cycles at a high rate. If a turbine rotor rotates at 50Hz and is affected by some sort of flow restriction then 4.32×10^6 cycles will be accumulated in a 24 hour period.

Finite element modelling using an elastic/perfectly plastic model with thermal quenching loading used to simulate the residual stresses obtained via shot peening has resulted in a good replication of the measured shot peened stress profile, see Figure 84. Application of the centrifugal loading is illustrated in

Figure 87 and Figure 88. A finite element model was also constructed and analysed for the case of a fir tree serration with no shot peening.

The benefit of the shot peening process to the fir tree serration stresses can clearly be seen in Figure 88, where the centrifugal loading at 3000rpm is applied after the application of overspeed cycles. The shot peened condition has a predicted surface stress of 25MPa as opposed to 675MPa for the un-peened condition and is hence much better able to resist the initiation of fatigue or stress corrosion cracks.

The results of the finite element modelling correlate well with work by Soady et al [**24**] showing that a notched specimen does not lose all of its compressive stress when localised yielding takes place and that shot peening is beneficial in low cycle fatigue applications. This would be true even in the extreme case of centrifugal loading on a fir tree root due to a 3600rpm overspeed condition (normally 3300rpm would be the maximum). The fir tree root is thus not expected to have the same fatigue characteristics as the flat samples.

CHAPTER 7 CONCLUSIONS AND SUGGESTIONS FOR FURTHER WORK

The shot peening treatment of fir tree turbine blade roots has been demonstrated to result in significantly beneficial residual stresses, even after the application of overspeed centrifugal loading which is required at certain times during the life of a steam turbine blade.

The variation in residual stress values observed for shot peening coverage values between 75% and 200% is minimal, which implies that 100% coverage is sufficient to achieve the desired result. The Eskom standard currently requires 200% which results in higher roughness which, in itself, is detrimental to blade fit-up and possibly to fatigue life.

Fatigue load cycles applied to the flat samples showed that the residual stress reduces significantly if the 0.2% stress limit is reached during dynamic loading. The constraint of the fir tree root will however limit this effect.

The synchrotron data will serve as an important reference point for further work in this area, particularly in validating other modelling techniques.

REFERENCES

[1] W Nel, "Duvha Power Station – blade analysis," Eskom Technical Report MT320/2005, 2004.

[2] Wegst GmbH, *Key to Steel 1998*. Marbach, Germany, 2004.

[3] JP Botha, "Shot peening process for stage 5 turbine blades," *SAA Technical procedure for Eskom*, 2005.

[4] MN James, DJ Hughes, Z Chen, H Lombard, DG Hattingh, D Asquith, JR Yates, and PJ Webster, "Residual stresses and fatigue performance," *Engineering Failure Analysis*, no. ISSN 1350-6307, 2006.

[5] M N James, D G Hattingh, D J Hughes, L-W Wei, E A Patterson, and J Fonseca, "Synchrotron diffraction investigation of the distribution and influence of residual stresses in fatigue," *Fatigue and Fracture of Engineering Materials and Structures*, vol. 27, no. ISSN 0160-4112, pp. 609-622, 2004.

[6] M Johannes, "Turbine Blade Root Inspections – an Assessment and Feasability Study of UT Capabilities," Eskom Research Report RES/RR/03/22773, 2004.

[7] H Pollak, E Pfitzinger, N Thamm, and M Schwarz, "Design And Materials For Modern Steam Turbines With Two Cylinder Design Up To 700 MW," Siemens AG, Power Generation, Germany,.

[8] TH McCloskey, RB Dooley, and WP McNaughton, *Turbine Steam Path Damage: Theory and Practice Volume 1*, 0803350627th ed.: EPRI, 1999.

[9] TH McCloskey, RB Dooley, and WP McNaughton, *Turbine Steam Path Damage: Theory and Practice Volume 2*, 0803350635th ed.: EPRI, 1999.

[10] NF Rieger, TH McClosky, and Dewey RP, "The High Cost of Failure of Rotating Equipment," *MFPG 44, Vibration Institute*, 1990.

[11] GW Prabhugaunkar, MS Rawat, and CR Prasad, "Role of Shot Peening on Life Extension of 12% Cr Turbine Blading Martensitic Steel Subjected to SCC and Corrosion Fatigue," in *The 7th International Conference on Shot Peening*, Warsaw Poland, 1999.

[12] SA Meguid, G Shagal, and JC Stranart, "3D FE analysis of peening of strain-rate sensitive materials using multiple impingement model," *International Journal of Impact Engineering*, vol. 27, pp. 119–134, 2002.

[13] J Altenkirch, "Stress engineering of Friction Stir Welding: Measurement and Control of," Manchester University, PhD Thesis 2009.

[14] M Guagliano, "Relating Almen intensity to residual stresses induced by shot peening: a numerical approach," *Journal of Materials Processing Technology*, no. 110, pp. 277-286, 2001.

[15] YF Al-Obaid, "Shot peening mechanics: experimental and theoretical analysis," *Mechanics of Materials 19*, pp. 251-260, 1995.

[16] PE Cary, "History of Shot Peening," in *The 1st International Conference on Shot Peening*, pp. 23-28.

[17] G Nachman, "Shot Peening - past Present and Future," in *ICSP7*, Warsaw, 1999.

[18] SAE Aerospace Material Specification, "Shot Peening of Metal Parts," SAE, AMS-S-13165, Nov 1997.

[19] S Kyriacou, "Shot-Peening Mechanics a Theoretical Study," in *ICSP6*, San Francisco, 1996, pp. 505-516.

[20] PS Prevéy and JT Cammett, "The Effect of Shot Peening Coverage on Residual Stress, Cold Work and Fatigue in a Ni-Cr-Mo Low Alloy Steel," in *International Conference on Shot Peening*, Garmisch-Partenkirchen, 2002.

[21] JT Cammett, PS Prevéy, and N Jayaraman, "The effect of shot peening coverage on residual stress, cold work, and fatigue in a nickel-base superalloy," in *ICSP 9*, Paris, 2005, p. Paper 261.

[22] SA Meguid, "Effect of Partial-Coverage Upon the Fatigue Fracture Behaviour of Peened Components," *Fatigue & Fracture of Engineering Materials and Structures*, vol. 14, pp. 515-530, May 1991.

[23] D Kirk and RC Hollyoak, "Realtionship between Coverage and Surface Residual Stress," in *The 9th International Conference on Shot Peening*, Paris, France, 2005, pp. 373-378.

[24] KA Soady, BG Mellor, J Shackleton, A Morris, and PAS Reed, "The effect of shot peening on notched low cycle fatigue," *Materials Science and Engineering A*, no. 528, pp. 8579-8588, 2011.

[25] PJ Withers, "Residual Stress definition," in *Encyclopaedia of Materials: Science and Technology*.: ISBN: 0-08-0431526, 2001, pp. 8110-8113.

[26] FA Kandil, JD Lord, AT Fry, and PV Grant, "A Review of Residual Stress Measurement Methods - A Guide to Technique Selection," National Physical Laboratory, UK, Middelsex, NPL Report MATC(A)04 ISSN 1361-4061, 2001.

[27] PJ Withers and HKDH Bhadeshia, "Residual stress Part 1 – Measurement techniques," *Materials Science and Technology*, vol. 17, no. ISSN 0267 – 0836, April 2001.

[28] MN James, "Residual stress influences on structural reliability," *Engineering Failure Analysis*, vol. 18, pp. 1909-1920, 2011.

[29] PJ Withers, "Residual Stresses: Measurement by Diffraction," in *Encyclopaedia of Materials: Science and Technology*.: ISBN: 0-08-0431526, 2001, pp. 8158-8170.

[30] DJ Hughes, MN James, DJ Hattingh, and PJ Webster, "The Use of Combs for Evaluation of Strain-free References for Residual Strain Measurements by Neutron and Synchrotron X-ray Diffraction," *Journal of Neutron Research, December 2003 Vol. 11 (4), pp. 289–293*, vol. 11, pp. 289-293, December 2003.

[31] V Hauk and B Krüger, "Invariant intersections in diffraction stress analysis — a check of experimental results," vol. A284, pp. 261-267, 2000.

[32] PANalytical, *XRD Course Residual Stress*. The Netherlands: PANalytical B.V., May 2006.

[33] ME Fitzpatrick, AT Fry, P Holdway, FA Kandil, J Shackleton, and L Suominen, "Determination of Residual Stresses by X-ray Diffraction – Issue 2," National Physics Laboratory, UK, Measurement Good Practice Guide No. 52 ISSN 1744-3911, 2005.

[34] GF van der Voort, *Metallography, principles and practice*.: McGraw – Hill, 2004.

[35] ABLE Electropolishing Inc., *Looking for solutions to metal surface problems?*: ABLE Electropolishing Inc., 2007.

[36] V Palmieri, "Fundamentals of electrochemistry - the electrolytic polishing of metals: application to Copper and Niobium," Istituto Nazionale Di Fisica Nucleare Laboratori Nazionali di Legnaro,.

[37] T Christiansen and MAJ Somers, "Avoiding ghost stress on reconstruction of stress- and composition-depth profiles from destructive X-ray diffraction depth profiling," *Materials Science and Engineering*, vol. A 424, pp. 181-189, 2006.

[38] T Hong, JY Ooi, and B Shaw, "A numerical simulation to relate the shot peening parameters to the induced residual stresses," *Engineering Failure Analysis*, 2008.

[39] C Hardy, CN Baronet, and GV Tordion, "The elasto-plastic indentation of a half-space by a rigid sphere," *Int J Numer Methods Eng*, vol. 3, pp. 451-462, 1971.

[40] PA Cundall and ODL Strack, "A Discrete Numerical Model for Granular Assemblies," Géotechnique," *Géotechnique*, vol. 29, pp. 47-65, 1979.

[41] RG Fata, JA Jones, AB Perlman, and O Orringer, "A numerical model for estimation of temperature-time history and residual stress in head-hardened rails," *ISS Technical Paper*, pp. 1-8, 1997.

[42] C Hakan Gür and A, Erman Tekkaya, "Numerical investigation of non-homogeneous plastic deformation in quenching process," *Materials Science and Engineering A319–321*, pp. 164-169, 2001.

[43] ESRF. (2011) European Synchrotron Radiation Facility, Beam lines ID31 and ID15A. [Online]. http://www.esrf.eu/about/organisation

[44] E J Hearn, *Mechanics of Materials Volume 1 and 2*.: Pergamon Press, 1994, ISBN 0080311318.

[45] Y-S Xiong and P J Withers, "A deconvolution method for the reconstruction of underlying profiles measured using large sampling volumes," *Journal of Applied Crystallography*, vol. 39, pp. 410-424, 2006.

[46] S Kodama, "The behaviour of residual stress during fatigue stress cycles," in *In: Proceedings of the International Conference on Mechanical Behavior of Metals II, Society of Material Science*, Kyoto, 1972, pp. 111-118.